國立交通大學

光電工程學系

博 士 論 文

入射光瞳編碼控制以及其應用

Pupil Engineering and Its Applications

研 究 生：藍子翔

指導教授：田仲豪　教授

中 華 民 國 一 百 年 九 月

入射光瞳編碼控制以及其應用

學生：藍子翔　　指導教授：田仲豪博士

國立交通大學光電工程學系博士班

摘要

本論文以研討入射光瞳之振幅、相位、與極化對高數值孔徑光學系統之三維聚焦函數的變化作為本博士論文的開端主軸，尤其著重在探討極化對於聚焦光場調變之控制與影響。經由對入射極化分佈與聚焦光場場型關係之了解，本論文提出一個具動態控制之光學架構，以實驗的方式合成出具任意極化分布的雷射光源。且搭配高數值孔徑之聚焦系統，吾人更進一步探討任意極化光與金薄膜及奈米金棒之交互作用，並利用所產生的表面電將共振機制提出四種創新的光學儀器概念，應用於表面電將激發、生醫感測器、與光儲存，包含了：遠場表面電將激發器、近場雷達偵測儀、全頻譜之表面電漿共振偵測儀、極化編碼之光儲存技術。

Pupil Engineering and Its Applications

Student：Tzu-Hsiang Lan　　Advisors：Dr. Chung-Hao Tien

Department of Photonics
National Chiao Tung University

ABSTRACT

The aim of this thesis is to study the response of a high numerical aperture lens by means of pupil engineering, especially in the polarization point of view, and to study the interaction between focused light and metal in associated with surface plasmon resonance. More specifically we aim to develop several different novel schemes and concepts for different surface plasmon mediated applications in terms of polarization manipulation at the pupil plane. In this thesis, four kinds of novel applications are proposed, including far-field surface plasmon polaritons excitation and manipulation, nanoscopy surface plasmon resonance radar, white light surface plasmon resonance sensor, and gold nanorods mediated polarization multiplexing recording.

致謝

我的人生一步一步地往上走到現在，但我的心就像稻穗一般，垂地一次比一次低，因為我藍子翔何德何能可以擁有如此精采燦爛的學生時代。我最想感謝的就是我的爸媽對我的栽培以及他們對我的教育，另外還有不同求學階段，每位老師給我的叮嚀與觀念，這些無形的思想觀念與態度徹底的改變了我，讓我今天才能順利邁向取得交通大學博士學位的路上。

我從小生長在新竹，交通大學對我來說不陌生，小時候每次上高速公路時都會經過，但對當時的我來說，要去那邊念書談何容易阿！很明顯地，那是一個遙不可及的夢想，就如同白日夢一般。不過幸運的是，我聽老師的話，並照著老師的叮嚀去做實踐、改變我的態度、並創造我想擁有的人生。尤其是北科大一年級時，科技管理的陳繩籌老師，告訴我們：若要如何全憑你自己、先知先著手先攻佔、差異化…等等的觀念。由於這些觀念跟態度的養成，讓在大學時代的我徹底的改變，做了很多令自己及父母驕傲的事情，甚至最後有機會推甄上交大光電碩士班。這段期間，我就像是那從蛹中蛻變出來的蝴蝶，有自信的在藍天中自由的飛翔。

六年前，開始在田仲豪老師的門下學習做研究，這是人生的另外一個開始。因為若不是五年前，田老師問我要不要直升博士班，以及當時我爸的支持態度「就試試看，大不了就大學畢業而已，只要我們有盡力去做，那剩下的就看老天要不要給我們這個機會了。」我打從出生就不曾想過要唸博士，所以更無法想像今天的我有幸能夠走到這裡。而也是因為這兩件事情的發生，讓我願意給自己一個挑戰，看看究竟我自己到底能走多遠。

在唸博士的這段期間，非常感謝田仲豪老師給了我很大的彈性與空間去花五年的時間去探索學術、工程、與人生，因為沒有他的包容與督促，我真的很難在五年後的今天能具備提畢業口試的資格，也感謝這五年來跟我一同做研究討論的學弟們－Paul、潘紀豪、張永昇、何展燁、鍾岳、李功賀、鍾議寬、與李杰恩。沒有你們的討論與一起努力，我的博士生活應該會更為漫長。而實驗室其他的學長與學弟們，因為一路上有你們的陪伴，讓我覺得我並不孤單。最後，也感謝國科會的支持，讓我可以在最後一年到澳大利亞墨爾本於 Swinburne University 的 CMP 中心，在顧敏老師與李向平計畫主持人的指導，做了快一年的研究，而其成果讓我博士研究主題的應用又更上一層樓。

該感謝的人太多了，最後就讓我感謝天跟地。

學生 藍子翔

目錄

圖目錄

Chapter I

Characterization of the Three-dimentional Point-spread Function by Pupil Mask

In an optical system, lens is always the most important optical element. It gives us the possibility to reproduce the image of an object for imaging purpose or to converge light into a hot spot for further applications. Generally, the lens can be treated as a linear response system, where the output (field distribution in the vicinity of focus) is depended on the input (field distribution at entrance pupil plane) and the impulse response of this lens (transfer function).

To understand this relation, there are two ways for analyzing the performance of a lens: the point spread function method and the transfer function method. The former, relatively simple in terms of the mathematical skills involved, is based on the image of a single point object and is easily understood, but it sometimes lacks an insight into an imaging process. The later analysis based on the concept of transfer function is given for an imaging system. It gives a physical insight into image formation in an optical imaging system. The function of an optical imaging system such as a microscope is to provide a magnified image of an object in which details are too fine to be seen by naked eye. It is desirable that an imaging system should have an ability to reproduce the detail in an object. However, as we known an optical imaging system is a low pass filter which transmits only low spatial frequencies corresponding to slow variations in an object. The fine details of the object are represented by high spatial frequencies. These high spatial frequencies may not be imaged because an optical system has a cutoff spatial frequency; this leaded to an imperfect image.

Here, we will restrict ourselves to the point spread function method to illustrate the link between input (field distribution at entrance pupil plane) and output (field distribution in the vicinity of focus) of a lens system because they are more suitable for us to understand the influence of field distribution at the focal plane caused by the change of pupil function. For simplicity, we will start from the diffraction pattern by a lens under the condition of the uniform illumination on the lens aperture and the paraxial approximation.

1.1 Diffraction by a Lens

In this section, we will consider the detail of the light field near the focal region of a lens. We firstly consider the light field in the focal region, i.e. at $z = f$, as shown in Fig. 1.1. Suppose that a plane wave of amplitude U_0 is incident upon a lens. Thus the field in the plane immediately before the lens is $U_1(x_1, x_2) = U_0$. The lens is a diffraction screen of a complex transmittance given by Eq. (1.1).

$$t(x,y) = P(x,y)exp\left[\frac{ik(x^2+y^2)}{2f}\right] \tag{1.1}$$

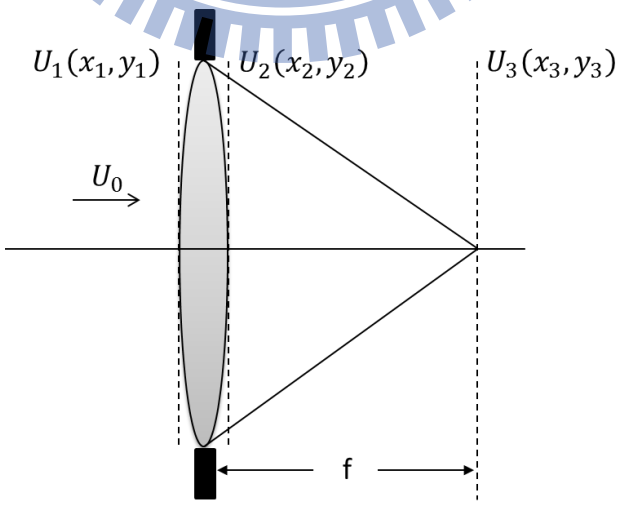

Fig. 1. 1 Diffraction by a lens in the focal plane.

Therefore, the field in the plane immediately behind the lens is

$$U_2(x_2, y_2) = U_0 P(x_2, y_2) exp\left[\frac{ik(x_2^2+y_2^2)}{2f}\right] \tag{1.2}$$

So the field in the focal can be derived from the Fresnel diffraction formula given by Eq. (1.3) shown as below

$$U_2(x_2, y_2) = \frac{iexp(-ikz)}{\lambda z}$$

$$\iint_{-\infty}^{\infty} U_1(x_1, y_1) exp\left\{-\frac{ik}{2z}[(x_2 - x_1)^2 + (y_2 - y_1)^2]\right\} dx_1 dy_1 \tag{1.3}$$

Substituting Eq. (1.2) into Eq. (1.3), we can express the light field in a plane of observation placed at the focus, i.e. at $z = f$, as

$$U_3(x_3, y_3) = \frac{iU_0}{\lambda f} exp(-ikf) \iint_{-\infty}^{\infty} P(x_2, y_2) exp\left[\frac{ik(x_2^2+y_2^2)}{2f}\right]$$

$$exp\left[-\frac{ik}{2f}(x_3^2 + y_3^2)\right] exp\left[-\frac{ik}{2f}(x_2^2 + y_2^2)\right] exp\left[\frac{ik}{f}(x_3 x + y_3 y)\right] dx_2 dy_2 \tag{1.4}$$

Here the nonlinear phase term in Eq. (1.3) has been expanded into three terms in the second line of Eq. (1.4). Clearly the quadratic phase caused by the lens is cancelled out by the quadratic phase resulting from the Fresnel diffraction process, which lead to

$$U_3(x_3, y_3) = \frac{iU_0}{\lambda f} exp(-ikf) exp\left[-\frac{ik}{2f}(x_3^2 + y_3^2)\right]$$

$$\iint_{-\infty}^{\infty} P(x_2, y_2) exp\left[\frac{ik}{f}(x_3 x + y_3 y)\right] dx_2 dy_2 \tag{1.5}$$

To explan the physical meaning of Eq. (1.5), we let $m = x_3/(f\lambda)$ and $n = y_3/(f\lambda)$. Thus the integration in Eq. (1.5) is the two-dimensional (2-D) Fourier transform of the pupil function $P(x, y)$ at spatial frequencies of m and n. Comparing Eq. (1.5) with Eq. (1.6) of Fraunhofer diffraction equation,

$$U_2(x_2, y_2) = \frac{iexp(-ikz)}{\lambda z} exp\left(-ik\frac{x_2^2+y_2^2}{2z}\right)$$

$$\iint_{-\infty}^{\infty} U_1(x_1, y_1) exp\left[\frac{ik}{z}(x_1 x_2 + y_1 y_2)\right] dx_1 dy_1 \tag{1.6}$$

we found that Eq. (1.5) gives a Fraunhofer diffraction by a circular aperture of radius a, one can use a lens of radius a and the resulting diffraction pattern in the focal plane as the

same distribution as the Fraunhofer diffraction by the circular aperture. It should be pointed out that although $U_3(x_3, y_3)$ in Eq. (1.5) takes a form of the Fraunhofer diffraction of the pupil function, the diffraction process caused by a lens is the Fresnel diffraction rather that the Fraunhofer diffraction.

Now let us turn into the study on the diffraction pattern by a thin lens if the observation plane is placed at a defocus position. Assume the defocus distance to be Δz, as shown in Fig. 1.2. The distance between the observation plane and the lens is thus $z = f + \Delta z$. For a uniform plane wave U_0 incident upon the lens, the field immediately behind the lens $U_2(x_2, y_2)$ is the same as Eq. (1.2). Therefore, in terms of the Fresnel diffraction formula Eq. (1.3), the field $U_3(x_3, y_3)$ on the observation plane at $z = f + \Delta z$ is given by

$$U_3(x_3, y_3) = \frac{iU_0}{\lambda z} exp(-ikz) \iint_{-\infty}^{\infty} P(x_2, y_2) exp\left[\frac{ik}{2f}(x_2^2 + y_2^2)\right]$$
$$exp\left\{-\frac{ik}{2z}[(x_3 - x_2)^2 + (y_3 - y_2)^2]\right\} dx_2 dy_2 \qquad (1.7)$$

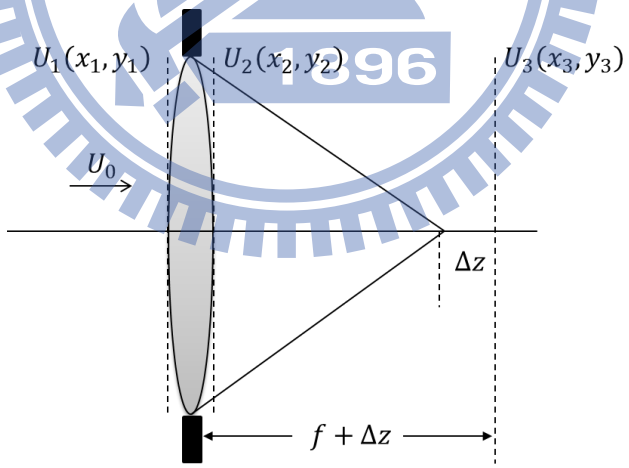

Fig. 1. 2 Diffraction by a lens in a defocus plane.

1.1.1 Circular Lens

As mentioned before, a practical lens is usually circularly symmetric. In this case, its

pupil function is only a function of the radial coordinate, i.e. $P(x,y) = P(r)$, where $r = (x^2 + y^2)^{1/2}$. Using a polar corrdinate system in Eq. (1.6), we have

$$U_3(r_3) = \frac{i}{\lambda f} exp(-ikf) \exp\left(-\frac{i\pi r_3^2}{\lambda f}\right) \int_0^\infty P(r_2) J_0\left(\frac{2\pi r r_3}{\lambda f}\right) 2\pi r_2 dr_2 \tag{1.8}$$

where we have assumed $U_0 = 1$. Here J_0 is a Bessel function of the first kind of order zero, $r_2 = (x_2^2 + y_2^2)^{1/2}$ and $r_3 = (x_3^2 + y_3^2)^{1/2}$.

If $P(r)$ is a uniform circular aperture with radius a, one can express its pupil function

$$P(r) = \begin{cases} 1, & r < 0, \\ 0, & otherwise. \end{cases} \tag{1.9}$$

By using the Hankel transform, we can reduce Eq. (1.8) to

$$U_3(r_3) = \frac{i\pi a^2}{\lambda f} exp(-ikf) \exp\left(-\frac{i\pi r_3^2}{\lambda f}\right) \left[\frac{2J_1\left(\frac{2\pi r_3 a}{\lambda f}\right)}{\left(\frac{2\pi r_3 a}{\lambda f}\right)}\right] \tag{1.10}$$

where J_1 is a Bessel function of the first kind of order unity.

In order to simplify Eq. (1.10), we introduce three important parameters.

(a) Numerical aperture of the lens, NA:

$$NA = n \sin\alpha \approx n \frac{a}{f} \tag{1.11}$$

The significance of the NA of an objective lens can be found from Fig. 1.3; a higher

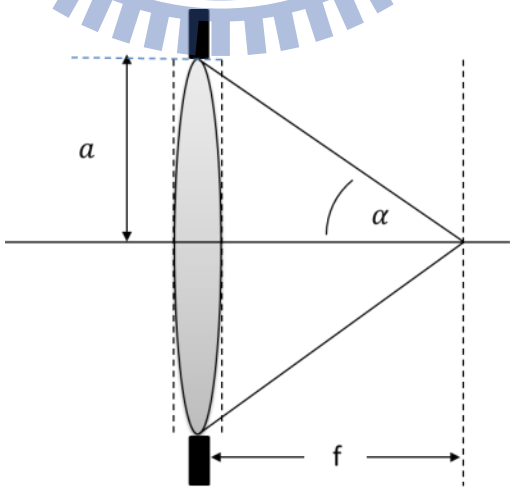

Fig. 1. 3 Description of the numerical aperture of a lens.

numerical-aperture objective corresponds to a larger maximum angle of convergence, α. For a given maximum angle of convergence, increasing the refractive index of immersion medium of a lens yields a high numerical aperture of an objective. Radial (transverse) optical coordinate ν. The definition of the radial optical coordinate is given by

$$\nu = \frac{2\pi}{\lambda}\frac{a}{f}r_3 \approx \frac{2\pi}{\lambda}r_3 \sin\alpha \tag{1.12}$$

Therefore for a given value of ν, the larger the numerical aperture of a lens the smaller the value of the real radial coordinate in the focal region.

(b) Fresnel number N:

$$N = \frac{\pi a^2}{\lambda f} \tag{1.13}$$

In terms of Eqs. (1.11) – (1.13), one can rewrite Eqs. (1.8) and (1.10) as

$$U_3(\nu) = 2iNexp(-ikf)\exp\left(-\frac{i\nu^2}{4N}\right)\int_0^1 P(\rho)\,J_0(\nu\rho)\rho d\rho \tag{1.14}$$

and

$$U_3(\nu) = iNexp(-ikf)\exp\left(-\frac{i\nu^2}{4N}\right)\left[\frac{2J_1(\nu)}{\nu}\right] \tag{1.15}$$

respectively, where $\rho = r_2/a$ is the normalized radial coordinate over lens aperture. $P(\rho)$ is the pupil function with the normalized radius of unity and is given by

$$P(r) = \begin{cases} 1, & \rho < 0, \\ 0, & otherwise. \end{cases} \tag{1.16}$$

for a uniform circular pupil.

Taking the modulus squared of Eq. (1.15) results in the intensity in the focal plane:

$$I(\nu) = (\pi N)^2\left[\frac{2J_1(\nu)}{\nu}\right]^2 \tag{1.17}$$

Eq. (1.17) is called the Airy pattern of a lens and is shown in Fig. 1.4(a). The intensity distribution, normalized by the maximum intensity, along the radial direction is depicted in Fig. 1.5(a). Approximately 80% of the incident energy is confined to the central bright spot. The position at which the intensity drops to zero is approximately ν = 3.83. Recalling Eq. (1.12), we can conclude that the central spot size is inversely proportional to the numerical

aperture and directly proportional to the incident wavelength. These properties are important in determining image resolution: the smaller the central spot the higher image resolution. To understand the diffraction pattern in a defocus plane by a circular lens, we substitute Eq. (1.9) into Eq. (1.7) and use polar coordinates, yielding

$$U_3(r_3) = \frac{i}{\lambda z} exp(-ikz) exp\left(-\frac{i\pi r_3^2}{\lambda z}\right)$$

$$\int_0^\infty P(r_2) exp\left[\frac{ikr_2^2}{2}\left(\frac{1}{f}-\frac{1}{z}\right)\right] J_0\left(\frac{2\pi r_2 r_3}{\lambda z}\right) 2\pi r_2 dr_2 \qquad (1.18)$$

where the incident amplitude U_0 has been assumed to be unity without losing generality. To simplify it, we let

$$P(r_2, z) = P(r_2)\exp\left[\frac{ikr_2^2}{2}\left(\frac{1}{f}-\frac{1}{z}\right)\right] \qquad (1.19)$$

which is called the defocused pupil function for a lens. Therefore Eq. (1.18) can be written as

$$U_3(r_3) = \frac{i}{\lambda z} exp(-ikf) exp\left(-\frac{i\pi r_3^2}{\lambda z}\right) \int_0^\infty P(r_2, z) J_0\left(\frac{2\pi r_2 r_3}{\lambda z}\right) 2\pi r_2 dr_2 \qquad (1.20)$$

As we known, Eq. (1.20) is a Hankel transform of $P(r_2, z)$. Thus the light field $U_3(r_3)$ in a defocus plane of a lens is given by a 2-D Fourier transform of the defocused pupil function for the lens. In the present situation, the following two optical coordinates can be introduced.

(a) Radial (transverse) optical coordinate ν. Because a defocus plane is considered, the definition of ν now becomes

$$\nu = \frac{2\pi}{\lambda}\frac{a}{z} r_3 \approx \frac{2\pi}{\lambda}\frac{a}{f} r_3 \approx \frac{2\pi}{\lambda} r_3 \sin\alpha \qquad (1.21)$$

(b) Axial optical coordinate u:

$$u = \frac{2\pi}{\lambda} a^2 \left(\frac{1}{f}-\frac{1}{z}\right) \approx \frac{2\pi}{\lambda} \Delta z \frac{a^2}{f^2} \qquad (1.22)$$

Using ν and u in Eq. (1.20) and expressing U_3 as an explicit function of the defocus distance *u* gives

$$U_3(\nu, u) = 2iN exp(-ikf)\exp\left(-\frac{i\nu^2}{4N}\right) \int_0^1 P(\rho) exp\left(\frac{iu\rho^2}{2}\right) J_0(\nu\rho)\rho d\rho \qquad (1.23)$$

,where $\rho = r_2/a$.

For a lens of a uniform circular aperture, Eq. (1.23) reduces to

$$U_3(v,u) = 2iNexp(-ikf)\exp\left(-\frac{iv^2}{4N}\right)\int_0^1 exp\left(\frac{iu\rho^2}{2}\right)J_0(v\rho)\rho d\rho \tag{1.23}$$

This is an expression giving the 3-D distribution of the diffraction pattern near the region of the focal plane. In general, $U_3(v,u)$ can be expressed by Lommel function or evaluated by numerical integration. When $u = 0$, i.e. when the observation plane is at the focus, the in-focus intensity is given by Eq. (1.17), as expected. When $v = 0$, the intensity along the axil direction becomes

$$I(v=0,u) = |U_3(v=0,u)|^2 = (N)^2\left[\frac{\sin(u/4)}{u/4}\right]^2 \tag{1.24}$$

,which is plotted in Fig. 1.4(b), after it is normalized by the maximum intensity. As may be expected the intensity is symmetric with respect to the focal plane at $z = f$. Another property from Fig. 1.4 is that the axial size of the diffraction spot is approximately three times larger as the transverse size.

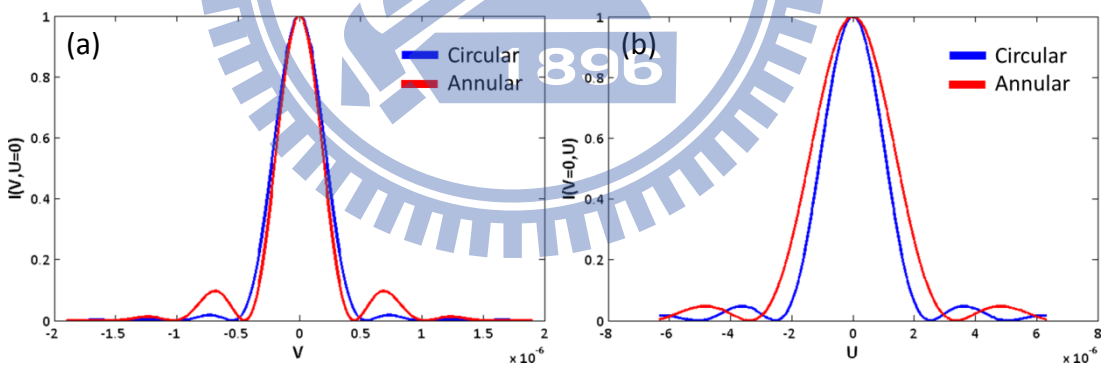

Fig. 1. 4 Intensity distributions, normalized by the maximum intensity, along the radial direction in the focal plane (a) and along the optical axis (b) for a circular lens and an annular lens (ε=0.5).

1.1.2 Annular Lens: Amplitude Only Partition

An annular lens means that a circular opaque disk is co-axially placed in the aperture of

a lens, so that the pupil function an annular lens is given by

$$P(r) = \begin{cases} 1, & \varepsilon < \rho \le 1, \\ 0, & otherwise. \end{cases} \tag{1.25}$$

,where ε is the radius of the central obstruction normalized by the radius of the lens aperture, a. Using Eq. (1.25) in Eq. (1.23) yields

$$U_3(v,u) = 2iNexp(-ikf)\exp\left(-\frac{iv^2}{4N}\right)\int_{\varepsilon}^{1} P(\rho)exp\left(\frac{iu\rho^2}{2}\right)J_0(v\rho)\rho d\rho \tag{1.26}$$

The light field in the focal plane ($u = 0$) becomes

$$U_3(v,u=0) = iNexp(-ikf)\exp\left(-\frac{iv^2}{4N}\right)\left\{\left[\frac{2J_1(v)}{v}\right] - \varepsilon^2\left[\frac{2J_1(\varepsilon v)}{\varepsilon v}\right]\right\} \tag{1.27}$$

,while the light field along the axis ($v = 0$)becomes

$$U_3(v=0,u) = iN(1-\varepsilon^2)exp(-ikf)\left\{\frac{\sin[u(1-\varepsilon^2)/4]}{u(1-\varepsilon^2)/4}\right\} \tag{1.28}$$

The result in Eq. (1.28) shows that the depth of focus for an annular lens is larger than that for a circular lens ($\varepsilon = 0$). In the case of a thin annular lens, i.e. when $\varepsilon \to 1$,

$$U_3(v,u) \propto iNexp(-ikf)\exp\left(-\frac{iv^2}{4N}\right)J_0(v) \tag{1.29}$$

, which implies that the intensity along the propagation direction for a thin annular lens is constant. The physical reason for the generation of Eq. (1.29) is that the diffracted beam from a thin annular lens includes a plane wave propagating only at one angle determined by the numerical aperture of the lens. A beam described by Eq. (1.29) is called diffraction-free beam because it can keep its size along the propagation direction, which can also be produced by an axicon. A diffraction-free beam plays an important role in optical microscopy due to its large depth of focus.

As an example, the intensity distribution for an annular lens of ε = 0.5, the intensity distributions along the radial and axial directions are shown in Fig. 1.4. These figures clearly show that the depth of focus for an annular lens is much longer than that in Fig. 1.4 for a circular lens. Furthermore, the full width at half maximum in the focal plane for an annular lens is reduced, which means that transverse resolution with an annular lens is higher than

that with a circular lens.

1.1.3 Doughnut Lens: Phase Only Partition

The doughnut lens considered here is a circular lens masked by a spatial phase filter which can change the phase of an incoming beam by integer multiple of 2π in the transverse plane. The mask can be placed in the aperture plane of the lens or in the front focal plane of the lens. In either case, the effective pupil function for a doughnut lens is given by

$$P(r) = \begin{cases} exp(in\phi), & \varepsilon < \rho \leq 0, \\ 0, & otherwise. \end{cases} \tag{1.30}$$

,where n is called the topological charge of the singularity. Eq. (1.30) means that the phase of the incident beam is changed by $2\pi n$ around the center of the lens. As expected, the intensity along the axis is zero. This is why a lens described by the pupil function in Eq. (1.30) is called the doughnut lens.

Eq. (1.30) cannot be substituted directly into Eq. (1.23) due to the angle dependence in the pupil function. Using two polar coordinate systems in the lens plane and in the observation plane, respectively, in Eq. (1.7) and normalizing the radial coordinate by a gives

$$U_3(v, \Psi, u) = \frac{iNexp(-ikf)}{\pi} exp\left(-\frac{iv^2}{4N}\right)$$
$$\int_0^{2\pi}\int_0^1 p(\rho,\varphi) exp\left(\frac{iu\rho^2}{2}\right) exp[iv\rho\cos(\varphi - \Psi)]\rho d\rho d\varphi \tag{1.31}$$

,where v and u are given by Eqs. (1.21) and (1.22). Here φ and Ψ are polar angles in the lens plane and in the observation plane, respectively. However, there is no analytical solution to Eq. (1.30).

1.1.4 The Focus Affected by the Pupil Engineering

At pervious sections, it shows that the diffraction pattern of a lens in the case of a

uniform illumination is an Airy pattern. Approximately 80% of the incident energy is confined to the central bright spot. The position at which the intensity drops to zero is approximately $\nu = 3.83$. The central spot size is inversely proportional to the numerical aperture and directly proportional to the incident wavelength. In addition, the axial size of the diffraction spot is approximately three times larger as the transverse size.

Following, we introduced two kind of pupil engineering by means of amplitude (annular illumination) and phase (doughnut lens) modulation for observing the response of focus distribution in the vicinity of the focal point. Former one is amplitude only modulation at the entrance pupil. It shows that the depth of focus for an annular lens is much longer than that with a circular lens. Also, the full width at half maximum in the focal plane for an annular lens is reduced, which means that transverse resolution with an annular lens is higher than that with a circular lens. As a conclusion for annular illumination, it provides a smaller focus spot at main lobe and longer depth of focus, which is great for non-diffraction imaging application. Therefore, the depth resolution is reduced in imaging with annular apertures, leading on the other hand to a larger depth of focus [1]. However, it consists of many bright rings encircling the central maximum and thus having a diminishing effect on the image contrast [2].

Later one is phase only modulation at the entrance pupil which demonstrates a great example for manipulating amplitude at the focus by means of phase modulation. A plane wave which has a phase singularity means that there exists a phase change of $2n\pi$ around a point in a transverse plane. Since the phase at that point is not defined, its intensity must be zero, which forms a doughnut structure of the intensity in the transverse plane. It has been found that an optical singularity beam has various applications, such as optical tweezers and the de-excitation beam of stimulated emission depletion microscopy [3, 4]. Besides, some researchers utilized binary phase with phase step of π, to improve the issue of pupil transmittance on annular illumination, and the side lobe can be suppressed by optimized the

spacing of concentric binary phase. The simplest system of this kind is the well known Fresnel zone plate, which produces a focusing effect in the different orders, according to the principle of grating diffraction.

In contrast, nun-uniform illumination based on higher order Gaussian illumination provides a powerful method to suppress the secondary maxima, so-called apodization technique. Based on this method, smaller side lobes occurs when the exponent parameter m of super-Gaussian profile function is 2, which results in the conventional Gauss profile. As a result, the field distribution at the focus is Gaussian profile which completely inhibits the existence of side lobes but the main peak become border than usual. With increasing m, the distribution increasingly takes the shape of a top hat profile with a very large slope at the boundary and results in the point-spread function becomes more and more similar to Airy pattern. Furthermore, one can pursue complex pupil function to modulate amplitude and phase of the pupil function at the same time, which gives a customized focus design for different applications based on the iterative calculation.

In general, the field distribution presented at the pupil plane can be represented as

$$\vec{U}(x,y) = A_x(x,y)exp[-iP_x(x,y)]\hat{x} + A_y(x,y)exp\big[-iP_y(x,y)\big]\hat{y} \quad (1.32)$$

, where $A_i(x,y)$ and $P_i(x,y)$ respectively represent the amplitude and phase distribution at the pupil plane, and footnote i is the polarization coordination. So far, all of the pupil engineering methods that mentioned above are based on the manipulation of phase and amplitude. They are based on the scalar diffraction assumption which does not take the effect of polarization into consideration. This is because the polarization effect can be ignored when the numerical aperture of an optical system is small, so-called paraxial approximation. When the numerical aperture of an optical system increased, larger than 0.6, the polarization effect should be taken into consideration. The depolarization effect do play an important role in which they introduce additional projection on electric filed from transverse plane to axial plane. As a result, they yield the redistribution on the weighting of

different polarization at the focal plane. Although it bring us complex relation between the pupil plane and the focal plane, but this effect gives us additional freedom to manipulate the field distribution, especially for an optical system with high numerical aperture. The depolarization effect is based on the theory of vectorial debye diffraction which will be discussed in the next section.

1.2 Vectorial Debye Theory

When vectorial properties of electromagnetic fields are considered, the fields cannot be treated as scalar, it means that the different component of electric fields will couple into each other, the phenomenon is so-called depolarization. Especially in the higher numerical aperture objective system, depolarization effect is more obvious.

In order to confirm this effect, we assume a linear polarized incident light which along the x-axis. For the polar coordinate

$$E_i(r) = P(r)cos\varphi a_\rho - P(r)sin\varphi a_\varphi \tag{1.33}$$

The $P(r)$ is the amplitude distribution within the lens aperture, a_ρ and a_φ is the unit vectors in ρ and φ directions. As depicted in Fig 1.5. Then utilized the vectorial Debye integral

$$E(P_2) = \frac{i}{\lambda}\iint_\Omega E_0(P_1)\exp(-is\cdot R)\,d\Omega \tag{1.34}$$

The $E(P_2)$ is an electric fields at point P_2 in the focal region of an objective and the $E_0(P_1)$ at point P_1 on the reference sphere surface. Therefore the P_1 and P_2 are represented by spherical and polar coordinate system respectively. The origin of each system is located at O.

$$\text{position } P_1 = \begin{cases} x_1 = fsin\theta cos\varphi \\ y_1 = fsin\theta sin\varphi \\ z_1 = \quad -fcos\theta \end{cases}, \begin{matrix} f^2 = x_1^2+y_1^2+z_1^2 \\ r_1^2 = x_1^2+y_1^2 \end{matrix} \tag{1.35}$$

$$\text{position } P_2 = R = \begin{cases} x_2 = r_2 cos\Psi \\ y_2 = r_2 sin\Psi \\ z_2 \end{cases}, \quad r_2^2 = x_2^2 + y_2^2 \tag{1.36}$$

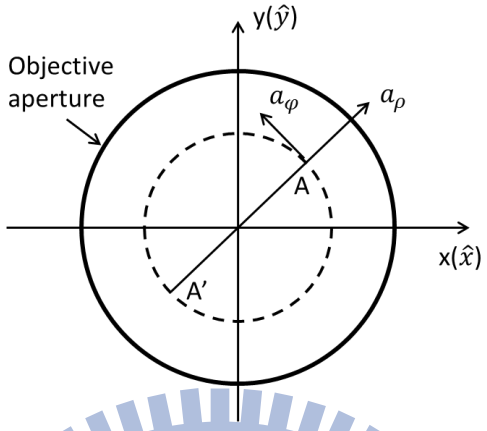

Fig. 1. 5 The schematic diagram of a_ρ, a_φ, $\hat{x}$ and $\hat{y}$.

The unit vector s can be written as

$$s = sin\theta cos\varphi\hat{x} + sin\theta sin\varphi\hat{y} + cos\theta\hat{z} \tag{1.37}$$

The $\hat{x}$, $\hat{y}$ and $\hat{z}$ are unit vectors in x, y and z direction, then the Eq. (1.33) can rewritten as

$$\mathrm{E}(r_2, \Psi, z_2) = \frac{i}{\lambda}\iint_\Omega E_0(\theta, \varphi)$$
$$\exp[-ikr_2 sin\theta\cos(\varphi - \Psi) - ikz_2 cos\theta] sin\theta d\theta d\varphi \tag{1.38}$$

Considering the refraction of the wave on A-A' plane, as shown in Fig 1-5 the $P(r)$ is converted to $P(\theta)$, then, Eq. (1.33) become

$$E_0(\theta, \varphi) = E_i(\theta, \varphi) = P(\theta)cos\varphi a_\rho - P(\theta)sin\varphi a_\varphi$$
$$= P(\theta)\{[cos\theta + sin^2\varphi(1 - cos\theta)]\hat{x}$$
$$+cos\varphi sin\varphi(cos\theta - 1)\hat{y} + cos\varphi sin\theta\hat{z}\} \tag{1.39}$$

We substitute Eq. (1.39) into the Eq. (1.38), leading to

$$E(r_2, \Psi, z_2) =$$
$$\frac{i}{\lambda}\iint_\Omega P(\theta)\{[cos\theta + sin^2\varphi(1 - cos\theta)]\hat{x} + cos\varphi sin\varphi(cos\theta - 1)\hat{y}$$
$$+cos\varphi sin\theta\hat{z}\}\exp[-ikr_2 sin\theta\cos(\varphi - \Psi) - ikz_2 cos\theta]\, sin\theta d\theta d\varphi \tag{1.40}$$

The integration with respect to φ is from 0 to 2π and θ is from 0 to α, then the electromagnetic wave in the focal region of an objective can be expressed as

$$E(r_2, \Psi, z_2) = \frac{\pi i}{\lambda}\{[I_0 + \cos(2\Psi)\, I_2]\hat{x} + \sin(2\Psi)\, I_2\hat{y} + 2icos\Psi I_1\hat{z}\} \quad (1.41)$$

The definition of three variables I_0, I_1 and I_2 is given by

$$I_0 = \int_0^\alpha P(\theta)sin\theta\,(1 + cos\theta)J_0(kr_2sin\theta)\exp(-ikz_2cos\theta)\,d\theta \quad (1.42)$$

$$I_1 = \int_0^\alpha P(\theta)sin^2\theta\, J_1(kr_2sin\theta)\exp(-ikz_2cos\theta)\,d\theta \quad (1.43)$$

$$I_2 = \int_0^\alpha P(\theta)sin\theta\,(1 - cos\theta)J_2(kr_2sin\theta)\exp(-ikz_2cos\theta)\,d\theta \quad (1.44)$$

, where the J_0, J_1 and J_2 are the zero-order, first-order and second-order Bessel functions of the first kind.

Eq. (1.41) shows the fields distribution in focal region of a higher numerical aperture objective has three components even though the incident light is only one component. We can find the vectorial properties of light can described by vectorial Debye theory, but not in scalar diffraction theory.

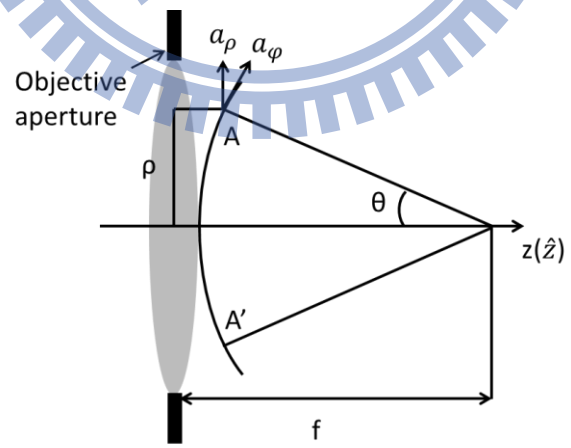

Fig. 1. 6 A side view of figure 1.5.

1.3 Thesis Structure

The aim of this thesis is to study the response of a high numerical aperture lens by means of pupil polarization engineering, especially in the polarization point of view, and to employ their focus spot toward surface plasmon steering, surface plasmon resonance based sensing, optical recording. More specifically we aim to develop several different novel schemes and concepts for different application in terms of polarization manipulation at the pupil plane. They will be discussed in this thesis.

Chapter 2: In order to develop all of the applications that mentioned above, a method for the generation of spatially inhomogeneous polarized (SIP) beam should be introduced. To this end, we proposed two methods for the generation of SIP beam which full fill the requirement of the manipulation freedom on polarization at the entrance pupil. For coherent light source, we utilized a single spatial light modulator in conjunction with an interferometer to convert linearly polarized laser beam into SIP beams. For an incoherent source, the concept of assembling polarization converter, so-called spatially varying polarizer (SVP), which consists of several polarizer plates with different orientation on transmission axis was proposed. We take the chance at the generation of polychromatic radial polarization as an example to illustrate its functionality in Chapter 5.

Chapter 3: Based on the numerical simulation, we study the field distribution in the vicinity of focal point by means of vectorial debye theory. To this end, a comparison between linear, circular and radial polarization would be given.

Chapter 4: The first application we are going to show in this chapter is a novel scheme to excite and steer long-rang propagating surface plasmon polaritons (SPPs) by means of

polarization engineering at the far field. Excited SPPs exhibit a wide range of field distribution, based on single, double, and triple excitations. Furthermore, the defocus technique provides additional freedom for excited SPPs propagating inward or outward.

Chapter 5: Here we demonstrate two kind of surface plasmon resonance (SPR) mediated sensor launched by coherent and incoherent radially polarized light. In the case of the coherent light, a refractive index step was employed for giving a proof-of-concept on the idea of interfering SPR sensor. Based on its unique sensing property which is sensitive to the change on refractive index at a 2D spatial domain, the concept of the near-field radar was proposed to show the possibility on tracing the moving orientation of a small object. Second, by employing incoherent polychromatic radially polarized light, we brought you a powerful sensor which provides a magnificent rainbow concentric ring pattern containing all SPR mediated information of a local region. By analyzing the pattern of rainbow concentric ring, we can sense the fine change on refractive index of the sample under test caused by the change of reaction, concentration, temperature…etc.

Chapter 6: Finally, we apply radial polarization for two kinds of optical data storage (ODS) system. One is to study the tracking and focusing signal as radial polarization was applied to conventional ODS. Second, we introduced radial polarization to the five-dimentional ODS system for the purpose of utilizing entire nanorods inside the recording media, which can increase the recording density at the same position.

Chapter 7: We concluded this thesis and provide suggestions for future research toward a continuation of the work presented here

Chapter II

Start from the Synthesis Methods of a Spatially Inhomogeneous Polarized Beam

In this thesis, we focus on the investigation of pupil engineering by means of polarization manipulation and its applications. For the application purpose, this thesis will not only cover theoretical parts but also experimental parts, we tried to deliver an entire concept of this subject to readers. The main topic of this thesis is going to apply pupil engineering for different applications, but the first issue coming out is “how can we generate a beam which can contain spatial varying polarization at pupil plane”. At the thesis, we called them as a spatially inhomogeneous polarized (SIP) beams. So, firstly we will dress on this issue by reviewing and analyzing existing literatures. A comparison between different methods as well as a brief introduction of individual working principle will be given in section 2.1. Then, different from current methods, we came out an idea to generate an arbitral SIP beams. The original concept, proposed schematic diagram of optical setup, and experimental results will be given in section 2.2.

2.1 Literature Review of Synthesis Methods

Spatially varying polarized beam is a kind of beam having different state of polarization at different position of a pupil plane, which is different from that of conventional state of polarization (linear, circular, and elliptical) which keeps the consistency of polarization among entire pupil plane. SIP beams are attracting much attention owing to contained distinguishing

feature of complex polarization configuration at the pupil plane. As a result, it brings many applications by means of tight focusing scheme using high numerical aperture (NA) objective. This process leads to depolarization effect which can produce alternative field distributions at the focal point controlled by pupil polarization engineering. It stimulates some interesting phenomena and valuable applications in the fields of the interaction between light and materials and these phenomena are more apparent as material is formed by nanostructure or operated at sub-wavelength region.

In terms of polarization distribution, radial and azimuthal polarizations are two of the most well know SIP beams which feature varying polarization at different pupil position but at the same time they also keep rotational symmetry. According to this unique feature some researchers called them cylindrical vector (CV) beams [5]. Due to their polarization arrangement matched with the circular aperture of a normal lens, the field distributions of their focus maintain circle shape all the time even under the situation of strong focusing [6]. In general, both active and passive method are able to generate CV beam. Active method is to generate CV beam directly from a laser resonant cavity with special design, passive method on the other hand, is to use external optical elements to convert the state of polarization from a linear polarized beam to a CV beam. Former one is complex with less flexibility but has pure mode quality. In contrast, later is practical to most of apply situation but has lower beam quality and lower transfer efficiency.

2.1.1 Active Method

The radially polarized (RP) doughnut mode can be represented as

$$RP = HG_{10}\vec{n}_x + HG_{01}\vec{n}_y \tag{2.1}$$

Here HG_{ij} denotes the Hermite-Gauss (ij) mode. Substituting for the HG_{10} and HG_{01} we have the radial mode given as

$$RP = E_0 \left\{ \frac{2x}{w_0} e^{\frac{-(x^2+y^2)}{w_0^2}} \vec{n}_x + \frac{2y}{w_0} e^{\frac{-(x^2+y^2)}{w_0^2}} \vec{n}_y \right\} \quad (2.2)$$

Here E_0 is just a constant factor describing the magnitude of fields and w_0 is the parameter that determines the diameter of the mode. Also, the azimuthally polarized (AP) mode can be represented as

$$AP = -HG_{01}\vec{n}_x + HG_{10}\vec{n}_y \quad (2.3)$$

$$AP = E_0 \left\{ -\frac{2y}{w_0} e^{\frac{-(x^2+y^2)}{w_0^2}} \vec{n}_x + \frac{2x}{w_0} e^{\frac{-(x^2+y^2)}{w_0^2}} \vec{n}_y \right\} \quad (2.4)$$

Based on the mode equations, it is awarded that RP and AP is composed by Hermite-Gauss modes added with different states of polarization. Therefore, a straight forward way to generate RP and AP is to create high order Gaussian mode first then superpose them to each other. Besides, the polarization structure of RP and AP can be described by using radial direction for RP and circumferentially direction for AP in a cylindrical coordinated system which are orthogonal to each other.

In 1972, Y. Mushiake *et al*. reported the first experimental demonstration of the generation of a radially polarized beam mode by the oscillation of an He-Ne gas laser operated at 0.633 μm [7]. They used a new type of gas laser tube that has no polarizing effect which was normally caused by Brewster windows. Also, they introduced an ordinary flat mirror of the subresonator and a mode selector. The mode selector is essentially a conical thin dielectric film fabricated over a conical surface of a glass substrate. The transmittance of this thin film was designed for having higher transmission in radially polarized component and having less transmittance in circumferentially polarized component. With proper align and precision control, RP and AP can be generated via a laser oscillator. Instead of conical thing coating, a complex Brewster windows was implemented, but they found to be complicated and involver practical difficulties [8]. In 1999, a special polarization-sensitive diffraction mirror was use to purify radial polarized component [9].

This method is practical but provides low polarization extinction ration and the fine feature on the diffraction mirror is wavelength dependence which may be difficult to implement at short wavelength. Therefore, various methods were proposed to overcome these issues by means of intracavity calcite telescope structure [10], phase plate [11], and thermally stressed isotropic laser rods [12].

The generation method based on the oscillation of laser cavity provides several advantages, including pure mode structure, high beam quality, and high energy efficient. But those benefits all stand on the precise control and proper align. In addition, without the support of commercialized radially polarized laser, it is not practical for lab to implement.

2.1.2 Passive Method – Single Element

Linear polarized laser is the most common using laser source in an optical laboratory. It would be great if someone can come out an idea to generate CV beams by converting the state of polarization from linear to radial or azimuthal polarization. Based on our literatures review, the concept of turning linear polarization into radial polarization is the mainstream according to the total number of published paper. Those proposed ideas also can be classified into two kinds, one is using single optical element to radial polarized beam, and the other is based on interferometric configuration.

The first single optical element transform method was proposed by S. Quabis in 2005 [6, 13]. This method is based on an approximate device instead of a continuous spatially varying retarder [14, 15]. It consists of four quadrant sectors of half-wave-plates, each one with different orientation identical to the optical axis of crystal plate. It is a simple device but the transformation efficiency of this converter is 75%[14]. Therefore, A. K. Spilman *et al.* increased the number of sectors by a factor of two which improved the polarization quality

[16-18]. In addition, a simple method is also proposed by using conic polarization device [19]. However, the generation concept is based on an approximate method which would let non-transformed power go to higher order mode. As a result, an additional confocal Fabry-Perot resonator which is operated as a mode cleaner and eliminates high frequency noise of sharp boundaries between each sector is required. Although the segmented spatially varying retarder provides a good performance as the number of plate is large enough, it is still not as good as laser cavity generated CV beams due to the number of the retarder is finite in practical.

According to this intrinsic issue, Hongwen Ren apply the property of liquid crystal to form a polarization converter with continues polarization change [20]. Liquid crystal (LC) is a strong contender as a polarization converter because its directors can be reoriented by an electric field. The action of liquid crystal can be explained in the following way. In general, the light polarization direction will follow the LC director orientation. By making use of such a characteristic, one can easily design a LC cell with two sides of substrate having different rubbing direction; top side is a homogeneous rubbing alignment, and the bottom side is a radially rubbing direction. Also, if a radial electric filed is applied, then the LC directors on the bottom substrate will present radial orientation. Therefore, a linearly polarized light becomes radially polarized light as passing through this LC cell. Due to the simplicity of this structure and freedom of voltage control, LC cell has been commercialized (ARCoptix, Radial-Azimuthal Polarization Converter) and has been widely accepted in practical use.

2.1.3 Passive Method – Interferometer

Different from the generation of CV beam through a single optical element, interferometer configuration also provides a similar capability to generate CV beams by means of superposition. From Eq. 2.1 and Eq. 2.3, we do know RP and AP can be treated as

the superposition of two first order Hermite-Gauss modes having orthogonally linear polarized light. In optical, an interferometer is a perfect platform to perform superposition. If we can generate first order Hermite-Gauss modes from a linear polarized simple Gaussian mode, then later we can add them together via an interferometer.

In 2005, Nicolas Passilly *et al.* utilized a simple interferometric tecunique for converting a linearly polarized Gaussian beam into a radially polarized donught beam [21]. This experiment accomplished the coherent summation of two orthogonally polarized TEM_{01} and TEM_{10} beams that are obtained from the transformation of a TEM_{00} beam by use of a simple binary diffractive optical element. This binary diffractive optical element is a phase step of height h etched in a thin polymer film having refractive index n and deposited on a glass plate. This step produces a phase shift $\phi = 2\pi h(n-1)/\lambda$ between the two parts of the laser beam illuminating the polymer edge. When the phase difference between the two parts is multiple of half wavelength, then transmitted beam would be converted into a high order beam having the same state of polarization but oscillates at opposite direction due to the difference of initial phase on two parts. As the light propagated to the far-field, the sharp phase edge induced polarization singularity would result in an intensity distribution having two lobes on each side and no intensity at the middle boundary which is the iconic feature of Hermite-Gauss modes. Then, an azimuthal or radial polarized beam is generated by using an optical based on a superposition platform.

Obviously, Mach-Zehnder interferometer is the most common setup to perform this operation, also other types of interferometer such as Sagnac interferometer is also been proposed [22]. For the purpose to generate Hermite-Gauss modes from linear polarized beam, some researches replace fixed phase plate with spatial light modulator which has better flexibility to manipulate phase distribution. In 2005, Baohua Jia *et al.* utilized the combination of single liquid crystal display and Mach-Zehander interferometer to synthesis radially polarized light [23], which provides a possibility of dynamitic control.

2.2 Synthesis of Arbitral SIP Beams

The polarization configurations mentioned above are individually proposed by different types of method via delicate optical design in conjunction with step phase plate, segmented quarter wave plate, liquid crystal, spatial light modulator, spiral phase plate, interferometer, or designed resonator cavity [11, 15-17, 21-26]. However, these proposed methods only designed for generating a specific kind of SIP beams. It lacks the flexibility for researchers to change the polarization structure of generated SIP beams for different purpose in a fixed optical setup. Therefore, it is indeed necessary to come out a method which is able to generate adjustable SIP beams in a fixed optical setup.

Different to the work of I. Iglesias *et al.* [19, 26], we proposed a new algorithm which can generate arbitral SIP beams composed of whole combination of linear polarization with different in-plan orientation. Also, adjustable SIP beams were experimentally demonstrated via an interferometer structure in conjunction with the advantages of spatial light modulator in high dynamical control and high resolution. The algorithm of synthesized SIP beams and its implementation will be shown in the following sections.

2.2.1 Synthesis Algorithm

In order to describe clearly, the theory of our method to synthesize SIP beams will be began illustrating with mathematical formulas and taking decomposed radial polarization as initial example. Our method is based on superposition method, so-called interference method in reference to interferometer, which can be classified into two kinds according to operating polarization. As like Gaussian modes, radial polarization is one kind of solutions of wave equation owing to its field distribution is the combination of two orthogonally linear polarization of Hermite-Gaussian (HG) beams or two orthogonally circular polarization of

Laguerre-Gaussian (LG) beams. As neglecting the time depended features and simplify complex amplitude of the equation, radial polarization can be respectively described in forms of Eq. (2.5) or Eq.(2.6).

$$\vec{\mathrm{E}}_{total}(x,y) = HG_{1,0}\hat{x} + HG_{0,1}\hat{y}$$

$$\vec{\mathrm{E}}_{total}(r,\phi) = \mathrm{E}_{\mathrm{HG}_{10}}(\mathrm{r})\cos(\phi)\,\hat{\mathrm{x}} + \mathrm{E}_{\mathrm{HG}_{01}}(\mathrm{r})\sin(\phi)\,\hat{\mathrm{y}} \tag{2.5}$$

$$\vec{\mathrm{E}}_{total}(x,y) = LG_{0,1}(\hat{\mathrm{x}} - \mathrm{i}\hat{\mathrm{y}}) + LG_{0,-1}(\hat{\mathrm{x}} + \mathrm{i}\hat{\mathrm{y}})$$

$$\vec{\mathrm{E}}_{total}(r,\phi) = \mathrm{E}_{\mathrm{LG}_{01}}(\mathrm{r})\mathrm{e}^{\mathrm{i}\phi}(\hat{\mathrm{x}} - \mathrm{i}\hat{\mathrm{y}}) + \mathrm{E}_{\mathrm{LG}_{0-1}}(\mathrm{r})\mathrm{e}^{-\mathrm{i}\phi}(\hat{\mathrm{x}} + \mathrm{i}\hat{\mathrm{y}}) \tag{2.6}$$

where $\vec{\mathrm{E}}_{total}$ is the field distribution of radial polarization, HG and LG are the field distribution of Hermite-Gaussian and Laguerre-Gaussian, the suffix (n,m) of HG or LG represents the order and degree of the beam, and E_{HG}, E_{LG} represent the complex field distribution. The major difference between these two approach methods is the constituent of polarization rather than the field distribution. Therefore, one can say that both linear and circular polarization could produce desired radially polarized beam with proper tailored amplitude and phase distribution.

Referring to Eq. (2.5), two orthogonal linear polarizations are set as base elements of radial polarization. The trigonometry functions of cosine and sine mimic the intensity distribution of HG_{10}, and HG_{01}, respectively. Moreover, these trigonometry functions provide a negative number which ensured the corresponding electric fields could oscillate with opposite direction. For example, the field distribution of first part of Eq. (2.5) has two separated lobes of amplitude divided by y-axis and two contra-oscillated x-linear polarizations. Although linear polarization approach is a straight forward thinking, it remains a drawback that one should modulate not only phase but also amplitude simultaneously, and this resulted in the need of complex optical setup. Even though some researches tried to use phase element only and ignored the requirement of tailored amplitude which yielded the quality of polarization neither lack symmetry nor without continuous [27].

In contrast, the key idea of circular polarization approach is to imitate the field

distribution of LG. The feature of LG is a continuous spiral distribution in phase term. Therefore, this feature can easily reproducevia a phase delay element. As propagating for a certain distance larger than Fraunhofer region, the amplitude of uniform beam will gradually change to form donut shape which is the amplitude feature of LG mode due to the phase singularity. With proper superposition between two of the circular polarizations, the spiral phase of LG individually retards the phase of circular polarization at different location and yields radial or azimuthal polarization. In practical, circular polarization approach is more effortless than linear polarization approach due to the requirement of less optical elements.

Based on circular approach, we further extend this idea to form a new algorithm of synthesis arbitral SIP beams. As shown in Eq. (2.6), neglecting constant value of E_{LG}, the states of polarization along the same azimuthal angle are identical. We can alter the positions of polar coordinate to Cartesian coordinate. The total polarization structure of SIP beams can be described in a summation, shown as

$$\vec{E}_{total}(x,y) = \sum_{i,j=1}^{n} \vec{E}_{local,ij}(xi,yj) \tag{2.7}$$

$$\vec{E}_{local}(xi,yj) = \frac{1}{\sqrt{2}}\begin{bmatrix}1\\ j\end{bmatrix} e^{-j\Delta} + \frac{1}{\sqrt{2}}\begin{bmatrix}1\\ -j\end{bmatrix} e^{-j\Delta} = \frac{1}{\sqrt{2}}\begin{bmatrix}\cos(\Delta)\\ \sin(\Delta)\end{bmatrix} \tag{2.8}$$

where $\vec{E}_{total}(x,y)$ is the field distribution of SIP beams, Δ is the phase delay term bounded within ±π. Utilizing the feature of easy operation in Jones Calculus, the total field distribution of Eq. (2.7) is composed of individual state of polarization at different location in the pupil plane, as shown in Eq. (2.8). The polarization type of a division is determined by the superposition of the left and right-hand circular polarization multiplied by a specific phase delay. According to the calculated result of this combination, it can further be reduced to a linear polarization with equal amplitude but different rotated angle Δ. Therefore, one can synthesize an arbitrary SIP beam consisted by a series of summation of locally presented linear polarization having individual oscillation direction. This method has advantages of providing identical amplitude and whole linear polarization based assembling. Also this is

differ from the work of other research whose assembling components was various and resulted in complex as interpreting the result of focused spot [26], and that generating idea still remains in theoretical phase.

By adapting the advantage of circular polarization approach, one can generate SIP beams external the laser cavity by altering the state of polarization via controlling the phase distribution of both sides of circularly polarized beams. In practical, commercial product of spatial light modulator (SLM) is appropriate to control individual phase delay within a desired region. Figure 2.1 shows the diagram of generating arbitrary SIP beams through orthogonal circular polarization and segmented spatial phase distribution. The SLM serviced as customized phase plate providing flexibility and high dynamitic control. While an expended circularly polarized beam reached the SLM, its phase distribution will be changed from uniform to particular format depended on the relation shown in Eq. (2.8). Two orthogonal polarized beams carried specific phase information and yield desired SIP beams after superposition. Following, the experiment results of synthesis of SIP beams will be given.

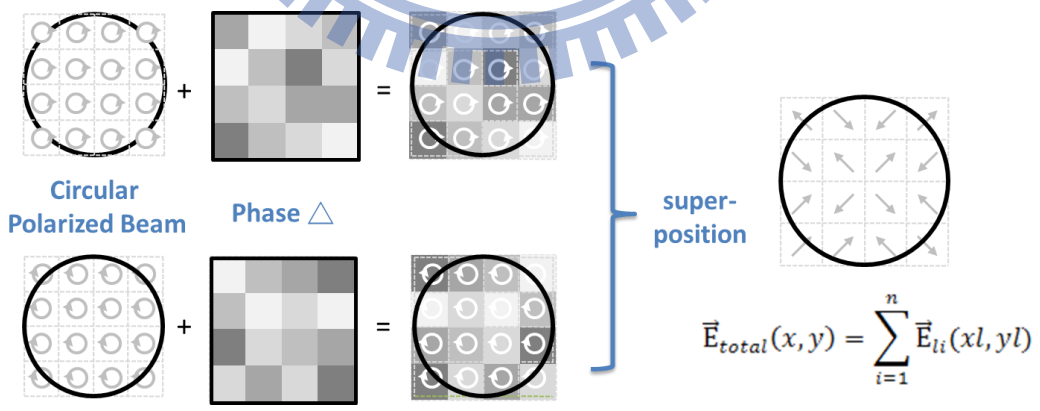

Fig. 2. 1 The diagram of generating arbitrary SIP beams through orthogonal circular polarization and segmented spatial phase distribution.

2.2.2 The Optical Setup

Figure 2.2 shows the experimental setup of the SIP beams generating system. A continuous wave of a 632.8nm He-Ne laser beam was used through this experiment. Its output was expended via a beam expender and propagated toward the spatial light modulator (HOLOEYE LC-R2500). The phase distribution of SLM was controlled by personal computer providing phase information. As expended light reflected from the SLM, its phase distribution of wave front changed from uniform to a specific pattern given from SLM. Then reflected beam was guided into an interferometer and create two truncated beams via diaphragm of the two arms of interferometer. Both of them converted from linear polarization to mutual-contrary circular polarizations via a set of polarizer and quarter wave

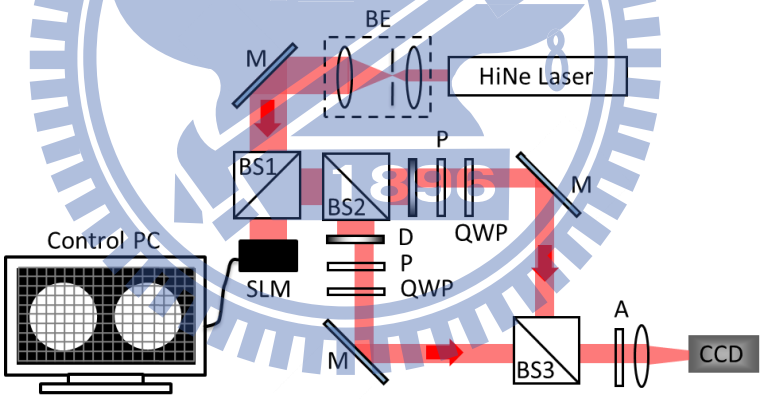

Fig. 2. 2 The schematic diagram of SIP beams generating system, where BE: beam expender, BS: beam splitter, SLM: spatial light modulator, D: diaphragm, P: polarizer, QWP: quarter wave plate, M: mirror, and A: analyzer.

plate. Although their state of polarization changed, they still reserved specific phase pattern loaded by the SLM. Finally, utilize beam splitter to perform optical superposition shown on Eq. (2.8), and then the outcome of the interferometer is a SIP beam. In short, the idea of synthesis arbitral SIP beams can be implemented through the use of interferometer structure

in conjunction with SLM, and it provides flexibility to control polarization distribution and adapts to the changing of wavelength.

Although the combination of SLM and interferometer structure provided a serious of advantages for synthesized SIP beams, these advantages came with highly accurate requirement as manipulation. Correct SIP beams only exist when two truncated beams match perfectly and propagate along identical axis. It is important and valuable to find an easy and trustable technique to calibrate the accuracy of this synthesis system. Therefore, based on ultra high sensitive of interferometer, we proposed a calibrate method utilizing interference pattern of high order optical vertex to overcome this alignment issue without changing the formation of optical configuration.

2.3 Interference Pattern of High Order Optical Vertex

An optical vertex wave is essentially a plane wave contained helical phase and it gradually changed phase distribution is suitable to exam the phase controlling ability of SLM. It math form can be described as

$$\vec{\mathrm{E}}(r,\phi,z,t) = \vec{\mathrm{E}}(r,z)\mathrm{e}^{im\phi}\mathrm{e}^{ikz-iwt} \tag{2.9}$$

where $\mathrm{E}(r,z)$ is the amplitude of plane wave, k is the wave number of a monochromatic optical wave, w is the angular frequency, and m is the topological charge of an optical vertex. The integer m can be either positive or negative which respectively represented gradual phase changing along clockwise or counter clockwise ϕ direction, and higher topological charge has stronger optical momentum as the beam propagate in the free space.

Based on our optical setup, spiral phase distribution could be loaded on two opposite circular polarizations, and they will superpose at the end of the system. Once two beams are not fully superposition, a small tilt angle θ between two beams will be introduced. Here, we set E_1 propagate along z direction and E_2 propagate along the x-z plane with a tilt angle θ respected to z axis. Therefore, each of them can be described as

$$\vec{E}_1(r,\phi,z) = E_0(r)e^{jm_1\phi}e^{-jkz}\,(\hat{x} - i\hat{y}) \tag{2.10}$$

$$\vec{E}_2(r,\phi,z) = E_0(r)e^{-jm_2\phi}\,e^{-jkz'}(\hat{x}' + i\hat{y})$$

$$\vec{E}_2(r,\phi,z) = E_0\,e^{-jm_2\phi}\,e^{-jkz\cos(\theta)}\,e^{-jkx\sin(\theta)}[\cos(\theta)\,\hat{x} - \sin(\theta)\hat{z} + i\hat{y}] \tag{2.11}$$

as two beams superposition, the result is

$$\begin{aligned}\vec{E}_{total}(r,\theta,z) &= \vec{E}_1(r,\phi,z) + \vec{E}_1(r,\phi,z)\\ &= \hat{x}E_0\left[e^{jm_1\phi}e^{-jkz} + \cos(\theta)\,e^{-jm_2\phi}e^{-jkz\cos(\theta)}e^{-jkx\sin(\theta)}\right]\\ &+ i\hat{y}E_0\left[-e^{jm_1\phi}e^{-jkz} + \cos(\theta)\,e^{-jm_2\phi}e^{-jkz\cos(\theta)}e^{-jkx\sin(\theta)}\right]\\ &+ \hat{z}E_0\left[-\sin(\theta)\,e^{-jm_2\phi}e^{-jkz\cos(\theta)}e^{-jkx\sin(\theta)}\right]\end{aligned} \tag{2.12}$$

Equation (2.12) shows the resulted total field after superposition, it contained three parts of orthogonal component. The interference pattern could be exacted via an analyzer which contain transmission axis along x-axis. As substituting $x = r\cos\phi$ into Eq. (2.12) due to the consistency of the coordinate, we can obtain

$$I_x = {E_0}^2\,[1 + \cos^2(\theta) + 2\cos(\theta)\cos((m_1 + m_2)\phi + kr\cos(\phi)\sin(\theta) + kz(\cos(\theta) - 1)] \tag{2.13}$$

Further, this can be abbreviated into

$$\begin{aligned}I_x &\cong 1 + \cos[(m_1 + m_2)\phi + kr\cos(\phi)\sin(\theta)]\\ &= 2\cos^2\left[\tfrac{1}{2}kr\cos(\phi)\,\sin(\theta) + \tfrac{m_1+m_2}{2}\phi\right]\end{aligned} \tag{2.14}$$

As the analyzer rotate 90 degree, a similar result was obtained

$$I_y \cong 2\sin^2\left[\tfrac{1}{2}kr\cos(\phi)\,\sin(\theta) + \tfrac{m_1+m_2}{2}\phi\right] \tag{2.15}$$

In Eq. (2.14), two phase terms are taken into account within cosine square function. First term is contributed by the tilted angle θ caused by the miss alignment of two truncated beams, and the other phase term revealed the total number of topological charges associated with the order of spiral phase. Further information could be obtained from Fig. 2.3 where shows various interference pattern generated by different order of spiral phase

distribution.

Various interference patterns are generated by combination of different order of spiral phase, and they are grouped into two parts: with or without tilted angle, as shown in Fig. 2.3. Color and grey pictures depicted the experiment and simulation results, respectively. The indictor m represented the number of topological charges of each spiral phase. This value could either be positive or negative. For positive value, the spiral phase gradually changed from 0 to 2π as the azimuthal angle increasing clockwise. In contrast, the spiral phase gradually changes from 2π to 0 as m is negative. In the cases of having a tilted angle, the interference figures are composed of two kinds of interference patterns: straight and bended

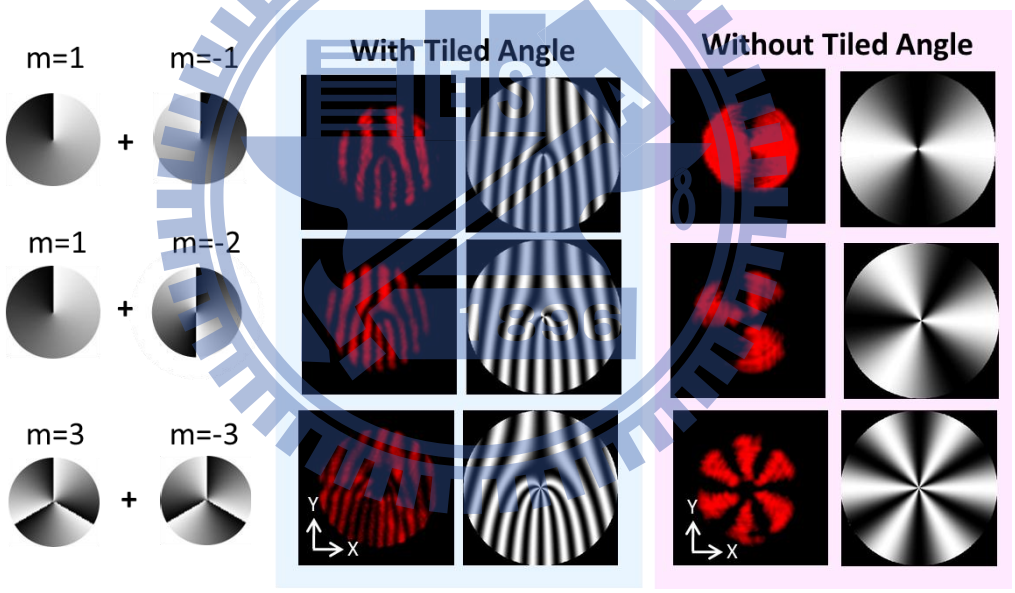

Fig. 2. 3 various interference pattern generated by different order of spiral phase distribution.

lines. Straight interference lines lay in vertical appealing from the upper edge toward lower edge of observation circle and without discontinuing. Those are contributed by the first phase term of Eq. (2.14) owing to the deviation of miss alignment. In addition, as the deviation getting larger the coefficient of this phase term became larger and resulted in a

rapidly oscillation of intensity along x-direction. Therefore, one can adjust the tilted angle of mirrors and beam splitters for calibration by observing the straight interference pattern. Interference pattern of high order vertex beam is experimentally performed via interferometer in conjunction with SLM which imply the spatial resolution of SLM is high enough for generating arbitral SIP beams.

In contrast, banded interference lines reveal a distinct feature compared to straight lines which only exists within a region from the center to the edge of the observation zone. These banded lines connected together at the center, called node, and the number of banded lines spread out from the node are identical to |m1+m2| associated with the second phase term of Eq. (2.14). Once the titled angle approaches to zero, not only the density of straight pattern decreased even absent but also the banded lines will expand the area of these lines to form separated sectors with equal size. Figure 2.4 gave us an overview of different interference figures observed at different title angles. As the titled angle become smaller, the density of straight lines becomes lower, and yields more accurate in the setup of this synthesis system. Therefore, observing the tendency of interference pattern of high order vertex beams is a reliable examination method to calibrate the accuracy of optical setup.

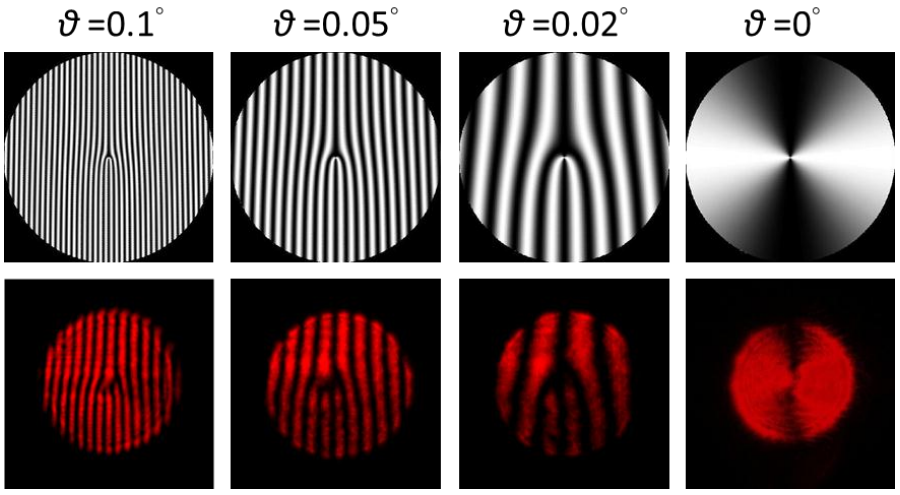

Fig. 2. 4 Different types of interference pattern at various tilted angles. Upper row

shows the simulation results, and lower row shows the experiment results. These figures gathered from the output of SIP beams generating system with an x-analyzer putting at the end.

2.4 Synthesis Results

Here, we further demonstrate others SIP beams with border definition which consists of arbitral state of linear polarization in different position as shown in Fig. 2.5. Two kinds of SIP beam with designed polarization structure: one is respectively assigned to reveal linear

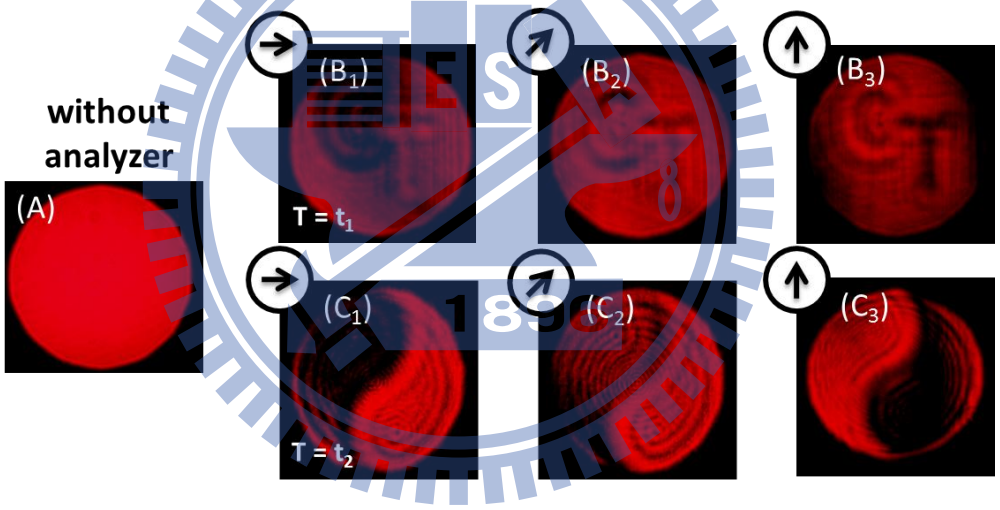

Fig. 2. 5 The intensity distribution of several SIP beams, where (A) shows uniform intensity distribution of arbitral SIP beams which embeds polarization cannot be perceived without analyzer. Grouped picture of (B_1-B_3) and (C_1-C_3) respectively shows the intensity distribution of two cases, letters 'CT' and symbol 'tai-chi', as analyzer taking apart.

polarization with orientation angle in 90, 0, and 45 degrees for the letters C, letter T, and background, as shown in Fig. 2.5(B); the other is assigned to having linear polarization with

orientation angle of 90 and 0 degrees for each half part of the symbol Tai-Chi, as shown in Fig. 2.5(C). They are changing sequentially as feeding time depended phase information on each frame. Owing to polarization varying with location, the intensity distribution of SIP beams one can observe it individual structure of polarization as rotating the analyzer. This phenomenon can refer to sub-pictures of (B) and (C) series, where the direction of arrow represents the extinct axis of analyzer. As the analyzer set horizontal as extinct axis, the strength of intensity for the region of letter C and left part of the symbol Tai-Chi will drop to zero, and appeal to it maximum as extinct axis parallel to vertical. From the figure some diffraction introduced pattern and polarization impurity slightly polluted the beam quality.

However, this minor undesired effect could be removed by utilizing optical spatial filter to reduce diffraction effect. In addition, SLM not only provide a possibility to synthesize linear polarization with 256 (8 bits in the degree of phase level) states of orientation angle but also provide a function for phase correction to eliminate the polarization impurity introduced by the phase delay of element in surface roughness.

2.5 Short Conclusion

In this chapter, we proposed a new synthesis algorithm to generate arbitral SIP beams consisted of varies state of liner polarization by means of two orthogonal circular polarizations in conjunction with individual phase distribution. This approach has successful demonstrated not only in theory but also in experiment. Thanks for the unique property of SLM, this generating system consists advantages of switching the structure of polarization by the time, neglecting the need of moving optical element, and providing abundant state of linear polarization. The interference pattern of high order vertex beam was introduced to verify the modulation ability of SLM in high resolution. Also, they act as calibration tool applying to generate the quality of synthesized SIP beams. The interference patterns of

experiment result show intense agreement with that of simulation results. In addition, the feature of dynamic adjustable SIP beams generated through our optical setup is applicable to optical tweezers for a close-loop trapping control.

Chapter III

Strong Focusing of Spatially Inhomogeneous Polarized Beam

According to the literatures, radial and azimuthal polarizations are two of the most well know SIP beams and have been apply to many applications. Although they have identical donut-shaped of intensity distribution at the pupil plane, one can find a distinguished difference by comparing the intensity distribution of their focused spot. The shape of focused spot for radial polarization is a tiny circle with about 20% smaller of radius than that of linear polarization [5, 6, 13, 15, 24, 26-43]. In contrast, the focus spot of azimuthal polarization exhibits a donut shape owing to the absence of the longitudinal component caused by the singularity of polarization along the optical axis [6, 15]. Moreover, several unique field distributions at the focal point have been demonstrated associated with delicate design of polarization structure in the pupil plane. A circle focused spot with a cross-shaped side lobe was generated via pseudoradial or segmentally radial polarization [16, 17, 21, 26, 27]. By switching the polarization of segmental SIP beams, two-fold symmetry, four-fold symmetry, and rectangular annular shape were created by the result of interference mechanism at the focal point [16, 17, 21, 26-28]. The shape of focused spot was gradually changed, from donut-shaped to flat-top-shaped then circle-shaped, by adjusting the weighting of radial and azimuthal polarization [24, 43]. In addition, these unique shapes of field distribution not only present at the focal point but also spread in the vicinity of the focal point resulting in a three dimensional focal volume. The volume size of cubed optical cage was tunable as controlling the ratio of the pupil radius to the beam radius of

double-ring-shaped radially polarized beam [38]. A horseshoe-shaped field distribution along the optical axis presented another craft of tailoring focal volume [25]. These novel field distribution have been applied to light trapping [44], performing various tiny focused patterns [24-26, 28, 32, 38, 40, 45-48], image of single molecule [49], and localized surface Plasmon excitation [50, 51].

3.1 Focusing Mechanism of Radial Polarized Beam

In this section, we employ vectorial diffraction to examine the focusing mechanism of radially polarized beams using an immersion objective with linear and circular polarized illuminations. Radial polarization features a sharp focus in a high-numerical-aperture system. The longitudinal component governing spot formation depends on the bending of the polarization vector rather than the immersion circumstance. As the marginal angle of the objective exceeds 64.16 and 71.81°, the depolarization effect of the radially polarized beam enables a smaller spot than the linear and circular polarizations, respectively.

It is well known that the focus spot in optical systems is determined by the scalar diffraction ~ kλ/NA, where λ is the free space wavelength and NA is the numerical aperture of the objective lens. The factor k is of the order unity and depends on apodization. In order to produce the smallest possible spot, it is desirable to pursue shorter wavelengths and higher NAs. However, the characteristics of vectorial behavior would be more apparent in a high-NA system and lead to an unsymmetrical focus (called elongation effect) under linear polarized illumination [52]. Recently, a doughnut-shaped optical field obtained via radial polarization (RP) attracted much attention owing to the preservation of the symmetric property of the focused spot. Such a unique feature makes it possible to apply RP in high resolution systems [6, 15, 53, 54]. Several methods have been proposed to generate such as axially symmetric polarized beam. Generally, the formation can be classified into two types.

One directly generates the beam from the laser cavity [55], the other approach involves indirect generation outside the laser cavity using the interference of two orthogonal Hermite-Gaussian modes [23, 56].

On the other hand, immersion technologies such as solid-immersion lens (SIL) yielding an effective NA (NA_{EFF}) above 1.0 also provide a route for radially polarized beams [29, 35]. In a SIL system the longitudinal component of focused radially polarized beams dominates the lateral size of the focus spot and propagates through the interface around 5-6 wavelengths [30, 57, 58]. In addition, the optical aberration caused by the air spacing can be alleviated owing to the characteristics of cylindrical symmetry. On the basis of the above mentioned features, we neglected the spherical aberration caused by air spacing and selected water as the immersion medium. The focus spot was observed in the immersion medium, and the comparisons of the focus spot with other homogeneous polarization modes were also carried out.

3.1 Simulation Condition

An ideal aplanatic system with a focusing power λ/NA_{EFF} is discussed, where $NA_{EFF} = n \times NA_{AIR}$ (n: refractive index of the focusing medium. NA_{AIR}: focused light in a dry lens which entirely depends on its angle of marginal ray). Figure 3.1 schematically shows the states of polarization on the pupil: (a) linear, (b) circular, and (c) radial polarizations, respectively. Ei and Eo represent the electric field before and after passing through the objective. The electric component at focus can be decomposed into two orthogonal components: transversal ($I_{trans} = I_X + I_Y$) and longitudinal ($I_{long} = I_Z$) components.

Figure 3.2 shows the intensity and phase distribution at focus for RP with $NA_{EFF} = 1.33$ (n = 1.33 with $NA_{AIR} = 1$), where I_X, I_Y, and I_Z denote the decomposed intensity distribution, and P_X, P_Y, and P_Z represent the corresponding phase plots for E_X, E_Y, and E_Z. The phases P_X and P_Y

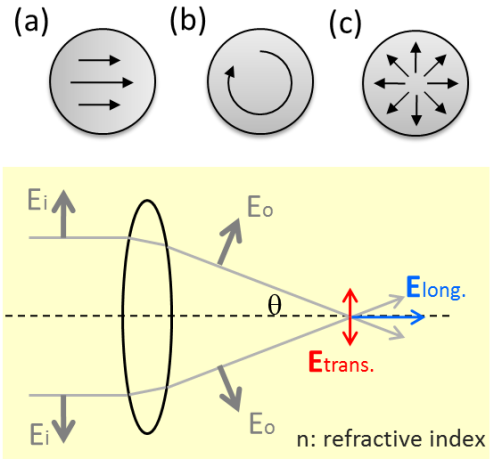

Fig. 3 1 The schematic diagram of the aplanatic focusing model and different illumination beams: (a) linear, (b) circular, and (c) radial polarization, where Ei and Eo represent the electric field of the radial polarization, $I_{long.}$ and $I_{trans.}$ represent the decomposed intensity distribution.

reveal the acquired curvature of the beam, as well as the π-phase difference between the two halves of E_X and E_Y. Whereas E_X and E_Y take the square operation, the two fold symmetry of I_X and I_Y result from the phase singularity along the y- and x-axes. The shape of the intensity distribution depends on individual phase distributions. Unlike the elongation effect from linear polarization (LP), the phase pattern P_Z of the longitudinal component of RP has concentric circles with a converging wavefront. The appreciable longitudinal component would result in a focus spot with cylindrical symmetry. Likewise, the longitudinal component of circular polarization (CP) shows a central hole in the intensity distribution caused by a continuous variation from 0 to 2π around the vortex. This donut-shaped intensity of longitudinal component ensures that the shape of the focus spot is also cylindrical with a slight spread.

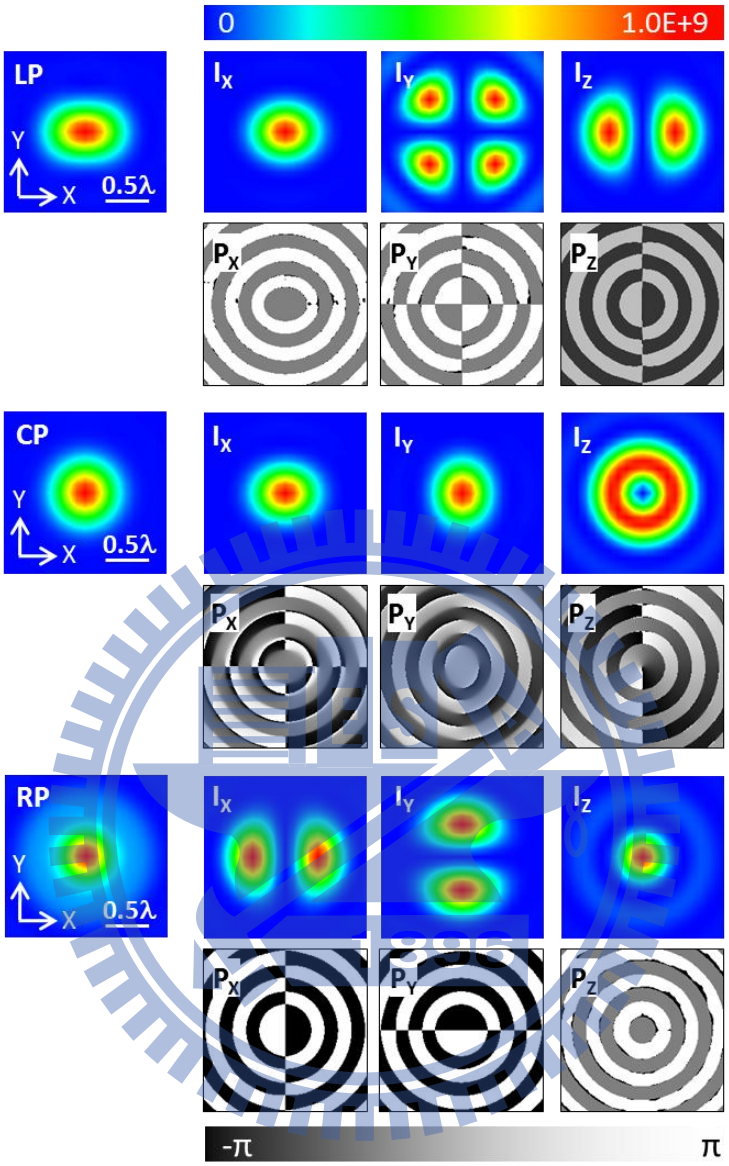

Fig. 3 2 The intensity and phase distribution of the field distribution in the focus with NA_{AIR} = 1.0 for radial polarization (RP). The I_X, I_Y, and I_Z denote the decomposed intensity distribution and P_X, P_Y, and P_Z represent individual phase distribution.

3.2 Discussion - Decomposition of focus spot

In order to further investigate the focusing mechanism of RP associated with the

immersion objective, an aplanatic focusing model was introduced, as shown in Fig. 3.1. We define a ratio of the longitudinal to transversal component as follows:

$$\mathrm{L-T\ ratio} \equiv \frac{Peak\ Intensity\ of\ Longitudinal\ Component}{Peak\ Intensity\ of\ Transversal\ Component} \qquad \text{Eq. 3.1}$$

Figure 3.3 shows the different L-T ratios of focused RP in water: (a) L-T ratio = 0.81, (b) L-T ratio = 1.38, and (c) L-T ratio = 2.94. The black solid, black dashed, and gray dashed lines

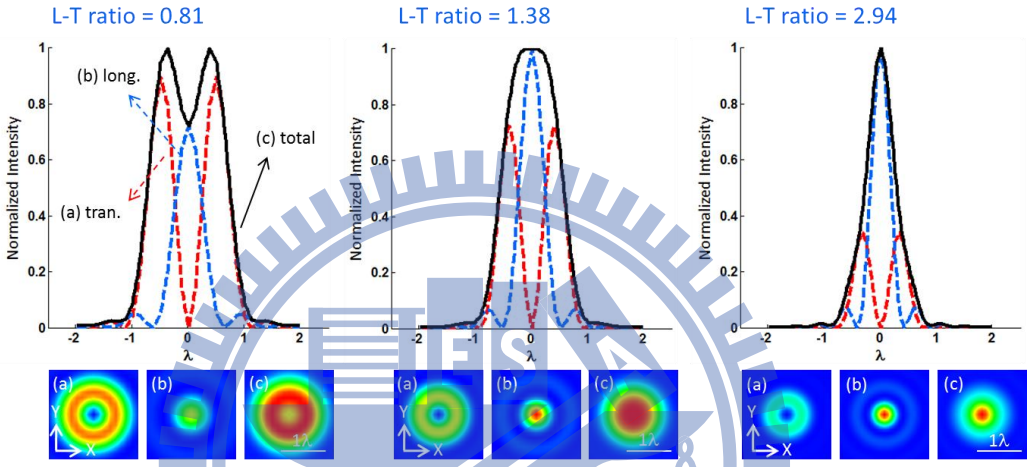

Fig. 3 3 The different L-T ratios with calculated cross-section and two-dimensional field distribution in the focus when RP beam focused by water immersion objective: (a) L-T ratio = 0.81, (b) L-T ratio = 1.38, and (c) L-T ratio = 2.94.

represent the intensity curve of total, longitudinal, and transversal components, respectively. As the L-T ratio increases, the shape of the focus spot changed from a donut-shaped spot to a circular spot. The flat-topped shape shown in Fig. 3 (b) with a L-T ratio = 1.38 is at the transition midway between above two cases. Once the L-T ratio becomes larger than the critical value, the dip in field intensity disappears; therefore, the beam shape is centralized by the considerable longitudinal component.

It must be mentioned that a high L-T ratio ensures that RP produces a smaller focus spot. The marginal angle determines the projection power of the transversal component onto the longitudinal component. That is, for RP, the shape of the focus spot entirely depends on the

bending of the polarization vector, and the refractive index merely functions as a proportional scale factor.

Figure 3.4 shows two L-T ratio curves for focusing RP with n=1.0 (dashed line) and n=1.33 (solid line). The subfigures of focus spot correspond to specific L-T ratios. Drawing a line parallel to the x-axis at L-T ratio = 1.38 separates those subfigures into two parts:

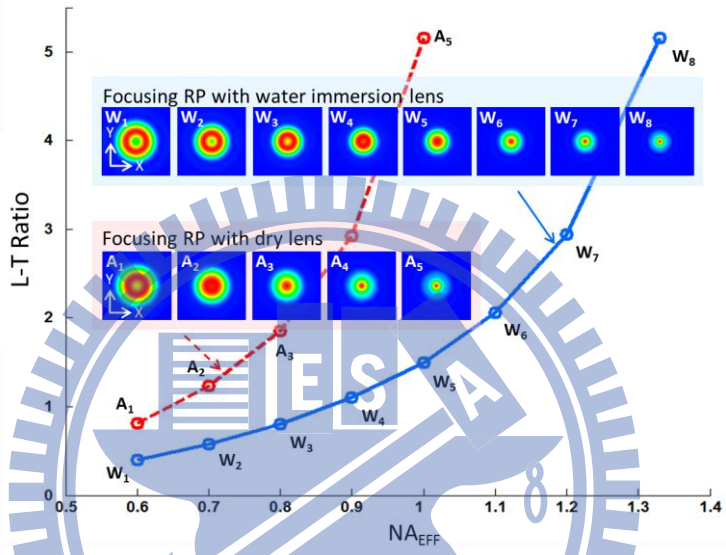

Fig. 3 4 The L-T ratio of radial polarization (RP) in the focus versus NA_{EFF} focused with dry lens and water immersion objective.

donut-shaped and circular focus spots. Two lines exhibit a common L-T ratio 5.16 at NA_{EFF} = 1.0 and 1.33 for different immersion media. The maximum solid angle of a single objective is 2π, which limits the strength of the longitudinal component projected from the transversal component. In addition, as the NA_{EFF} of the solid line is divided by the refractive index 1.33, the new line is identical to those reported in the literature [29].

3.3 Discussion - Comparison of full width at half maximum

Owing to the high L-T ratio, the shape of total field distribution at a high NA will mainly be governed by the longitudinal component. With reference to Fig. 3.5, we discuss the full

width at half maximum (FWHM) of the focusing spot in various states of polarization and immersion media. Since the refractive index of the immersion medium only provides a proportional down-scale factor, here we only address the case in air for simplicity.

Recall the L-T ratio = 1.38 shown in Fig. 3 (b), whereas NA_{EFF} > 0.73, the longitudinal to transverse component of the optical field has a critical ratio at which the optical field is transformed from a donut-shaped to a flat-topped shape. After that, the depolarization effect starts to govern the formation of the focused spot. As NA_{EFF} increases, the FWHM of RP exhibits a faster reduction and comparable to LP and CP at NA_{EFF} higher than 0.9 and 0.95, respectively. It was noted that superior radial illumination only exists in a high marginal ray. Compared with LP and CP, the smaller spot obtained by RP was under the conditions of marginal angle > 64.16° (mark 1) and marginal angle > 71.81° (mark 2), respectively. Likewise, in the case of using water similar results (mark 3 and mark 4) were obtained considering the effect of refractive index.

Another issue that must be addressed is that for LP, a discrepancy in FWHM exists under different immersion media. The faster spot size reduction in water is due to refractive index acting as a buffer to retard a considerable elongation effect caused by the longitudinal component as NA_{EFF} > 0.6. CP provides a good focus shape with no elongated aberration in a wide marginal angle from 0 to 71.8°. Although focused RP can generate the smallest focus spot, the required maximum marginal angle should be larger than 71.8°; also the design and cost of this type of lens are complex and expensive. Therefore, these features restrict the applicability of RP.

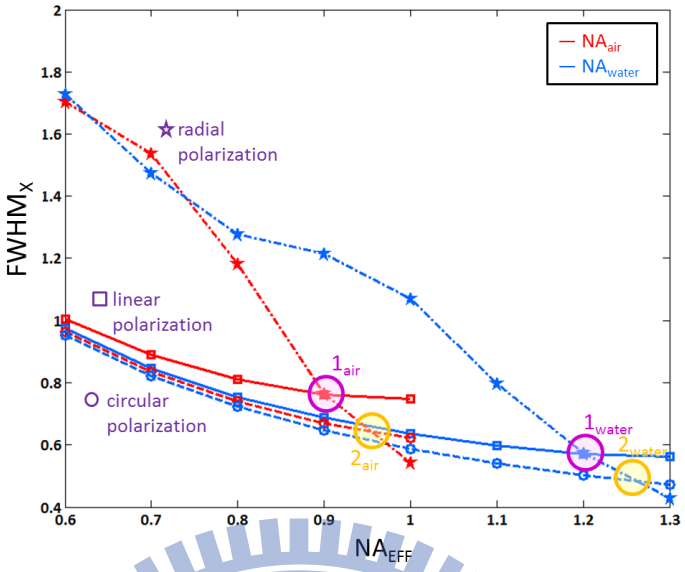

Fig. 3 5 Comparison of the $FWHM_x$ (measured along the x axis) versus NA_{EFF} for different illumination beam. The black and gray lines represent focused light in air (n=1.0) and water (n=1.33), respectively. The lines dressed with symbols represent different beams. (□: linear polarization, ○: circular polarization, ★: radial polarization).

In short, we examined the focusing mechanism of radially polarized beam associated with the immersion technology and compared the focus spot between linear and circular illuminations. According to our numerical analyses, the refractive index of the immersion medium only provides a proportional scale factor and does not involve enlarge event of the longitudinal component of RP. The degree of marginal angle is the key issue for RP to form a small focus spot. As the marginal angle of the objective exceeds 64.16 and 71.81°, the high L-T ratio of the RP enables the formation of a smaller spot than LP and CP, respectively. In an optical focusing system, CP is widely adopted, but RP provides a niche market in some applications.

Chapter IV

Application on

SPPs Excitation and Manipulation

Polarization is one important property of light. This vector nature of light and its interactions with matter make many optical devices and optical system designs possible. In the previous chapters, we have gone through the influence of field distribution at the focal plane, especially in the case of a high numerical aperture system, which is caused by the polarization distribution at the pupil plane. Also, the method to generate spatially inhomogeneous polarized beam was proposed which has a great freedom to add amplitude as well as phase modulation through the spatial light modulator. Based on the understanding on behavior of strongly focused SIP beams in homogeneous and isotropic media, in the following chapters, we are going to apply this polarization manipulation technique to interact with material which has pronounced behavior and response in associated with polarization.

In this thesis, we devoted gold as our material which can support the existence of surface plasmon resonance (SPR) by means of the interaction between polarization of light and geometry of metal. According to the geometry of metal, excited surface plasmon polaritons (SPPs) can be clasfied into two kinds: long-range propagating SPPs and localized SPPs. The former one is existed at a flat metal-dielectric interface by the in-plane polarized light (TM wave). A far-field polarization modulation method to excite SPPs is proposed and will be discussed in Chapter 4. Utilizing the property of SPR which is very sensitivity to the refractive index change of adjacent dielectric material, two kinds of SPR sensors will be delivered in Chapter 5.

In contrast, the localized surface plasmon is confirmed within the metallic shell of a nanoparticle. The nanorods with elongated shaped along longitudinal direction is a perfect polarization absorber which can generated two-photon excited fluorescent when the polarization of incident light is parallel to its longitudinal direction. Even, we can shorten its physical dimension by increasing the energy of pulse laser due to photothermal effect. Those great properties are useful for imaging as well as optical data storage which will be dressed in Chapter 6.

4.1 The Fundamental of Surface Plasmon Resonance

The discovery of SPPs is in 1902, R. W. Wood observed a unusual phenomenon that didn't fit the diffractive theorem of grating when the polarization of light with electric field upright to the groove of metal grating [59]. He attempted to explain the phenomenon by oscillation with specific polarization of light and metal grating structure. Until 1941, Fano purposed a new explanation about the strange phenomenon, he thought that a new electromagnetic wave would be produced and propagated along surface when the polarization of light with electric field upright to the groove of metal grating [60]. The electromagnetic wave is so-called SPPs afterward. Then in 1950, R. H. Ritchie and R. A. Ferrell *et al* purposed the theoretic model of SPPs sequentially [61, 62], From then on, SPPs elicited the interests of scientist, more attention invested in this study.

The SPPs are collective oscillations of free electrons that can propagate between the metal and dielectric surface. It is a kind of electromagnetic wave and confined within the sub-wavelength of metal surface. Exactly as above said, the SPPs are electromagnetic wave, therefore, we can find the condition of existence of SPPs from Maxwell's equation. In order to know the condition, we consider an interface between two media and look for a homogeneous solution of Maxwell's equations at the surface. The Maxwell's equation at the

surface between two media can be written as

$$\nabla \times \vec{H} = \varepsilon \frac{d\vec{E}}{dt} \tag{4.1a}$$

$$\nabla \times \vec{E} = -u \frac{d\vec{H}}{dt} \tag{4.1b}$$

$$\nabla \cdot \varepsilon \vec{E} = 0 \tag{4.1c}$$

$$\nabla \cdot \vec{H} = 0 \tag{4.1d}$$

Next considering s-polarization and p-polarization incident waves propagate between two media as shown in Fig. 4.1, for s-polarization incident wave, the wave function is

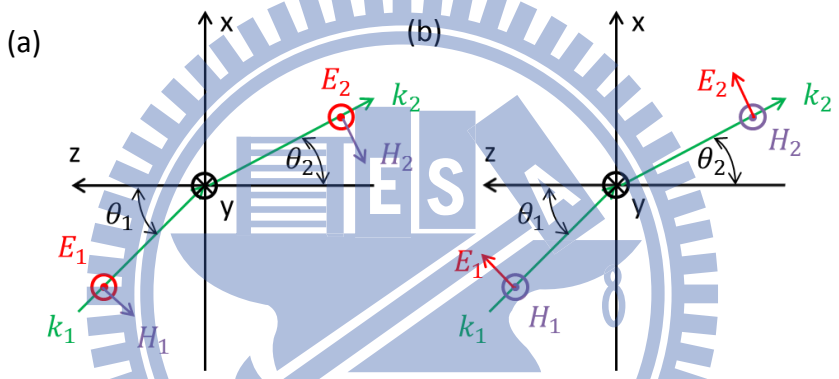

Fig. 4. 1 (a) s-polarization (b) p-polarization waves propagate between two media.

z>0

$$\vec{H}_1 = (H_{x1}, 0, H_{z1})\, exp(k_{x1}x + k_{z1}z - \omega t)i \tag{4.2a}$$

$$\vec{E}_1 = (0, E_{y1}, 0)\, exp(k_{x1}x + k_{z1}z - \omega t)i \tag{4.2b}$$

z<0

$$\vec{H}_2 = (H_{x2}, 0, H_{z2})\, exp(k_{x2}x - k_{z2}z - \omega t)i \tag{4.2c}$$

$$\vec{E}_2 = (0, E_{y2}, 0)\, exp(k_{x2}x - k_{z2}z - \omega t)i \tag{4.2d}$$

From Eq. (4.2a) to Eq. (4.2d), these equations must satisfy boundary condition, then electric fields and magnetic fields at the surface are of the form

$$E_{y1} = E_{y2} \tag{4.3a}$$

$$u_1 H_{z1} = u_2 H_{z2} \tag{4.3b}$$

$$H_{x1} = H_{x2} \tag{4.3c}$$

$$k_{x1} = k_{x2} \tag{4.3d}$$

Substituting Eq. (4.2a) to Eq. (4.2d) into Eq. (4.1b) leads to

$$k_{z1}E_{y1} = -u_1\omega H_{x1} \tag{4.4a}$$

$$-k_{z2}E_{y2} = -u_2\omega H_{x2} \tag{4.4b}$$

$$k_{x1}E_{y1} = -u_1\omega H_{z1} \tag{4.4c}$$

$$k_{x2}E_{y2} = -u_2\omega H_{z2} \tag{4.4d}$$

For nonmagnetic materials, $u_1 \approx u_2$, according as Eq. (4.3a) to Eq. (4.3d), we can obtain a result of wave-vector

$$k_{z1} = -k_{z2} \tag{4.5}$$

Comparing with dispersion relation

$$k_{x1}^2 + k_{z1}^2 = \varepsilon_1 \left(\frac{\omega}{c}\right)^2 \tag{4.6a}$$

$$k_{x2}^2 + k_{z2}^2 = \varepsilon_2 \left(\frac{\omega}{c}\right)^2 \tag{4.6b}$$

We can know that Eq. (4.5) is contradiction if $\varepsilon_1 \neq \varepsilon_2$ from Eq. (4.6). That because the s-polarization wave only has electron field along the surface, so there are no electron accumulation. Hence, the SPPs for s-polarization don't exist at the surface, in other words, the s-polarization incident wave cannot excite the SPPs

For p-polarization incident wave, the wave function is

z>0

$$\vec{H}_1 = \left(0, H_{y1}, 0\right) exp(k_{x1}x + k_{z1}z - \omega t)i \tag{4.7a}$$

$$\vec{E}_1 = (E_{x1}, 0, E_{z1})\, exp(k_{x1}x + k_{z1}z - \omega t)i \tag{4.7b}$$

z<0

$$\vec{H}_2 = \left(0, H_{y2}, 0\right) exp(k_{x2}x - k_{z2}z - \omega t)i \tag{4.7c}$$

$$\vec{E}_2 = (E_{x2}, 0, E_{z2})\, exp(k_{x2}x - k_{z2}z - \omega t)i \tag{4.7d}$$

From Eq. (4.7a) to Eq. (4.7d), these equations must satisfy boundary condition, and then

electric fields and magnetic fields at the surface are of the form

$$H_{y1} = H_{y2} \tag{4.8a}$$

$$E_{x1} = E_{x2} \tag{4.8b}$$

$$\varepsilon_1 E_{z1} = \varepsilon_2 E_{z2} \tag{4.8c}$$

$$k_{x1} = k_{x2} \tag{4.8d}$$

Due to the symmetric of propagating wave at the interface, $E_{z1} = -E_{z2}$, then relation of permittivity between two media is

$$\varepsilon_1 = -\varepsilon_2 \tag{4.9}$$

The significance of Eq. (4.9) indicated the SPPs only exist and are excited on metal which is negative index. Then Substituting Eq. (4.7a) to Eq. (4.7d) into Eq. (4.1a) leads to

$$k_{z1} H_{y1} = \varepsilon_1 \omega E_{x1} \tag{4.10a}$$

$$k_{x1} H_{y1} = -\varepsilon_1 \omega E_{z1} \tag{4.10b}$$

$$k_{z2} H_{y2} = -\varepsilon_2 \omega E_{x2} \tag{4.10c}$$

$$k_{x2} H_{y2} = \varepsilon_2 \omega E_{z2} \tag{4.10d}$$

$$\frac{k_{z1}}{\varepsilon_1} + \frac{k_{z2}}{\varepsilon_2} = 0 \tag{4.10e}$$

Finally, from Eq. (4.10e) and Eq. (4.8d) it leads to dispersion relation

$$k_{x1} = k_{spp}(\omega) = \frac{\omega}{c} \sqrt{\frac{\varepsilon_1(\omega)\varepsilon_2(\omega)}{\varepsilon_1(\omega)+\varepsilon_2(\omega)}} \tag{4.11a}$$

$$k_{zi} = \sqrt{\varepsilon_i k_0^2 - k_{x1}^2} \quad i = 1,2 \tag{4.11b}$$

In order to excite the SPPs, we require that k_{x1} is real and k_{zi} is purely imaginary in both media. Then permittivity of both media only can be

$$\varepsilon_1 + \varepsilon_2 < 0 \tag{4.12a}$$

$$\varepsilon_1 \cdot \varepsilon_2 < 0 \tag{4.12b}$$

The significance of Eq. (4.13) and Eq. (4.12) is similar to Eq. (4.9), which means that not only index of two media must be negative, but also the absolute value of negative index exceeding that of the other. Most of the materials, especially noble metals have large

negative real part of dielectric constant. Therefore, the SPPs can exist at the interface between a noble metal and a dielectric when the polarization of incident light is p-polarization.

4.1 Generate SPPs via Radial Polarization

Recently, there has been a surge of interest in the characteristics of electromagnetic modes supported by a variety of thin film structures, in both the fundamental and applied sciences. A great deal of attention has been devoted to surface plasmon polaritons (SPPs), which are confined to the metal-dielectric interface; exponentially decaying as they move away from the interface into the neighboring media. The excitation of SPPs in metallic films with complex permittivity $\varepsilon_m(\omega)=\varepsilon_m'(\omega)+i\varepsilon_m''(\omega)$ is determined by the law of dispersion that imposes a narrow set of resonant angular vectors at a given frequency of excitation [63, 64]. Because the relationship between the excitation and dispersion of SPPs is related to the characteristics of the adjacent dielectric material, a great number of SPP-based modulators and switches have been developed over the last few years [65-69]. Due to the unique behavior of SPPs in the near-field, researchers have recently shifted their attention to the focus and guidance of SPPs. In the journal NANO Letters of a 2005 study, Yin et al. reported a method for launching and focusing SPPs through a strip waveguide, utilizing subwavelength hole as a dipole source of SPPs [70]. In addition, Alberto et al. introduced phase delay into the arrangement of the array of holes, creating a so-called “near-field optical phase antenna” to refocus the source of the SPPs [71]. However, the design and implementation of surface-feature-mediated long-range plasmon were extremely delicate in the near-field, which unavoidably increased the difficulties in practical implementation.

Localized optical field engineering is complementary to near-field engineering, but

offers significant advantages in its approach to excitation, thanks to the wide spectrum of wave vectors it provides. Many studies utilize a high-numerical-aperture (NA) objective lens to tightly focus laser beams and precisely control the excitation of SPPs on a structureless metal surface [72, 73]. Based on the collinear Kretchmann setup, Q. Zhan focused radial polarization on a dielectric-metal interface. Owing to the fact that the entire beam was p-polarized (TM-polarized) with respect to the incidence plane of the multilayer structure, the subwavelength Bessel beam was subject to resonant conditions and could be regarded as an SPPs point source [73, 74]. In addition, modified radial polarization with a cogwheel-like light source, was also adapted to symmetrically focus SPPs [75]. According to previous studies, most of the generated SPPs were center-symmetric and identical to the focus field of the longitudinal component. Alternatives for the generation of asymmetrical SPPs and their properties have not been adequately reported or discussed; which has hindered advancement in the application of SPPs.

In this study, we have maintained our commitment to far-field schemes, in proposing a flexible new approach to launching SPPs, with versatile field distribution. This method is based on a collinear configuration, in conjunction with spatially inhomogeneous polarized (SIP) illumination [17, 21-23, 26, 43]. The structure of the polarization for the SIP beam at the pupil entrance fulfills a similar function to the array of holes used in near-field engineering. This enables a variety of SPPs, due to the three-dimensional characteristics of the optical field. To elaborate on the underlying physics and mechanisms, we produced a phenomenology model associated with the manipulation of SPPs on a flat metallic surface. In addition, we verified the proposed scheme through observation of experiments and finite-difference time-domain (FDTD) simulation.

4.2 Optical Configuration and Mechanism

We employed wide field SPR microscopy [73-76], illuminated by a specific state of polarization, as illustrated in Fig. 4.2 (a). The total internal reflection (TIR) objective with gold coated cover glass was used to replace the conventional prism coupler, as in a collinear Kretchmann setup. The cover glass was coated with 40 nm of Au (n = 0.203 + 3.105i at λ_0 = 632.8 nm). The gap between the objective (Olympus 60x NA = 1.45) and the cover glass was filled with oil, with a matching liquid refractive index. The light source was created to perform a specific state of polarization, a so-called SIP beam, as shown in Fig. 4.2(b). The SIP beam comprised two orthogonal components: radial and azimuthal polarizations. The spatial arrangement of the polarizing structure on the plane of the pupil was directly related, to the three-dimensional optical field in the focal region of the high-NA lens, by a simple real-valued geometry-dependent matrix [77].

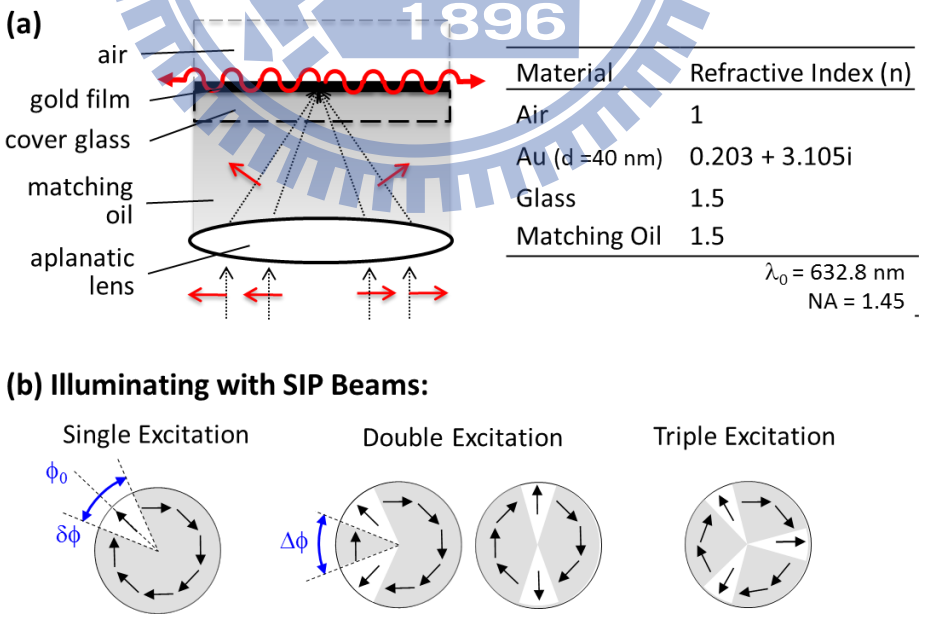

Fig. 4. 2 A schematic diagram of the optical setup for steering and shaping SPPs, utilizing spatially inhomogeneous polarized (SIP) illumination. The table [right side of Fig. 1(a)] shows the parameters of the proposed optical setup with a working wavelength of λ_0 = 632.8 nm.

The SIP beams were grouped into three schemes [Fig. 1(b)]: single, double and triple excitation, respectively. Three parameters were adjusted to identify the character of the features of SIP beams; where $\delta\phi$ represents the size of the TM-polarized sector at the pupil entrance, ϕ_0 is the center of angular arc of TM-polarized sector, and $\Delta\phi$ represents the angular distance between two TM-polarized sectors.

As longitudinal electric oscillation waves, the SPPs followed only the direction of the electric field induced by the radially polarized focus. In contrast, the azimuthal polarization imposed none of the resonant in-plane angular vectors, with no excitation of SPPs. The ability to alter the properties and subsequent polarization arrangement at the entrance pupil offered a simple but effective SPP launching scheme, with respect to individual incident planes. The polarization distribution at the entrance pupil was characterized by three parameters: $\delta\phi$, ϕ_0 and $\Delta\phi$, as shown in Fig. 4.2(b). $\delta\phi$ is the size of the TM-polarized sector at the entrance pupil. ϕ_0 is the center of angular arc of TM-polarized sector determining the direction guiding the launched plasmonic wave. $\Delta\Phi$ represents the angular distance between two TM-polarized sectors.

In the past, the study of field-distribution of focus excited SPPs was well developed through the use of vectorial Debye integral of Richards and Wolf, in conjunction with Fresnel transmission coefficients of a dielectric/metal/air structure [52, 57, 78-80]. Several researchers adapted this method of calculation to study the behavior of SPPs, under various degrees of illumination [73, 81-85]. The state of polarization at the pupil entrance determined the field distribution at the focal point, which could be calculated by means of vectorial calculation. When angular contribution was restricted to a narrow band, the field distribution of the SPPs was proportional to the longitudinal component of the focus. Integral equations with embedded Fresnel transmission coefficients could be used to

describe the excitation of the SPPs. However, the quantitative description and analytical solution mentioned above are valid only for symmetrically focus excited SPPs. Under the conditions of our method, when illumination is an SIP beam, rather than conventional polarization, the result of the excited SPPs indicates more than simple constructive or destructive interference. This discussion would be incomplete without considering the propagational behavior of plasmonic waves when the structured illumination contained attributes of asymmetrically-distributed polarization. For example, in the case of a single excitation, the field distribution of SPPs would show a discrepancy between the results of the experiment and the outcome of the vectorial Debye integral. This is because conventional models are unable to describe the coma-shaped field distribution of SPPs, in which their propagating nature is revealed. We have improved on previous versions and propose a new phenomenological model associated with a semi-quantitative description, to illustrate the mechanism of SPP generation and its underlying physics. A schematic diagram is illustrated in Fig. 4.3.

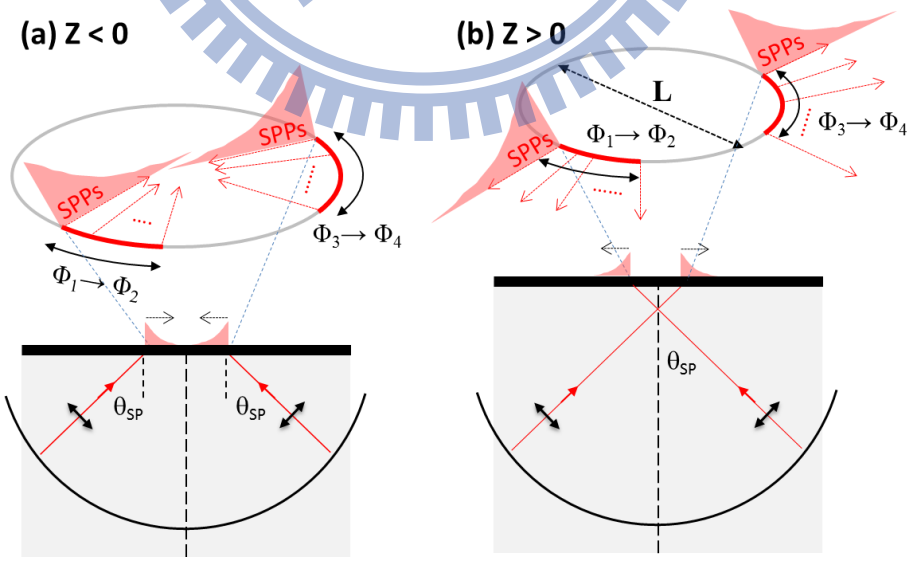

Fig. 4. 3 A schematic diagram of the mechanism used to generate surface plasmon waves originating from a virtual annular ring via spatially inhomogeneous

polarized beams. The virtual annular ring is the cross section between the light cone and the observation plane, and it consists of red and gray arcs which indicate the positions of TM- or TE-polarized rays impinged, respectively.

From the viewpoint of geometric projection, we treated SIP beam as a group of rays propagating along its Poynting vector toward the vicinity of focus due to the guidance of the lens. Each ray carried either TM- or TE-polarization depending on its emitting position at entrance pupil, and only TM-polarized ray could effectively excited SPPs. Because of phase matching condition, contributed rays were restricted to a light cone with a narrow bandwidth. The cross section between the light cone and the observation plane pointed out a virtual annular ring. This virtual annular ring was the connection of each exciting positions of SPPs and its diameter was highly relevant to the position of focus. In other word, the polarization structure of the SIP beam at the pupil entrance determined the pattern of SPP excited position which fulfilled a similar function to the array of holes used in near-field engineering.

In this paper, we have presented an alternative to bringing partial in-plane wave vectors to create specific conditions for the excitation of SPPs located on the virtual annular ring, by switching the state of polarization between TM and TE modes. The characteristic of virtual annular ring fulfills a similar function to the array of holes used in near-field engineering. As shown in the Fig. 4.3, the gray circle with diameter L represents the virtual annular ring. The red arcs indicate the active regions where the SPPs are launched; also they are the projection of TM-polarized sectors of SIP beam at the entrance pupil.

As the metallic film was below the focus [Fig. 4.3(a), $Z < 0$], the plasmon waves counter propagated toward the center to interfere mutually. As the metallic film is above the focus [Fig. 4.3(b), $Z > 0$], the plasmon waves propagated away from the center, effectively casting multiple plasmonic waves. Under these conditions, no interference occurred within the

virtual annular ring. The overall behavior of launched SPPs could be described as a summation of individual plasmon waves resembling a secondary source originating from the virtual annular ring, as shown in Eq. (4.13).

$$\mathrm{E}_{total}(r,\phi) = \int_{\Phi_1}^{\Phi_2} \frac{dE_{SP}(\phi)}{d\phi} d\phi + \int_{\Phi_3}^{\Phi_4} \frac{dE_{SP}(\phi)}{d\phi} d\phi + \cdots \quad (4.13)$$

and

$$\mathrm{E}_{SP}(r,\phi) = E_0(r,\phi) e^{-\alpha d(r,\phi)} e^{i\beta d(r,\phi)} \quad (4.14)$$

$$\mathrm{d}(r,\phi) = L - r\cos(\phi - \phi_0) \quad (4.15)$$

where r and ϕ refer to the polar coordinates of the point of observation. The total field distribution was a superposition of individually launched plasmons propagating toward/away the center, where the upper and lower limits of each integral indicated the boundary of the launched SPPs, defined by the TM-polarized sectors. Individual plasmon waves are described as planar waves (Eq. 4.14) with the attenuation term α and propagating constant β given by real and imaginary parts of $k_{SP} = k_0 [\varepsilon_d \varepsilon_m / (\varepsilon_d + \varepsilon_m)]^{1/2}$, where L is the radius of the virtual annular ring and ϕ_0 is the original point of the plasmon wave. The development of this equation was an extension of the interference model of two counter-propagating surface plasmon waves in the Kretchmann configuration [86]. Compared to FDTD method, this model did not provide an analytical solution to the formation of SPPs. Nevertheless, the discussion provided guidance for a qualitatively study of the field distribution of SPPs, when propagation behavior and interference were simultaneously affecting the results. In addition, the proposed phenomenological model provided a quick method to initiate a new design for SIP beams.

4.4 Simulation Results

To calculate the formation of SPPs, we imported the field distribution of focus,

generated by vectorial diffraction theory, into commercial FDTD software, SIM 3D_MAX, by MMResearch. The two-dimensional field distributions of |Ez| component are identical to the field distribution of excited SPPs. Figure 4.4 illustrates the field distribution of excited SPPs for single excitation. To improve the visualization of the outer ring, the results were selected to illustrate the amplitude of its field distribution rather than intensity. With a single excitation, we modulated the size and position of a single TM-polarized sector to observe the corresponding SPPs fields. As shown in Fig. 4.4(a) and (b), the center of the angle of TM-polarized sector, ϕ_0, determined the direction of propagation of the plasmonic waves. The size of the TM-polarized sector, $\delta\phi$, corresponded reciprocally to the excited area. Such plasmonic manipulations show potential as a new scheme, for achieving high throughput and coupling efficiency for the planar plasmonic waveguides or devices.

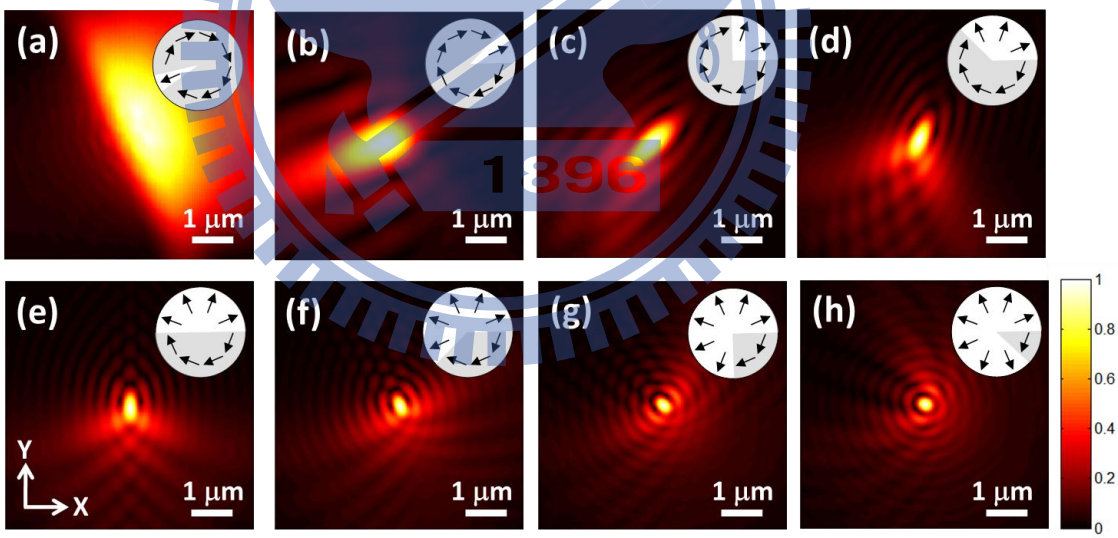

Fig. 4. 4 The calculated field distribution of SPPs when the SIP beam was focused on the Au/Air interface. Subfigures (a) to (h) display single excitations with different ratios of TM-polarization (indicated with black arrows along the radial direction, indicated by the white background) at the pupil entrance, where (a) $\phi_0 = 202.5^\circ$ and $\delta\phi = 22.5^\circ$, (b) $\phi_0 = 22.5^\circ$ and $\delta\phi = 45^\circ$, (c) $\phi_0 = 90^\circ$ and $\delta\phi = 45^\circ$, (d) $\phi_0 = 67.5^\circ$ and $\delta\phi = 135^\circ$, (e) $\phi_0 = 90^\circ$ and $\delta\phi = 180^\circ$, (f) $\phi_0 = 112.5^\circ$ and $\delta\phi = 225^\circ$, (g) $\phi_0 = 135^\circ$

and $\delta\phi = 270^{\circ}$, (h) ϕ_0 = 157.5° and $\delta\phi = 315^{\circ}$.

The field distribution of excited surface plasmon waves along the radial direction was expressed as $E_{SP} \sim E_0 \exp(ik_{sp}r)\exp(-L_{SP}/r)$, where L_{SP} was the propagation length with 1/e attenuation of the SPPs amplitude and r represented the radial propagation distance from the position of excitation. The propagation constant and length of SPPs were calculated by taking the real part on the field distribution of |Ez|. In the case of ϕ_0 = 22.5° and $\delta\phi = 45^{\circ}$ [Fig. 4.4(b)], the numerical result of the length of propagation and resonant wavelength were L_{SP} = 0.98 um and λ_{SPP} = 601nm, respectively. The numerical results agreed closely with the theoretical prediction under $\lambda_{SPP} = 2\pi/\mathrm{Re}[k_0(\varepsilon_1\varepsilon_2/\varepsilon_1+\varepsilon_2)^{1/2}]$ = 598 nm, whereas the theoretical length of propagation (6.24 um) was longer than that of the numerical results. This was because the field distribution of SPPs was formed by constructive interference induced from partially in-phase angular vector k_{sp}. This intensity peak was much higher than that of any ray excited surface plasmon wave.

When the size of the TM-polarized sector $\delta\phi$ was increased from 90^{o} to 315^{o}, the field distribution of excited SPPs revealed a gradual tendency toward local concentration, as shown in Figs. 4.4(c) to (h). In addition to the concentration of energy, the propagating SPPs were steered counterclockwise as $\delta\phi$ increased. At the same time, a series of interference ripples along the azimuthal plane became noticeable, yielding side lobes in the shape of discontinued arcs, due to the consequences of omni-directional SPPs propagation. As TM-polarized light occupied the entire pupil of illumination, the Bessel field distribution became excited creating a tiny spot at the center dressing the side lobe with a concentric ring. This was consistent with results in previous studies [73, 74].

Figure 4.5 shows two animations of SPPs with different formations generated by the double excitation scheme. The polarization distribution of the SIP beam was designed to aid

in the investigation of the interference behavior of the two propagated surface plasmons. In Fig. 4.5(a), the TM-polarized sector was divided into two equal parts where $\delta\phi = 45^{o}$ and varied in $\Delta\phi$. The inserted TE-polarized sector acted as a barrier to isolate two generated plasmon waves with an angular distance $\Delta\phi$. As $\Delta\phi$ changed from 15 to 135 degree, the interferometric patterns of the two oblique plasmonic waves gained additional outer edges with corresponding sway. The angular distance between the two edges was identical to $\Delta\phi$. In addition, a constructive bright spot was observed at the center, which had been created by in-phase counter-propagating vectors, but was irrelevant to the change of angular distance.

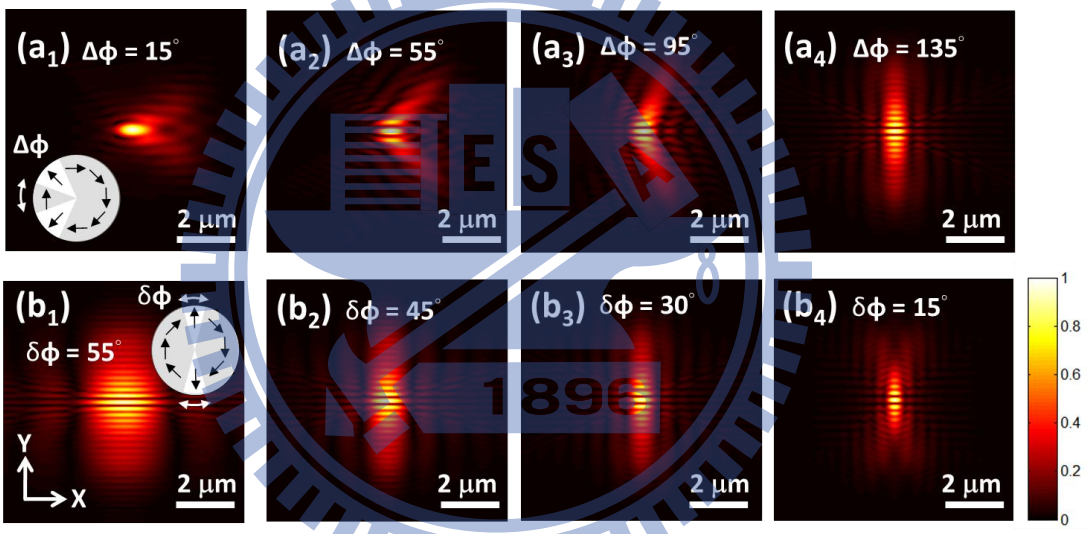

Fig. 4. 5 Double excited SPPs generated by purposely designed SIP beams, with the point of observation lying on the plane of focus. (a) the TM-polarized sector is divided into two part with equal $\delta\phi$ but varied in $\Delta\phi$. As $\Delta\phi$ changed from 15° to 135°, the interferometric patterns of two oblique plasmonic waves show additional outer swayed edges. (b) the polarization distribution of SIP beam consists of double TM-polarized sectors which was arranged on the opposite side with variations in the size of $\delta\phi$. A clear plasmonic interference pattern spreading along vertical direction can be observed due to the counterpropagation of the SPPs.

Figure 4.5(b) (right side) depicts the normalized field distribution of SPPs observed on the focal plane illuminated by an SIP beam featuring two counter TM-polarized sectors with varied $\delta\phi$. A clear plasmonic interference pattern extending vertically was observed, due to the counter-propagation of the SPPs. The modulation of the interference pattern implied a recipitical relation between the size of sector and the lateral elongation of the interference lines. When the size of the sector $\delta\phi$ shrank to a narrow slit on each side, the interference pattern of SPPs resembled that of two counter-propagating plane waves. This approach provided an easy, but effective way for scientists to investigate the interference of SPPs without the need for complicated nano-structures in the near-field.

Figure 4.6 shows additional methods for the manipulation of the SPPs, via scanning the observation plane through the geometrical focus. As mentioned before, the cross-sectional points between every TM-polarized ray and dielectric/metal interface comprised a virtual annular ring referring to the initiation points of the SPPs. When metallic film was placed below ($Z < 0$) or over the focus ($Z > 0$), excited plasmonic waves propagated either toward the center or away from the virtual annular ring, yielding obvious or obscure individual interference patterns. One point of note was that the excitation position of SPPs shifted with additional extension or reduction, depending on the axial position of the focus, as shown in Fig. 4.6(a). This behavior was consistent with predictions from proposed phenomenological model. The radius of the virtual annular ring (the parameter of L in Eq. 4.3) was largely dependent on defocus.

As we split the TM-polarized sector into three sections and scanned the metallic film through the focus, several unusual patterns were observed. These had been created either by interference between counter-propagating plasmons at the center, or three independent propagating SPPs, as shown in Fig. 5(b). It is vital to note that the resulting interference patterns for such triple excitations was a group of 150-nm-radius (in magnitude of 1/e decay) bright spots in a 300-nm-period hexagonal arrangement caused by many in-phase SPPs. The

separation distance and spot radii followed the basic concept of interference in which the period and the size are close to half the effective wavelength of SPPs. The spatial distribution of subwavelength spots could be manipulated by varying the size of individual TM-polarized sectors and the angular distance between each sector. On the other hand, when the focus moved above the interface, three propagated SPPs were simultaneously launched. This yielded a field distribution in the shape of a shamrock. Such multiple excitations could be applied to future's applications in planner optics.

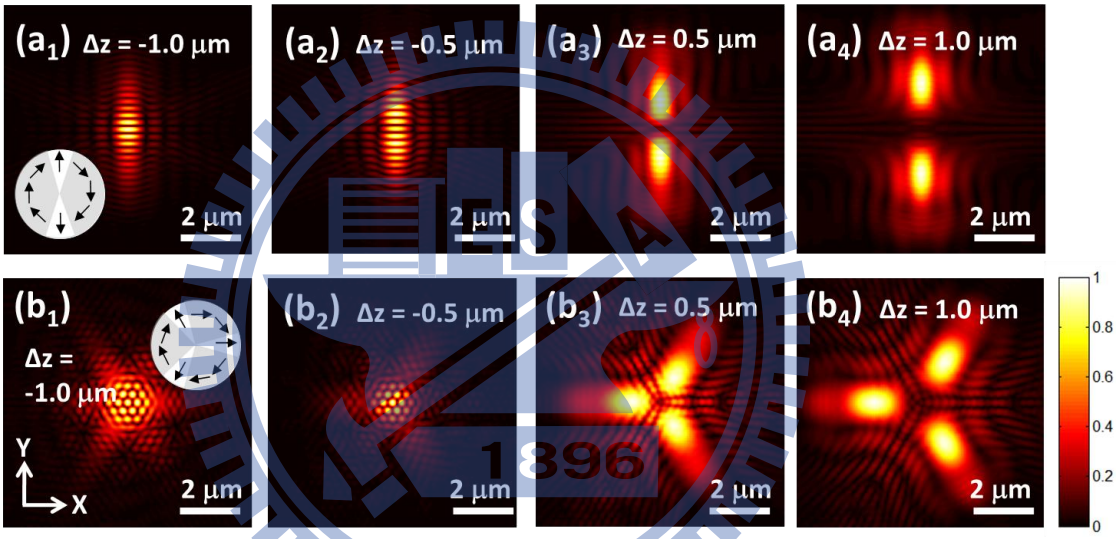

Fig. 4. 6 Dual excited SPPs, generated by purposely designed SIP beams with the observation plane scanning through the focus. (a) and (b) shows the field distribution of SPPs under specific SIP illuminating with dual and triple TM-polarized sectors (with equal $\delta\phi = 45°$), respectively.

4.5 Direct Measurement of Excited SPPs

In order to verify our far-field scheme, we conducted scanning near-field optical microscopy (SNOM) to image the field distribution of excited SPPs. Figure 4.7 shows the field

distributions of excited SPPs imaged by SNOM, where (a): single excitation, $\delta\phi$ = 45°, on focus, (b) single excitation, $\delta\phi$ = 15°, on focus, (c) double excitation, $\delta\phi$ = 45°, $\Delta\phi$ = 45°, on focus, and (d) double excitation, $\delta\phi$ = 45°, $\Delta\phi$ = 45°, defocus Z > 0, respectively. The insets depict the calculated SPP field distributions via FDTD calculation. In the case of a single excitation on the focus [Fig. 4.7(a) and (b)], the arc center of TM-polarized sector, ϕ0, dominates the propagating direction of excited SPPs. The spread area of excited SPPs is directly governed by the occupied ratio of TM-polarized sector which exhibits a reciprocal dependence between each other. Figure 4.7(c) and (d) show the function of defocus subject to a double excitation scheme. As two TM portions were kept in phase and focused, two groups of plasmonic

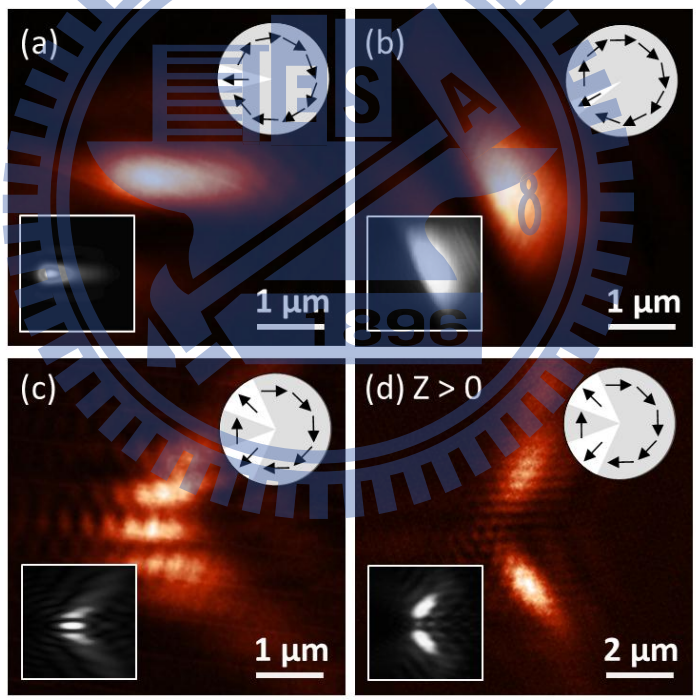

Fig. 4. 7 SPP field distributions imaged by SNOM under different excitation scheme: (a) single excitation, $\delta\phi$ = 45°, on focus, (b) single excitation, $\delta\phi$ = 15°, on focus, (c) double excitation, $\delta\phi$ = 45°, $\Delta\phi$ = 45°, on focus, and (d) double excitation, $\delta\phi$ = 45°, $\Delta\phi$ = 45°, defocus Z > 0, where insets represent FDTD maps.

waves not only lead to a constructive interference at the center, but also form an additional

pair of outer edges. The angular interval of those outer edges is controlled by the size of the sandwiched TE-polarized sector. When the observation plane moves above the focus (Z > 0), the field distribution of double-excited SPPs goes back to propagating mode. Entire excited SPPs would propagate away from the center and no interference pattern would be observed. Furthermore, the results of double excitation is similar to the work done by L. Novotny, where he used a tightly focused beam to depolarize a linear polarization and thus form a two-lobe pattern [81].

Besides the manipulation of SPP patterns, the proposed scheme enables scientists to create interference patterns with a wide range of line width and period. Figure 4.8 shows the field distribution of excited SPPs created by a double excitation scheme with different ratios of the opposite TM sector along the x-axis. The measured period (Λr-SPP) of SPP interfering fringes along the x-axis increased from Λr-SPP = 275 nm to 316 nm as we increased the TM ratio from $\delta\phi$ = 15° to 75°. The experimental results closely agree with FDTD results, Λr-SPP = 273 nm at $\delta\phi$ = 15° and 312 nm at $\delta\phi$ = 75°. It is noted that the period of the interference pattern extends horizontally. This is because the spatial period of interference is given by Λr-SPP2 = Λx-SPP2 + Λy-SPP2, where obliquely propagating SPPs provide an additional ky wavevector in horizontal direction. Once a TM-polarized sector occupies the entire entrance pupil, the profile of excited SPPs will identical to a radial-polarization-generated Airy disk [23, 73, 74]. These properties ensure the modulation of the TM/TE ratio not only control the envelope of the SPP localization but also the fringe pattern.

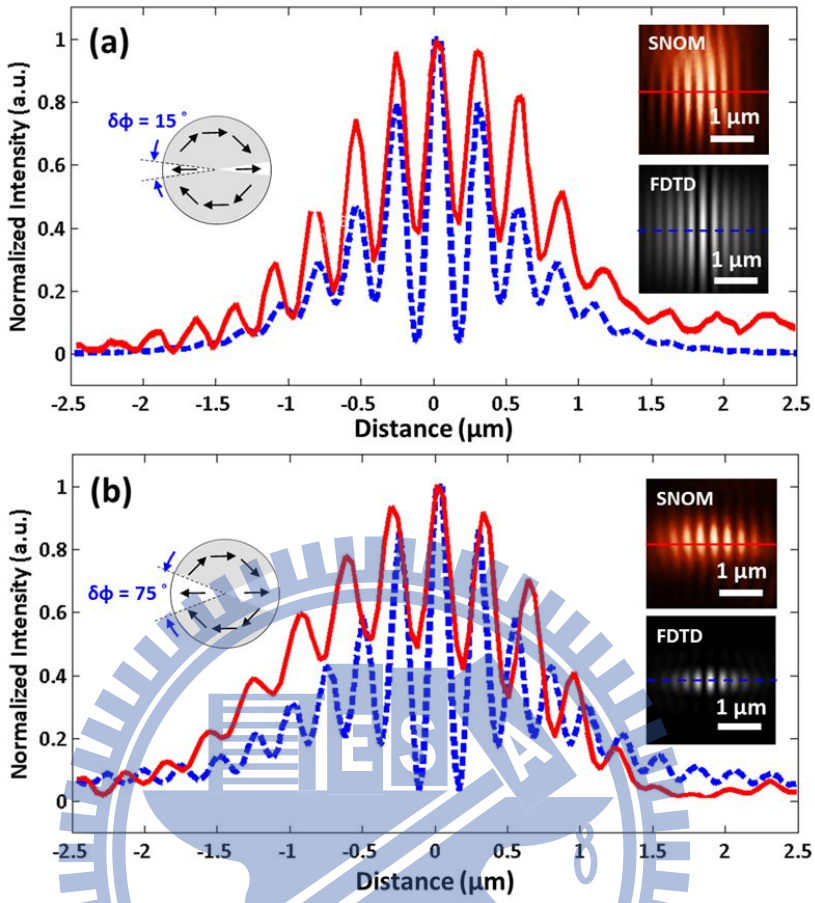

Fig. 4. 8 Cross-sectional cut of interference in the case of double excitation scheme with different ratios of the opposite TM sector along the x-axis (a) $\delta\phi$ = 15° and (b) $\delta\phi$ = 75°, where the period of fringe pattern is increased due to more oblique component of k_y wavevector in the case of $\delta\phi$ = 75°.

Based on the arrangement of the split polarization and the focus position, we demonstrated a number of unique patterns by using the far-field approach. Finally, we design the polarization distribution of entrance pupil into three-fold TM-polarized sector with equal arc distance $\delta\phi$ = 45°. In addition, we record the images of excited SPPs while the observation plane scans through the focus. The excited SPPs were formed either by interference between counter-propagating plasmons, or three independent propagating SPPs, as shown in Fig. 4.9. At Z < 0, three bands of in-phase plasmon waves propagated

toward the center and yielded a 150-nm-radius dots array profiled by a 300-nm-period hexagonal shape. The dot sizes and separation distances were governed by the standing plasmonic wave, the results were close to the half SPP effective wavelength (λ_{SPP} = $2\pi/\mathrm{Re}[k0(\varepsilon 1\varepsilon 2/\varepsilon 1+\varepsilon 2)1/2]$ = 598 nm). The separation distance between subwavelength holes can be manipulated by tuning the ratio of TM/TE polarized sectors. Compared with the strong steering by a converging beam, at Z > 0, three bands of unmodulated plasmonic waves would lead to three plasmonic fans propagating outward. In combination with the split engineering, other asymmetric SPP patterns can be achieved by introducing designated phase modulation at the entrance pupil.

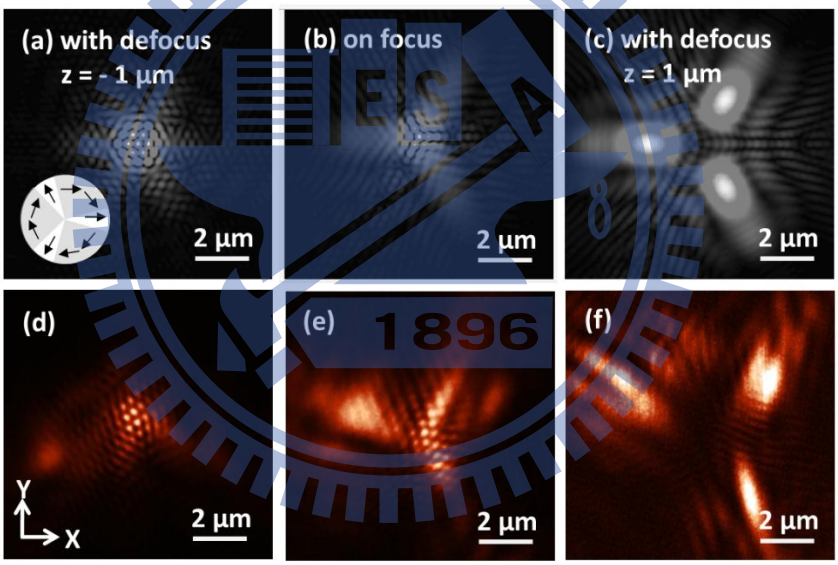

Fig. 4. 9 Intensity distribution of SPPs under triple excitation scheme when the observation plane scanned through the focus with (a) defocus Z = -1 um, (b) on focus and (c) defocus Z = 1 um. (d), (e) and (f) represent the corresponding FDTD results.

4.5 Short Conclusion

In conclusion, we proposed a far-field scheme for the generation of asymmetric SPPs. The excitation mechanism is based on the spatial arrangement of split polarization at entrance pupil in conjunction with a defocus technique. It provides a similar function to the near-field approach, which utilizes the subwavelength features in order to generate SPP dipoles. Also, it provides an irreplaceable flexibility to real-time manipulate SPPs into desired distribution by integrating a spatial light modulator into this scheme. Proposed method will certainly has a promising impact on carrying out various SPP excitations for lithographic applications, plasmonic waveguides, and biophotonic devices due to its simplicity and versatility.

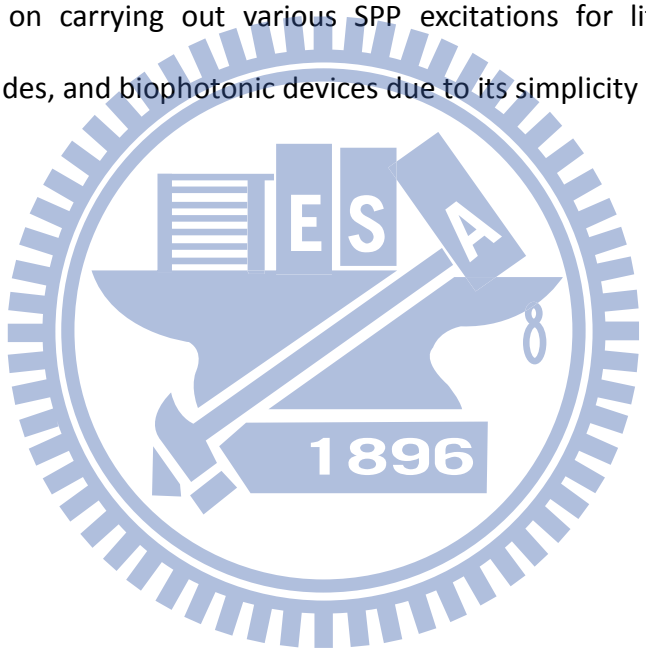

Chapter V

Application on

Objective-based SPR sensors

In the previous chapter, we discuss the application on applying SIP beam to excite surface plasmon polaritons (SPPs) which occurs at the metal/dielectric interface based on the energy coupling of the transmitted evanescent wave. In the meantime, rest of the uncoupled light will reflect to the back focal plane of the objective lens. By collecting all of the reflected light, a reflected disk having a dark resonance ring at particular angular position will be shown which is refer to resonance of surface plasmon. By observing the radius change or deformation of the dark resonance ring, we can built a sensor with high sensitivity which is used to detect tiny deviation came from a sample in terms of the change of effective refractive index and its shape. In Chapter 5.1, a brief introduction of surface plasmon (SPR) sensor and its corresponding literatures review will be given. Following current tendency of development on SPR sensor, we proposed two radial polarization enabling SPR sensors to meliorate the capability of current SPR sensor. One is interfering SPR sensor based on coherent radially polarized light, and the other is polychromatic SPR sensor based on incoherent light. The overall view of those two radial polarization enabling SPR sensors including concept, simulation results, and experimental results will be delivered in the chapter 5.2 and Chapter 5.3, respectively.

5.1 Introduction to SPR sensor

Surface plasmon resonance (SPR) sensors have been widely used to analyze the optical characteristics of material due to its highly axial resolution and angular/spectral sensitivity via strong confinement of SPPs at metal-dielectric interface. As the in-plane wavevector of an incident wave matches the resonant condition at the metal-dielectric interface, the surface plasmon would be excited accordingly [67, 87, 88]. SPs are generally excited by the attenuated total internal reflection (ATIR) configuration, which was firstly proposed by Otto and Kretschmann in 1960s by means of a prism coupler [89, 90]. Figure 5.1 shows the schematic diagram of a Kretchmann configuration. The interface of bottom golden monolayer and dielectric media support the existence of surface plasmon polaritons mode which can be excited by coupling a light came from a high refraction index media with high incidence angle. One can observe the evidence of energy coupling through the intensity change on reflected light. Normally, the sudden dip would be observed at the incident angle just slightly larger than total internal reflection (TIR) angle due to the phase matching condition.

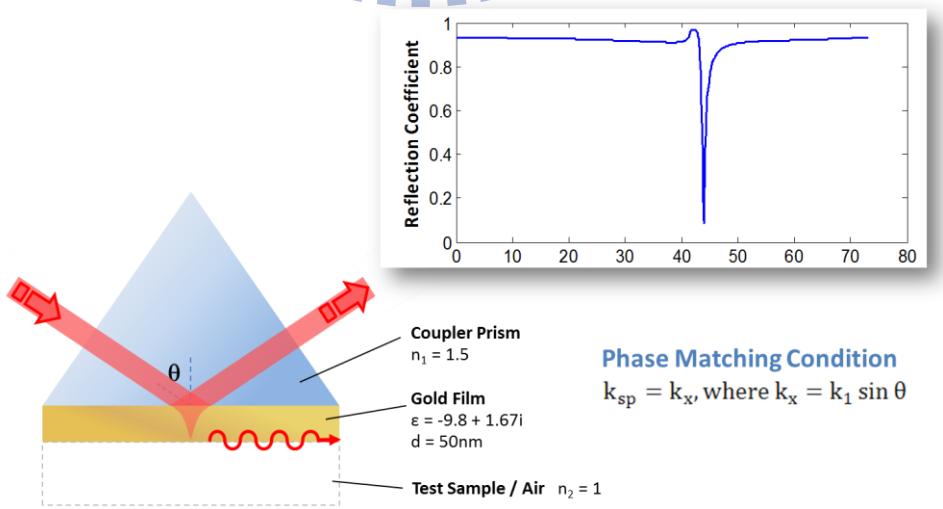

Fig. 5. 1 the schematic diagram of a Kretschmann configuration for the generation

of SPP and its corresponding reflectance versus incident angle.

Recently, H. Kano *et al* replaced a prism coupler with a collinear objective lens to create a universal angular wave vectors without the need for angular scanning [82, 91]. As a result, we are able to determine the resonance condition in a scan-free operation by observing the diameter change of resonance ring at the exit pupil. Based on the collinear setup, Zhan took advantages of radially polarized (RP) illumination to improve the conversion efficiency and spatial resolution [73, 74]. Impressive two-dimensional refractive index images of a bio-sample with fine details and high contrast have been obtained, but mostly by a monochromatic source [50, 51, 76, 92, 93].

5.2 Interfering SPR Sensor via Coherent Light

The ideas of utilizing radial polarization in conjunction with surface plasmon microscopy as a sensing setup is not new and have already demonstrated to image a cellular topography of refractive index map through scanning procedure. However, previous researches only focused on getting two-dimensional refractive index image which is generated by single wavelength excitation. It evidences the extreme sensitive and accuracy of the SPR again [94], but this property is innate and well know. What those studies have not mentioned yet is a unique feature come with the setup of radial polarization enabling surface plasmon microscopy. This unique feature is that the SPPs excited by a focused radial polarization is able to propagate along omni-direction cover entire metal surface. In this section, we demonstrate an experiment to reveal this unique feature by performing focused spot to scan across the edge of a water droplet. Then, the interaction between focused beam and sharp edge will be transported to far field shown on the back pupil plane of objective lens. The phenomenon of this feature is a corresponding relation between the deformation of dark-resonance-ring on reflect beam and position of index edge related to the center of plasmon focus. The results of FDTD simulation are given to show a good

agreement with that of experimental results. In addition, we also adopt a phenomenology model to describe the complex appearance of plasmon interference in the vicinity of index edge [95-99]. Finally, a novel sensing concept called “Near-field Sensing Radar” is proposed to elaborate the function of unique feature and push the capability of surface plasmon microscopy forward.

An oil immersion objective in conjunction with gold coated cover glass is arranged as collinear kretchmann configuration. Figure 5.2 shows its optical model with high numerical objective lens and test sample adhered to the substrate. A cover glass with refractive index of n_g = 1.5 is coated with 40 nm of gold (ε= -9.6 + 1.26i at λ_0= 632.8 nm). A water droplet placed on the metal layer was served as a refraction index step. We introduced a separation between the focused spot and the edge of the water/air boundary. The gap between total internal reflection fluorescence (TIRF) microscope objective (Olympus 60x NA 1.45) and the cover glass was filled with liquid refractive index matching oil. This immersion objective lens provides a large range of angular modulation with 75.16° which exceeds the required angular momentum for supporting a surface plasmon wave in the gold/air interface. With the radially polarized illumination, immersion

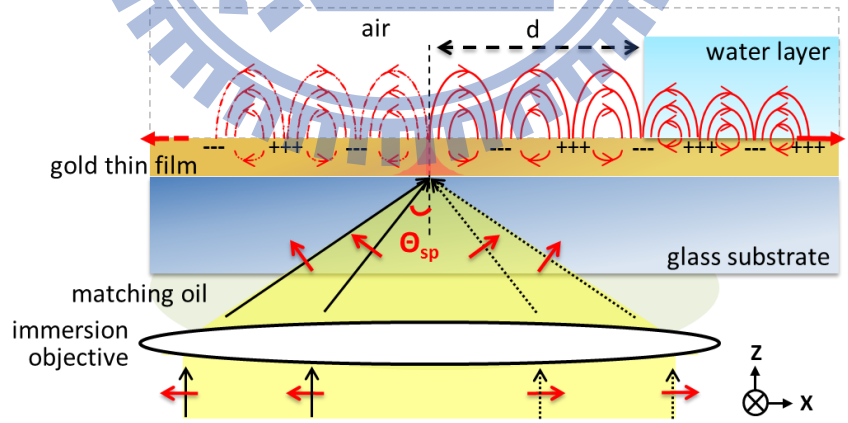

Fig. 5. 2 The optical configuration of collinear kretchmann with radially polarized illumination. The water layer creates a refraction index step having a separation distance between focused spot and boundary.

objective lens acted as a coupler which mimics the function of prism in traditional Kretchmann configuration with additional function of rotational symmetry. Consequently, an omni-direction propagating surface plasmon wave was generated among the metal surface and its self constructive interference forms a virtual probe with Bessel-shaped field distribution [73, 74].

The experimental setup shows in Fig. 5.3. It was based on an inverted microscope with a continuous wave (CW) He-Ne laser with wavelength of 632.8 nm. Linearly polarized beam converted to radial polarization through a consumer component of radial converter (RC). Its radiance illuminated the pupil of immersion objective lens through a pair of relay lens. With fine control of the focus, all of the light reflected from the metal surface was recollected via the same objective lens. Then, the Fourier spectrum of reflect light at back focal plane was projected onto the CCD camera by an imaging lens. The inset of Fig. 5.3(a) shows schematic patterns of the reflected beam captured on the CCD camera when the metal is exposed to air. The inner dark ring indicates the excitation angle of SP resonance ($\theta_{SPR,\ air}$ = 45°). Owing to the finite angular spectrum of immersion objective lens, it is unable to provide higher angular momentum ($\theta_{SPR,\ water}$ = 77°) to launch surface plasmon wave at gold/water interface which is beyond the maximum incidence angle of the lens. Therefore, the expecting dark-resonance-ring at Fourier plane is represented by a dashed contour which lies out of the pupil and is referred to $\theta_{SPR,\ water}$, as shown in Fig. 5.3(b).

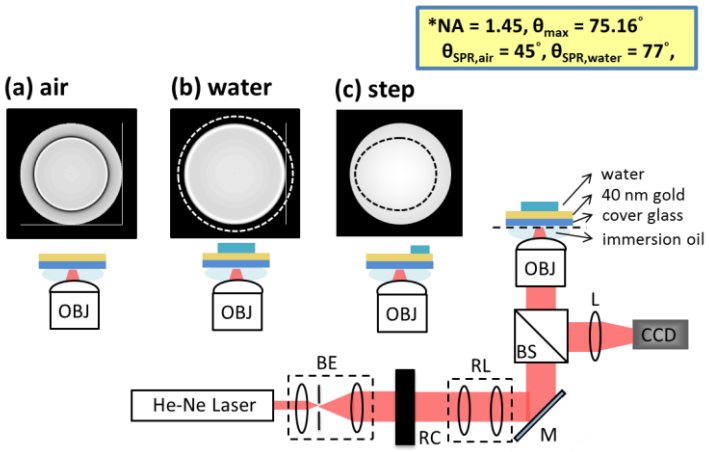

Fig. 5. 3 The setup of experiment is based on an inverter microscopy. Optical elements include a beam expender (BE), radial converter (RC), relay lens (RL), mirror (M), beam splitter (BS), objective with high numerical aperture (OBJ) and an imaging lens (L). Subfigure (a) to (c) respectively depicts the appearance of dark-resonance-ring corresponding to related position between water layer and the center of the focus.

Comparing to traditional SPR sensor, objective-based SPR sensor extends the active sensing region from one dimensional to two dimensional. The reflect beam is assembled by a bench of reflectance curves with respect to different azimuthal angle. Every individual reflectance curve is independently to each other and only responsible for individual refractive index change along azimuthal direction. The reflected disk shows position dependent 2D information rather than the averaged reflectance from a single focus. As a result, the appearances of the dark-resonance-ring at reflect beam would be deformed depending on the geometric layout of test object with respect to azimuthal angle. Hence, we propose a conceptual assumption that the pattern of dark-resonance-ring would be replaced by an asymmetry one while the distribution of refractive index under focused spot is inhomogeneous. In that condition, the appearance of dark-resonance-ring shall be perform as the black-dashed line in Fig. 5.3(c).

5.2.1 Simulation and Experimental Results

Generally, the application of multiple reflection calculation based on Fresnel reflection theory is straightforward and gives accurate results. In this work we are going to investigate the propagation phenomena of focused surface plasmon in associated with the present of index step. Far from this index step Fresnel theory still applies, but at the distance smaller than the propagation length of SPs it cannot be used. Because Fresnel theory assumes that

the multilayer structure consists of layers without lateral structure, it can only provide the reflectance far from the step as a boundary condition. Therefore, the finite-difference time-domain (FDTD) method is utilized to simulate the complex behavior of electro-magnetic wave along the metal surface caused by the step-distributed refractive index of specimen. Following, the electric field presented on the metal surface was mapped to far-field through the propagation calculation based on vectorial theory of diffraction. Consequently, a typical pattern of reflect beam with dark-resonance-ring can be observed at the exit pupil of immersion objective lens. Figure 5.4 shows the simulation and experiment results of the reflect beam captured on the CCD camera when different separation distance is introduced between focused radially polarized beam and the air/water boundary. The simulation results show a good agreement with experimental results and both of them give strong support on our conceptual assumption that the deformation of the dark-resonance-ring at the exit pupil is azimuthal direction dependent.

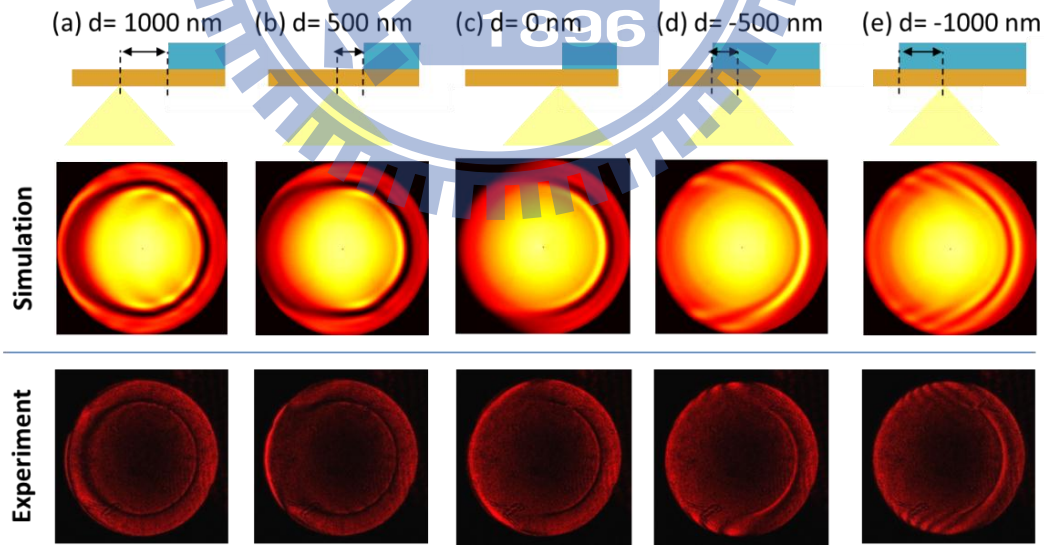

Fig. 5. 4 The simulation and experiment results of reflect beam at the exit pupil of objective lens for different separation distance between the center of focused spot and the edge of water droplet. The illustrations with label from (a) to (e) in first row show the setup configuration with different separation distance from 1 um to

-1 um. Second and third rows respectively reveals its corresponding reflect beam at the exit pupil of objective in simulation and experiment.

In the case (a) with 1 μm separation, the panel of simulation result reveals that the dark-resonance-ring suffer an asymmetrically lateral deformation, where the width of the ditch in left side is larger than that in right side. This is because the presenting water step would gradually raise the overall effective refractive index along the propagation direction of SPPs. As the refractive index step moved further, the left part of dark-resonance-ring is extended more even to reach the edge of the pupil. While the beam focused onto the air/water boundary as shown in case (c), it only displays a half set of dark-resonance-ring. This result gives us strong evidence that every SP wave is independent to each other. In this moment, only half part of focused beam impinges onto the air side. On the opposite side, it is forbidden to launch SP resonance at water/gold interface due to the shortage in angular spectrum of applying objective lens.

However, while the droplet covered the focused spot as shown in the case (d) with 500 nm separation, the dark-resonance-ring with crescent shape is replaced by a distinct constructive bright curve which referred to constructive interference at far-field. Moreover, bright parabolic-shaped curves continued rise followed initial one. There is no doubt that the plasmon spread on the metal surface suffers from discontinuousness of refractive index which causes some sort of interference and interferes with incoming light. More dramatic modulation on reflect beam is observed as the droplet moving further. From these results, it can be seen that the movement of index step does bring strongly influence on the field distribution of the reflect beam. As expected, the dark-resonance-ring creates an asymmetry deformation in lateral direction due to the inhomogeneously distributed refractive index. This azimuthal direction-orientated deformation also indicates the moving trajectory of test object. As we know that this conscious deformation is caused by the difference on optical

path between concentric wavelets of omni-directionally propagated SP and step-distributed refractive index of specimen. In short, the changing tendencies of patterns on reflect beam gives us a convenient observation window in far-field to monitor the moving orientation of test sample and to distinguish its little movement in the order of subwavelength.

5.2.2 Near-Field Sensing Radar

Based on our simulation and experimental results, it can be concluded that the boundary discontinuity along the metal surface would lead to interference between resonant and non-resonant wave. The most important thing is that the small variation caused by interference can be observed in far-field. Hence, in order to push the sensing application of collinear configuration further we propose a novel sensing concept called near-field sensing radar. It provides a convenient non-invasive technique, which has capability to trace the moving orientation or trajectory of a small object. The image capturing speed is associated to the frame speed of a CCD. The radial-polarization-generated SPPs are omni-direction propagating waves. Excited SPPs propagate away the center and create a series of concentric plasmon wave front which is similar to the water rippling caused by a stone falling into a peaceful lake. Excited SPPs wavelet act as a plasmonic scouts, they leave the center and detect any refractive index formed protrusion located along radial direction. Moreover, they are able to send the information back to far field by means of the interference of resonant wave and non-resonant wave than transport them to the exit pupil via objective lens.

To illustrate this concept, the movement of a sub-wavelength object was investigated. A tiny glass cube with half micrometer in each dimension lay on the flat metal with different separation distance. Figure 5.5(a) and 5.5(b) show the concept of near-field radar and its corresponding simulation results of disturbed electric field of SPPs among the metal surface

in the cases with 2.0 μm and 1.0 μm separation distance. The square with black outlines indicating the location of under-tested cube. It reveals that the concentrically wave front of propagating SPPs introduce different degree of interruption onto the wavelet. These fine variations interfere with incoming beam and directly reflect to the exit pupil as shown in Fig. 5.5(a_1) and 5.5(b_1) which revel the moving orientation of a small cube. At the exit pupil of Fig. 5.5(a_1), we can observe that the dark resonant ring at left side exhibits a slight expansion toward the edge and yields a constructive interference next to it. In the case of 5.5(b_1), a segmentation of expended dark resonant ring separate from original formation. The shift of this segmented deep shows an increasing on SPR angle caused by the higher effective refractive index mixed with the cube along radial direction. The difference between Fig. 5.5(a_1) and Fig. 5.5(b_1) is not significant, but it become pounced and contains analytical information through a designed algorithm of digital signal process. Figure 5.5(a_2) and 5.5(b_2) respectively shows the transformed data at exit pupil for both cases. The deformation of dark resonance ring is replaced by the spatial frequency of transformed pattern which provides a trustable character for determining relative moving orientation of the small objective .

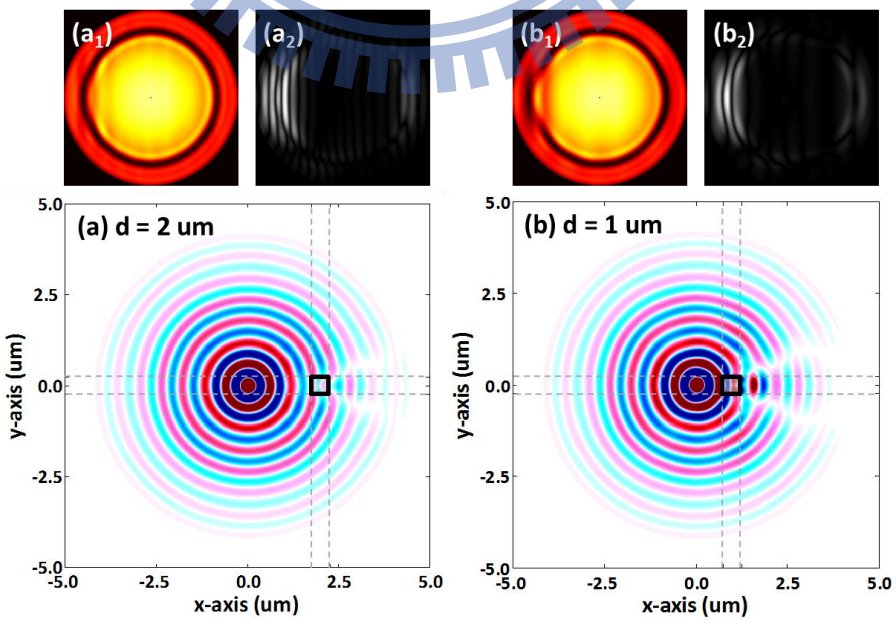

Fig. 5. 5 (a) and (b) are two groups of simulation results used to illustrate the

concept of near-field radar. Within the figure, the black squire depicts the tested cube with different separation distance for (a) 2 and (b) 1 μm. The cube is made by glass with half micrometer in each dimension lay on the flat metal. The red and blue mixed concentric wavelet shows the field distribution of Im [Ez] which is referred to plasmon wave among the metal surface. Figure (a_1) and (b_1) show the field distribution of reflect beam at the exit pupil. Figure (a_2) and (b_2) show the transformed results of field distribution at exit pupil which emphasizes the variation of the dark-resonance-ring through the spatial frequency at amplitude.

5.2.3 Short Conclusion

In summary, we investigate a corresponding link between the deformation of dark-resonance-ring on reflect beam and position of index edge related to the center of plasmon focus. An omni-direction propagated SPPs is excited by radial polarization, and it is able to sense the refractive index change among surrounding environmen. According to our simulation results, the boundary discontinuity along the metal surface significantly interrupts the SPPs wavelet and yields various interferences between resonant and non-resonant SPPs. In addition, this small variation in near-field could be observed at the far-field by means of destructive interference with incoming beam. The experimental results of the appearance of dark-resonance-ring at exit pupil show a good agreement with that of simulation results. It also experimentally demonstrates that the sensing resolution of the movement is beyond sub-wavelength. Furthermore, we also proposed a novel concept of near-field sensing radar based on this collinear configuration which provides the ability not only to sense the present of high refractive-index particle but also to detect its moving orientation and to measure its related distance. In the coming future, we believe this corresponding relation and the

concept of near-field sensing radar have highly potential for applying to trace the moving orientation of a single molecule in real time.

5.3 SPR Sensor Based on Polychromatic Radial Polarization

The necessity of relying wavelength-dependent optical elements to generate radially polarized light has been prevented to a large extent on RP-SPR sensor, thus precluding its transfer to practical use [50, 51, 73, 74, 76, 88, 92, 93, 100, 101]. A new optical element, based on the segmented spatially varying polarizer (SVP), was proposed to provide a broadband radial polarization filter, as shown in the inset of Fig. 5.6(a). It is composed of eight sectors of linear polarizer, the transmission axis of each sector aligned to individual principle radial direction [17, 88]. Unlike other attempts at making phase retardation feasible with specific wavelength [50, 51, 76, 92, 93], proposed scheme does not impose substantial limitations, and it therefore allows, for the first time, to achieve the white radially polarized beam via polarizer [102, 103]. In addition, for different operation purpose, the SVP device can be extended to create arbitrary stat of polarization without loss of generality. It is robust, compact in size with the benefit of low cost, and does not require interferometric accuracy in alignment. Figure 5.6b) – 5.6(d) shows the experimental far-field intensity distributions obtained for radially polarized beam without an analyzer [Fig. 5.6(b)] and after passing through analyzer in vertical and 45° orientation [Figs. 5.6(c) – 5.6(d), respectively]. The intensity distributions have two lobes, along a line parallel to the analyzer direction, as expected for an radially polarized beam. From the results of these experiments one can conclude that the polarization is close to ideal radial polarization.

5.3.1 Schematic Diagram of Poly Chromatic SPR Sensor

Figure 5.6 shows the schematic configuration of the polychromatic radially polarized enabling surface plasmon resonance (PRP-SPR) sensor, based on an inverted microscopy (Olympus IX81). A

white light source manufactured by Luxeon Star (LXHL-NEW8) was used to offer a collimated polychromatic beam. After passing through the SVP, a white radial polarized beam was tightly focused by an objective lens (Olympus PlanApo-N 60x/1.45 Oil) and launched upon the SPR coupler.

For typical objective based SPR coupler by Au monolayer, the operation range about refractive index is mainly limited by the marginal angle of the objective lens. Taking an example of oil immersion lens with NA = 1.45 (θ_{Max} ~ 75.16°), the maximum refractive index detectable is merely 1.28, which is much less than those of common living cell comparable with water (1.33) in visible spectrum [50, 93]. In this paper, we developed a metal/insulator/metal (MIM) sandwich structure as the SPR coupler to extend the operation range. Compared with Au monolayer coupler, the SPR is directly excited by the in-plane wavevector of the incident beam, additional insulator layer was inserted to arise a cavity resonance (CR) mode, results in a new SPR mode subject to the smaller in-plane wavevector. In order to maximum the depth of surface plasmon resonant dips, here we kept the symmetry of the MIM structure and set the overall thickness of Au thin film as 40 nm. SPPs were excited at the last interface (Au/medium) by the total internal reflection (TIR) mediated evanescent wave. The refractive index of the insulator should be the same as that of substrate to sustain the wave vector. As the consequence, we chose SiO_2 as insulator to maximize the angular range of TIR zone.

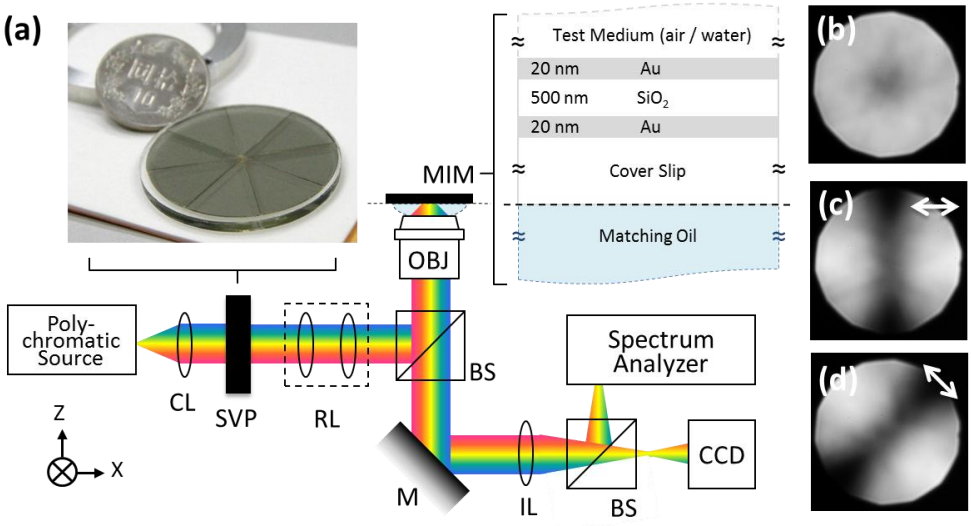

Fig. 5. 6 (a) the schematic diagram of white light RP-SPR platform, where CL: collimated lens, SVP: spatial varying polarizer, RL: relay lens, BS: beam splitter, IL: image lens, MIM: metal-insulator-metal structure. The insets show the experimental far-field intensity distribution of RP (b) before and after passing the beam through a polarizer in (c) vertical and (d) 45°, where arrow indicated the transmission axis of an analyzer.

5.3.2 The Functionality of MIM Structure

When the thickness of the SiO_2 layer is zero, MIM structure is reduced to a Kretchman configuration which reveals noticeable reflectance over entire angular spectrum excepting one dip in the vicinity of SPR angle, slightly larger than critical angle θ_{TIR} ~ 41.87°. As the thickness of the SiO_2 layer increases, reflectance at small angular spectrum are naturally caused by the interference between the multiple reflections within a Fabry-Perot-like resonator. With the same incident angle, the resonance would occur periodically as the insulator thickness is the integer multiple of half wavelength [25]. Meanwhile, the CR modes at large angular spectrum are likely to be coupled into SPR, which exhibits a large extent of evanescent fields into the air and serves as the mechanism of sensor applications. Because of the presence of SiO_2 layer with sufficient thickness (d_3>150nm), the coupled SPR mode would exist subject to smaller propagation constants, effectively provides the capability to detect a sample with higher refractive index at the same incident angle, it also have obviously angular shift and linear dependence in sensitivity.

Aforementioned behavior can be confirmed by Fig. 5.7(a). With n=1.33 water medium, the reflectance dip would exceed the border of the pupil, thus no SPR is generated at shorter wavelength of a monolayer Au SPR-sensor. For the MIM structure, on the other hand, coupled

SPR mode induces a sharp resonance dip cover the visible region, as shown in Fig. 5.7(b). The corresponding dark ring can be experimentally observed at the exit pupil, where three selective wavelengths across the visible spectrum (λ = 610nm, 530nm and 450nm) exhibit the individual resonance conditions. The experimental results were in close agreement with the simulation and prior literature with monochromatic light (Fig. 3, [50]).

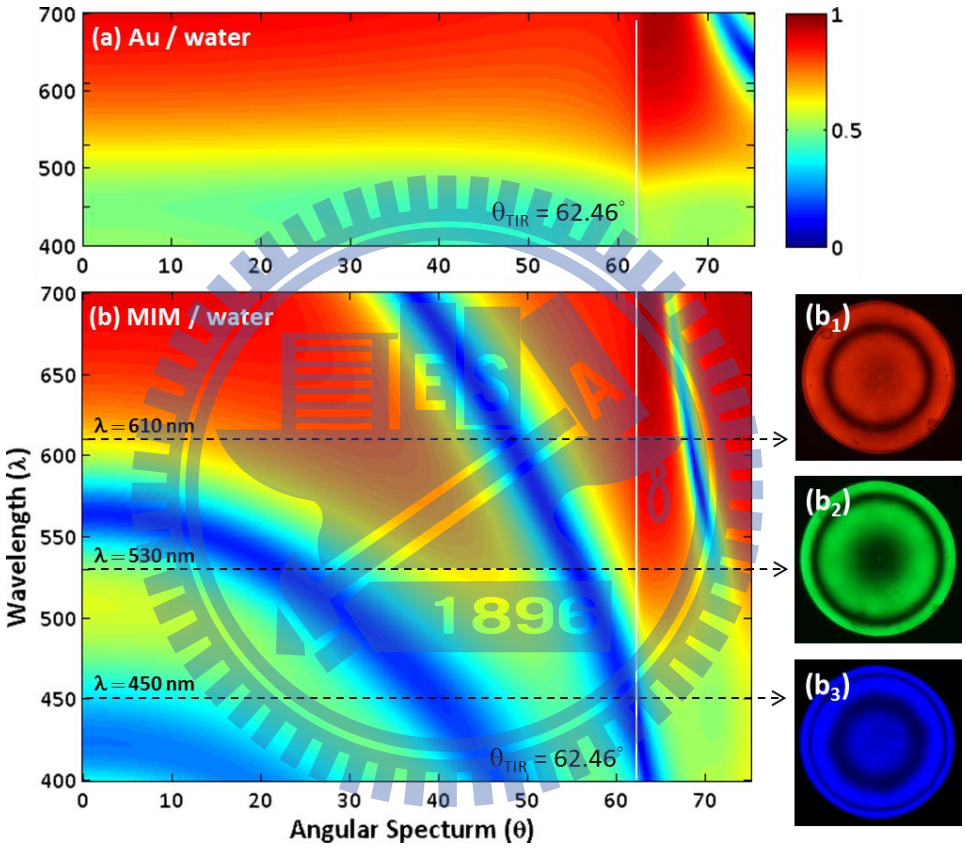

Fig. 5. 7 the wavelength dependent angular reflectance when the medium above the (a) Au monolayer and (b) MIM structure is chosen to be water. Experimental results of dark resonance ring respected to wavelength on 610 nm, 530nm, and 450 nm, where (b1)-(b3) are the case of MIM/water.

5.3.3 Rainbow Concentric Ring

By tightly focusing a polychromatic radially polarized beam on the Au(20nm) /SiO2(500nm)/Au(20nm) sandwich structure, we are able to embed the existence of angular and spectral surface plasmon resonance (SPR) in a unique far-field plasmonic rainbow rings, as shown in Fig. 5.8, where a two-dimensional snapshot of SPR excitation can be observed in a wide operation range of wavelength (λ=400~700 nm) and angular spectrum (θ = 0~75 degree).

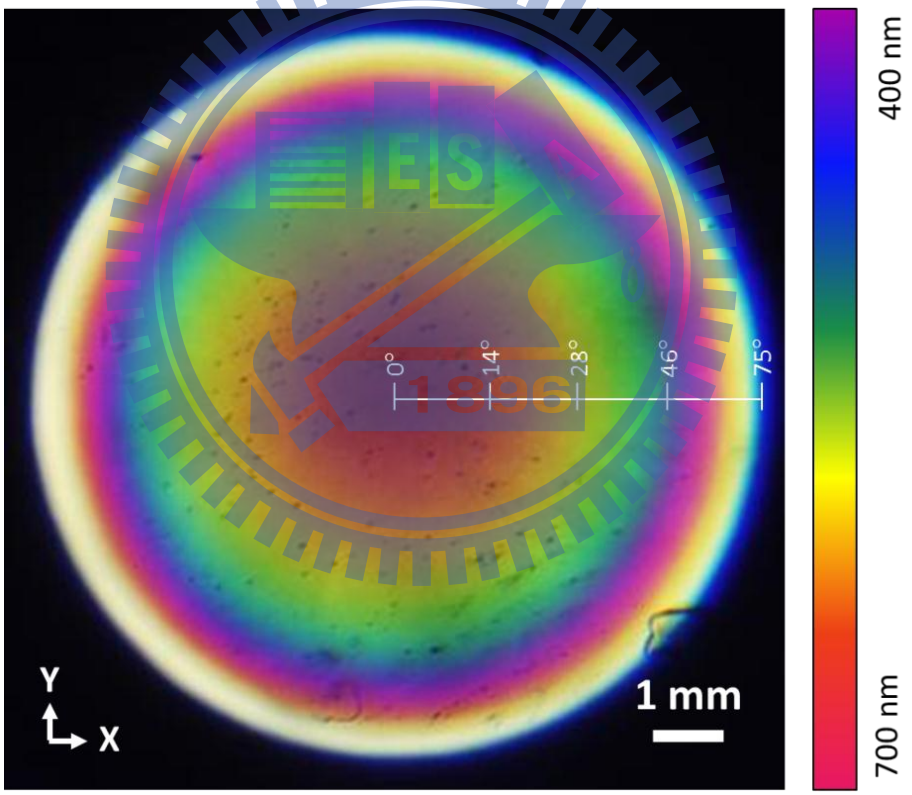

Fig. 5. 8 the experimental result of white light radial polarization induced rainbow concentric ring captured at the exit pupil of objective lens.

5.3.4 Spectrum Analysis

Combined with the real-time spectrum acquisition system (Chung-Yu Co., USB-100), we are able to further extend the colorfully static state to the dynamic situation. A proof-of-concept scenario was demonstrated by increasing the concentration of NaCl solution. The change of concentration leads to the deformation of rainbow rings which can be quantified and differentiated by the integral of individual colorband from colorful rainbow rings via spectrometer. The normalized differential reflectance spectrums (DRS) shown in Fig. 5.9 were recorded data of the measured spectrum by removing the baseline of the pure water as the concentration of NaCl solution reached to $\rho = 10\%$, 20%, 30%, and 40% of saturated condition. They exhibits a linear change as the concentration increased. In addition, by employing the difference of DRS with respect to the concentration change between 10% and 20% among the entire spectrum, defined as $\Delta DRS/\Delta\rho$, three peaked wavelength (462 nm, 551 nm, and 660 nm) were found to be the most sensitive as the observation windows to monitor the concentration change of a salt solution. We expect the proposed scenario to be a useful reference for researchers to find the proper wavelength and refractive index on the study of unknown bio-chemical interaction.

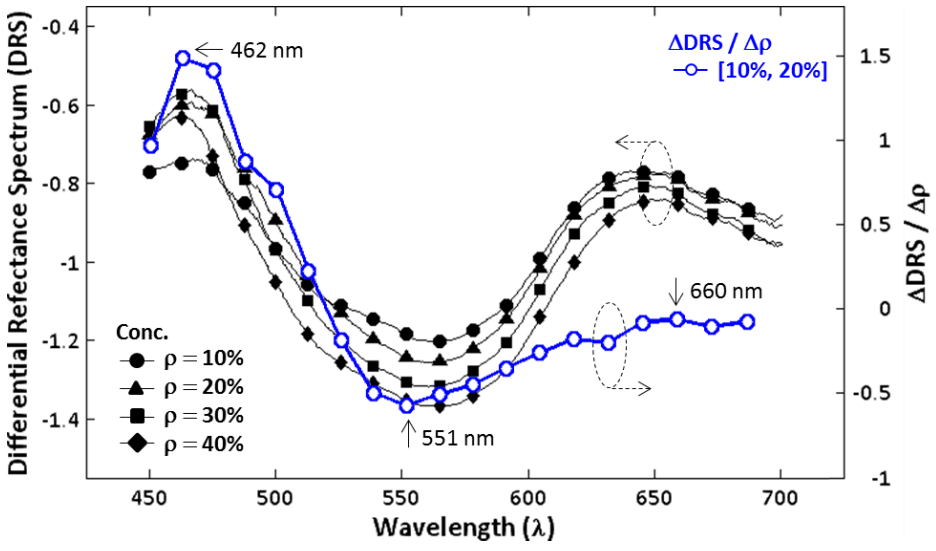

Fig. 5. 9 the experimental results of the normalized DRS between different concentration of NaCl solution from $\rho = 10\%$ to 40%. The blue curve with open circle shows the slope of DRS change with respect to the interval of $\rho = 10\%$ to 20%.

5.3.5 Short Conclusion

In summary, we demonstrated a unique pattern with rainbow concentric ring which is generated by a white light RP-SPR sensor integrated with a broadband radial polarizer and a MIM light coupler. Based on this configuration, a full color SPPs wave is able to excite and use to sense test samples with refractive index up to 1.42 cover most of living cells. The rainbow concentric ring is rich and embeds all of SPR information regarding to angular and wavelength spectra of a subwavelength-sized local region. The sensitivity of this sensor could be further enhanced by coating gold nanoparticles on the top of metal surface. Also, it can integrate with super continuum laser source to exploit surface-enhanced Raman scattering for more applications. Moreover, a two dimensional wavelength dependent refractive-index map of cell structure could be achieved via a raster scanning operation. As a result, we believe proposed methodology might certainly have a promising impact on using SPR sensor for monitoring the physical properties of biomacromolecules and protein-protein interactions.

Chapter VI

Apply Radial Polarization to Conventional and Nanorod Based ODS System

The desire of pursuing smaller focused spot is a kind of human nature. The driving force on this issue came from the huge demand of applications on higher resolution in microscopy, larger recording capacity in optical data storage, and finer exposure line width in lithography. The ultimate goal of them are that they all are looking for “smaller focus spot” in terms of the point spread function for spatial domain and transfer function in special frequency domain. Until now, the size of the smallest focus spot we can achieve right now is still governed by the diffraction limit of the scalar diffraction and vectorial diffraction theory. It is not easy to break, and the parameters of wavelength and numerical aperture only provide a scalar shrinking effect.

However, owing to the polarization property of radial polarization, it can achieve 20% smaller focused spot in terms of the cross section area of focal plane. This benefit comes from the constructive interference of projected electric field at the axial direction without the need to break diffraction limit. In this chapter, we are going to apply radial polarization to conventional optical data storage (ODS) system as well as novel nano rods based optical data storage. At the former one, we apply radial polarization to conventional ODS system and study the response of its servo singles. At the later one, we utilize the strong longitudinal component brought by radial polarization to melting out-of-plane gold nano rods for larger recording capacity.

6.1 Servo Study of Radially Polarized Beam in High Numerical Aperture Optical Data Storage System

The size of the focus spot in optical data storage (ODS) systems is determined by the scalar diffraction ~ kλ/NA, where λ is the free space wavelength and NA is the numerical aperture of the objective lens. The factor k is of order unity and depends on the pupil function. Substantially, in order to increase the recording density, it is desirable to pursue shorter wavelengths and higher NA. However, when NA is increased, scalar prediction is not sufficient to describe the vector properties of the focused beam, and a study based on full vector diffraction treatment is needed. The vector properties not only affect the local field polarization but also the intensity distribution at the focus. Recently, a radially polarized doughnut field synthesized by the superposition of two orthogonal Hermite-Gaussian modes has attracted much attention due to the appearance of a strong longitudinal field component and a sharper far-field focus centered on the optical axis [6, 15, 34, 35]. To ensure that such a peculiar polarization mode can be made applicable to conventional ODS systems, many issues such as focusing and a tracking scheme should be further examined [52]. In this topic, we employed full vector diffraction treatment to study the dependence of the servo signals to the novel focus radiation of a radially polarized beam and the resistance to the primary aberrations caused by the operation of ODS systems.

Since the effect of the vector properties of the polarization is proportional to the NA of the optical system, in this letter, NA was assumed to be 1.0 and the pupil to be unobstructed; the length unit is normalized by the wavelength. Figure 6.1 shows the calculated two-dimensional pupil and focus irradiance with linear (LP) and radially (RP) polarized illumination. For LP illumination, the focus spot is elongated along the incident polarization due to the depolarization effect in the focal region of a high-NA system. In the case of NA = 1.0, the spot size full width at half maximums (FWHMs) are 0.75λ×0.53λ. This asymmetry would lead to an undesirable deviation of the servo signals. In contrast, the radial

polarization is a type of inhomogeneously polarized light that can be described as the superposition of two orthogonal first-order Hermite-Gaussian modes (TEM_{10} and TEM_{01}). When it is focused using a high-NA objective lens, the radial component on the pupil plane

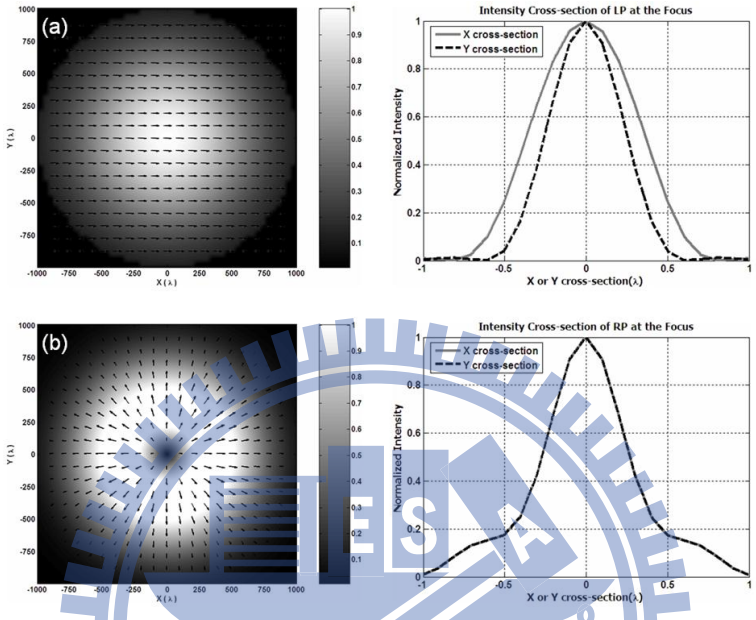

Fig. 6. 1 Comparison of intensity distributions for linear (a) and radial (b) polarizations. The left side shows the normalized intensity distribution on the transverse pupil plane and arrows represent the direction of polarization. The right side shows profiles of the normalized intensity at the focus, which is focused by an objective lens of NA=1.0. Solid line: profile along X cross section, dashed line: profile along Y cross section.

contributes to a strong longitudinal electric field, with a surrounding doughnut-shaped transverse field created by the azimuthal component [35]. The total field distribution is dominated by the longitudinal component and exhibits a rotationally symmetrical spot size of 0.54λ (FWHM). To discuss the impact of the radially polarized beam on the servo signals, a modeling program based on full vector diffraction was developed to calculate the propagation of the laser beam throughout a conventional disk system, as shown in Fig. 6.2. A

laser beam is first collimated and passed through a beam splitter. An objective lens of NA $= 1.0$ was assumed to focus the light onto the disk; the reflected beam is then modulated as the spot scans over different positions. The reflected beam passes back through the

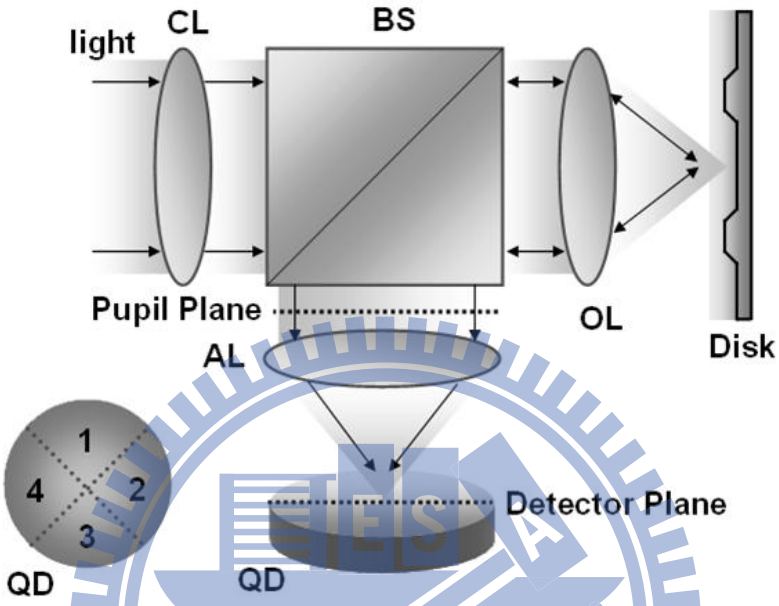

Fig. 6. 2 Configuration of high-NA conventional ODS system: CL, collimator; BS, beam splitter; OL, objective lens; Disk, pre-grooved disk (track pitch $= 2\lambda$, land width $= 1.375\lambda$, groove width at top $= 0.625\lambda$, groove width at bottom $= 0.375\lambda$, groove depth $= 0.125\lambda$); AL, astigmatic lens; QD, quad detector.

objective lens and is directed toward the quad detector by the same beam splitter. Grooves on the disk that define tracks produce fixed diffraction orders of the reflected light. The behavior of the fringe patterns on the pupil plane depends on the interaction of the focused field with the features on the optical disk. Figure 6.3 shows the modulated pupil patterns as the focused spot scans through the focus $(2{-}1{-}3)$ and cross-track $(4{-}1{-}5)$ directions. Compared with the well-known baseball patterns of the linear polarization, the on-axis null and the annular intensity modulation of the radially polarized illumination, the characteristics of axially symmetric beams are easily observed. For radial polarization, the

opposite sides of the transverse electric component are out of phase, which would not convey any information of the disk. Similar to the paraxial annular case, radial polarization and an annular pupil can be used to reduce the transverse field and obtain a sharper central lobe. It is expected that using such an arrangement for illumination will allow us to obtain super-resolution with a corresponding effect on the servo detection.

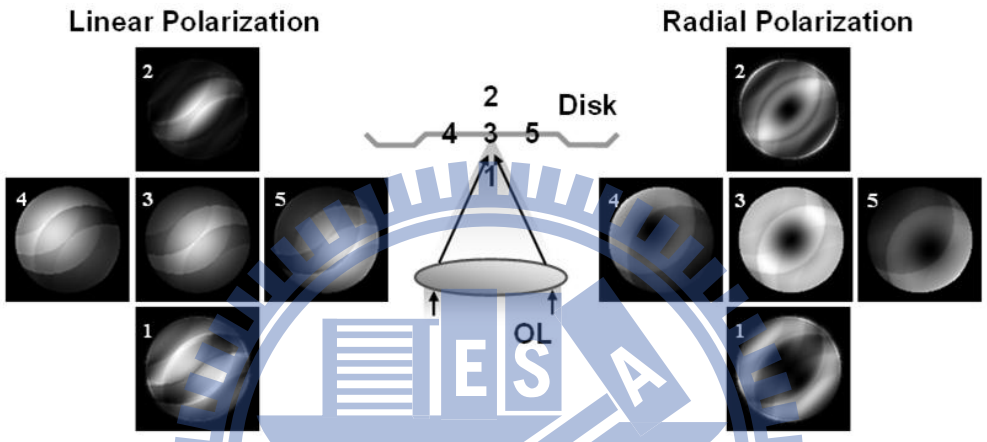

Fig. 6. 3 Intensity patterns of reflected light from disk for different polarizations (black corresponds to zero irradiance and white corresponds to the brightest irradiance).

During the read/write/erase operations, two major areas of concern are keeping the spot in focus and following the track in the radial direction. In this paper, numerical analysis was carried out to obtain the astigmatic focus-error signal (FES) and push-pull tracking-error signal (TES) for different polarized illumination. As shown in Fig. 6.4(a), for the linearly polarized beam, the focal spot is elongated along the incident polarization due to the depolarization effect leading to a 14% asymmetric FES compared with the radial polarization. In addition, FES versus defocus with 0.25λ spherical aberration (SA) was also calculated to examine the tolerance under different polarizations. When the light has a large incident angular spectrum in a spherical aberrated optical system, the transmitted components

undergo a phase change depending on the angle of incidence and polarization direction [57]. For a linearly polarized illumination, the phase change is affected by the transverse component more than the longitudinal component. Because radial polarization exhibits a strong longitudinal field ~10X higher than the transverse component in NA = 1.0, the FES curve with 0.25λ SA has no deformation and only 0.3λ offset, which can be easily compensated by the defocus. Figure 6.4(b) shows the tracking-error signal (TES) when the focal spot moves along the cross-track direction. Note that the elliptical focus spot of LP would easily result in erroneous judgment near the land center where the zero slope of the curve occurs. For RP, the erroneous judgment near the land center can be avoided. However, if the light was focused on the groove center, the surrounding doughnut-shaped transverse field would meet the edge of the groove and lead to an erroneous judgment. Moreover, if SA was introduced into the optical system, the flat curve near the land center for LP and the groove center for RP would deteriorate.

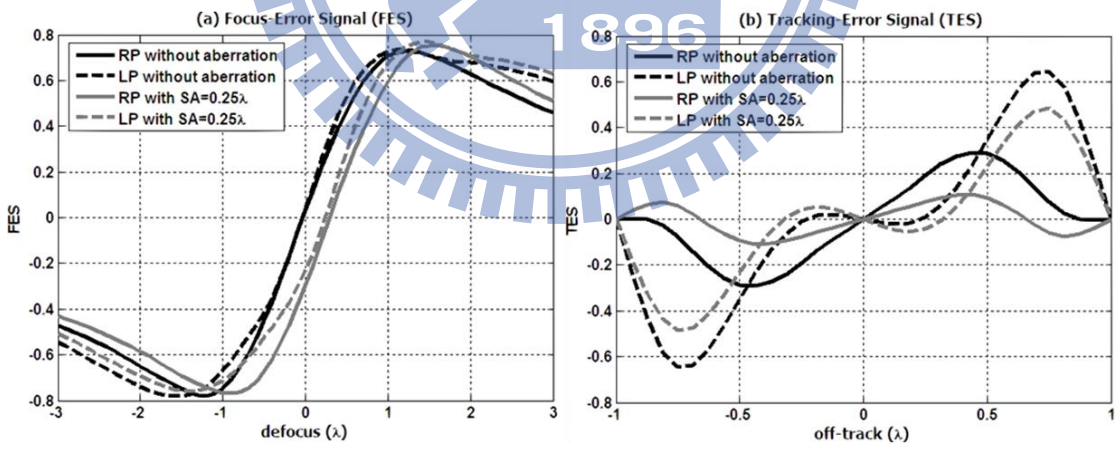

Fig. 6. 4 Servo signal comparison. The calculated focus-error signal (a) and tracking-error signal (b) were considered with different polarizations and with/without spherical aberration. For polarization type, the dark line and gray line rperesent radial polarization and linear polarization, respectively. For the amount of spherical aberration, the dashed line and solid line represent 0.25λ spherical

aberration and no aberration, respectively.

During seeking operations, as the focused spot scans the disk in search of a targeted track, diffraction from the grooves creates a false FES; this problem is referred to as “feedthrough”. Figure 6.5 shows the calculated FES for various weak aberrations when the spot moves along the cross-track direction. Compared with the LP shown in Fig. 6.5(a), RP has a feedthrough variation reduction of at least 56% in all 0.25λ aberration cases. In addition, on-axis aberrations such as spherical aberration does not destroy the rotational symmetry of the field near the focus. The beam preserves both longitudinal and transverse components at the focus. Therefore, SA only slightly influences the curve near the groove center and induces a dc level on the feedthrough for radial polarization.

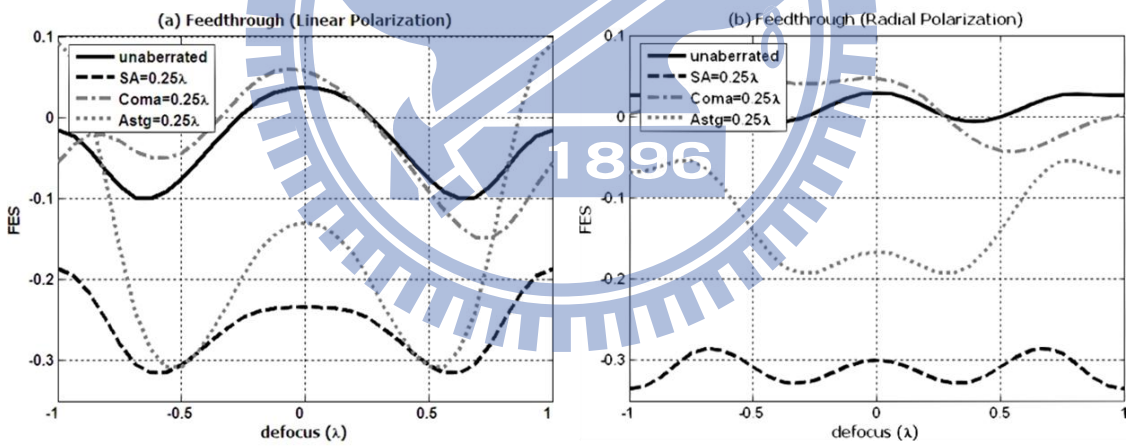

Fig. 6. 5 Comparison of feedthrough. Feedthrough is the crosstalk signal between the focus-error signal (FES) and the tracking-error signal (TES). The results for different 0.25λ aberrations are shown for LP (a) and RP (b).

In summary, the servo study of a high-NA ODS system by utilizing radial and linear polarization beams has been carried out. The radially polarized beam has a superior performance on ODS system than the linearly polarized beam because of the smaller spot

size at the focus and symmetry polarization. For example, it provides a higher recording density, 14% asymmetry reduction in the linear range of the FES, and at least 56% variation reduction in crosstalk for each aberration. However, if radial polarization was applied to the conventional ODS system, two issues need to be considered. First of all, in the TES, the noise increases slightly on the notch of the reflected light; therefore, the TES would become flat on the groove center. Second, only a high-NA objective lens generates a strong longitudinal field component with a sharp focus and, consequently, compatibility would be an issue that needs to be further examined.

6.2 Nanorod Mediated Optical Data Storage

Optical data storage has led to revolutionary advances in information technology and storage. One of the challenges in this field is to meet the rapid growth in demand for storage capacity. Bit-by-bit optical data storage systems such as compact discs (CDs), digital video discs (DVDs) and Blu-ray discs (Blu-rays) have emerged as compact, portable devices that have high memory density and high resistance to intense electromagnetic radiation. Given its high tolerance to vibration and robust reliability, bit-by-bit optical storage has been shown to be superior to holographic memory.

Over the past ten years, researcher has been tried very to increase the recording density in optical data storage. The current technology that we are using is Blu-rays which is operate at a much shirter wavelength of 405 nm as well as higher NA to 0.85. But still, the recording area is still working in a two-dimensional system. In a 2-D optical data storage system, where information is recorded only in one layer inside the medium, 99.99 percent of the volume of the optical disc has not been used. Researchers have pursued further research to explore the feasibility of three-dimensional (3-D) optical data storage, such as double-layer DVDs and double-layer Blu-ray discs. However, the increased number of recording layers is

insufficient due to the penetration depth of shorter wavelength is poor. Therefore, the single photo operation has been replaced by two-photon (2P) excitation via infrared femtosecond pulsed laser beam due to its highly confined properties and high efficiency of penetration into the volume of a recording medium. The 2P excitation technique has been widely applied to a variety of materials for high-density memories, including photopolymerizable materials, photochromic materials, photorefractive materials, photobleaching materials, void-fabricatable materials and nanoparticles dispersed materials [104]. The latest milestone that scientists have achieved in the development of high-density 3-D storage system was demonstrated by Walker et al. to achieve 1TB per disc in a 200-layer disc [105, 106].

But so far, all of the technology that we mentioned above is to record information in a 3-D domain. If one can introduce additional dimensional on current 3-D storage, then the capacity could be increased significantly. This thinking comes out the idea of a multi-dimentional system. The idea behind multi-dimensional optical data storage is to multiplex multiple states of information in the same 3-D spatial region of a recording medium. The information can be encoded into additional physical dimensions of the writing beam, such as spectra or polarization, and then individually addressed. The ground-breaking techniques of polarization and spectral encoding are the core of third-generation optical data storage. These approaches, which are not limited by the spatial resolution of recorded bits, allow capacity to be expanded by orders of magnitude. The first multi-dimentional optical data storage was proposed in 2007 by Li *et al* [107]. It was achieved by using two state of polarization through the 2P-induced re-orientation of azo dyes inside a photopolymer. Furthermore, a 2009 Nature article, Zijlstra and colleagues demonstrated that gold nanorods, combined with the sharp 2P-induded polarization sensitivity, enable information to be recorded in five dimensions [108].

Wavelength and polarization do provide additional freedom on recording, but it still got a plenty of room for scientist to further increasing the recording capacity due to the

material idle. Figure 6.6 illustrates a normal bulk media of polymer which has embedded nanorods. Normally, the orientation of embedded nanorods reveals random distribution. Here, we can simply divide them into in-plan and out-of-plane nanorods. In the pervious research, Zijlstra applied two state of linear polarization to shorten the length of in-plane oriented nanorods by increase the laser power. Based on the statistical estimation, the population of in-plane nanorods is one third amoug the entire nanorods. Therefore, rest of out-of-plane nanorods which are not participated in recording process would become a waste of material usage. By enrolling all of the out-of-plane nanorods inside the polymer, the capacity would be increased. This chapter we are going to using the strong longitudinal component of the focused radial polarization to utalize out-of-plane nanorods for the purpose of higher recording density.

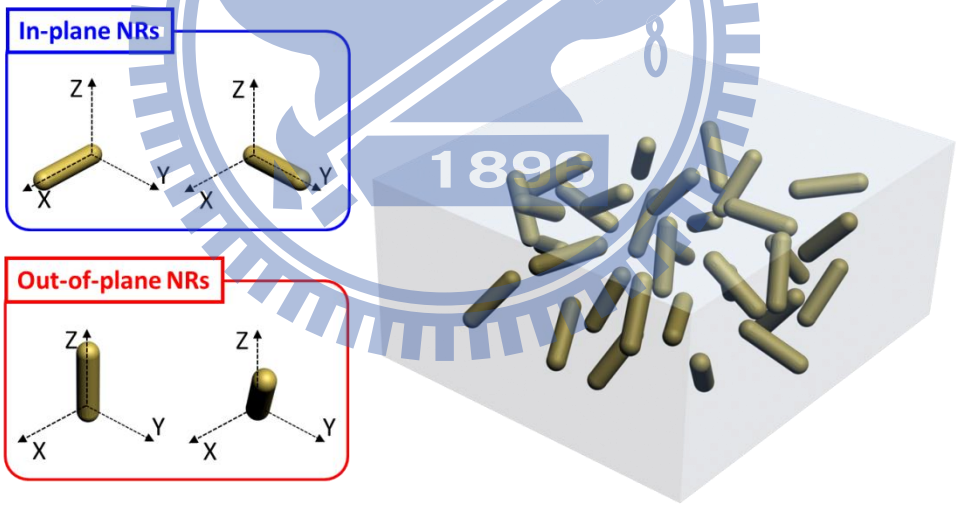

Fig. 6. 6 Schematic diagram of a random dispersed nanorods inside a bulk polymer media.

6.2.1 Synthesis of Nanorods

In order to study gold nanorods and use them in any application a reliable and large scale synthesis method is required. Various methods have been established for the synthesis of metal nanorods [109]. A templated method was first introduced by Martin and co-workers [110, 111]. This method is based on the electrochemical deposition of gold within the pores of nanoporous polycarbonate or aluminium template membranes. The gold nanorods were contained in the template to form a nanocomposite in which the aspect ratio of the nanorods can be controlled by varying the size of the pores. Van der Zande and co-workers later showed that a colloidal solution of nanorods could be obtained by redissolving the template [112, 113]. The fundamental limitation of the template method is the low yield, which makes it commercially unattractive. Larger scale synthesis can be accomplished by the widely used wet chemical synthesis method. Wet chemical synthesis includes electrochemical [114, 115], seeded [116, 117], and seed-less growth [118] methods. These methods are conducted in aqueous surfactant media which direct the nanoparticle growth by providing anisotropic micellar templates [119]. Here we will restrict ourselves to the seeded growth methods because they are more attractive methods for large scale synthesis.

The seeded growth method was developed by the groups of Murphy et al. [116, 118, 120] and El-Sayed et al. [117, 121, 122]. It was derived from the seeded method used to grow large gold nanospheres [109, 123]. The seed particles were 3.5 nanometer in diameter prepared by borohydrade reduction of gold salt. By controlling the growth conditions in aqueous surfactant media it was possible to synthesize gold nanorods with tunable aspect ratio using this method. The surfactant generally used to synthesize gold nanorods is cetyltrimethylammonium bromide (CTAB), which forms rod shaped micelles above the second critical micelle concentration (~ 20 mM) [124]. The surfactant forms a bilayer on the surface of the nanorod and directs the nanorod growth by preferentially binding to the

crystal faces along the length of the particle [122, 124].

It was found that addition of $AgNO_3$ influences not only the yield and aspect ratio control of the gold nanorods but also the mechanism for gold nanorod formation and correspondingly its crystal structure [109, 125, 126]. Subsequent reports have found that gold nanorods prepared in the presence of $AgNO_3$ are single crystalline with a [100] growth direction [125-127]. When no $AgNO_3$ is present the rods grow in the [110] direction and exhibit a multiply twinned crystal structure [128]. Liu et al. recently reported that silver acts as a surface structure specific surfactant [109]. They concluded that silver deposits selectively on the more open {110} facet of the gold rod, slowing down the growth of this facet which results in better control over the final aspect ratio.

The seeded growth method in the presence of AgNO3 yields gold nanorods with a controllable aspect ratio up to ~ 4.5 (longitudinal SPR ~ 825 nm). The group of El-Sayed et al.28 later modified this method to allow synthesis of higher aspect ratios. Instead of using a single surfactant they proposed a binary surfactant mixture composed of CTAB and Benzyldimethylhexadecylammonium Chloride (BDAC), yielding nanorods with an aspect ratio up to ~ 10 (longitudinal SPR ~ 1300 nm).

In experiment, Ascorbic acid, $AgNO_3$, and NaBH4 were purchased from Sigma-Aldrich. Cetyltrimethylammonium bromide (CTAB) was purchased from Alfa-Aesar. Benzyl-dimethylhexadecylammonium Chloride (BDAC) was purchased from TCI America. $HAuCl_4 \cdot H_20$ was purchased from ProSciTech. All chemicals were used without further purification. Distilled water was used for the preparation. Preparation of CTAB capped gold seeds: Gold seeds were prepared in a 10 mL aqueous solution containing 0.1 M CTAB and 0.25 mM $HAuCl_4$. To this solution was added 0.6 mL of a 16 mM ice-cold, aqueous $NaBH_4$ solution under vigorous stirring. Stirring was continued for 30 seconds after which the seed solution was put aside for 1 hour to ensure removal of excess $NaBH_4$.

Preparation of gold nanorods with aspect ratios <4.5 : Gold nanorods were prepared

using a $AgNO_3$ assisted, seed-mediated growth method, based on the system developed by El-Sayed et al [117]. To the growth solution ([CTAB] = 0.1 M, [$HAuCl_4$] = 0.5 mM) we added a certain amount of $AgNO_3$ depending on the required aspect ratio, and 0.75 mM freshly prepared ascorbic acid. Initiation of the nanorod growth was achieved by adding 6 µL per mL of the growth solution while stirring.

Preparation of gold nanorods with aspect ratios >4.5 : These particles were prepared using a binary surfactant mixture [117]. To the growth solution ([CTAB] = 0.025 M, [BDAC] = 0.075 M, [$HAuCl_4$] = 0.5 mM) we added different amounts of $AgNO_3$ and 0.75 mM freshly prepared ascorbic acid. Initiation of the nanorod growth was achieved by adding 6 µL per mL of the seed solution while stirring. Preparation of large volume gold nanorods: Larger volume nanorods were prepared using a low seed concentration. To the growth solution ([CTAB] = 0.1 M, [$HAuCl_4$] = 0.5 mM) we added different amounts of $AgNO_3$ and 0.6 mM freshly prepared ascorbic acid. Initiation of the nanorod growth was achieved by adding 1 µL per mL of the seed solution while stirring.

6.2.2 Two-photon Luminance of Out-of-plane Nanorods

Small metal particles exhibit complex optical and physical properties. Their small sizes (< 100 nm) cause strong confinement of the electrons, giving rise to fascinating effects not observed in the bulk material. The most striking phenomenon encountered in metal nanoparticles are electromagnetic resonances due to the collective oscillation of the conduction electrons. These so called localized surface plasmon resonances (SPR) induce a strong interaction with light, and the wavelength at which this resonance occurs depends on the local environment, shape, size and orientation of the particle [129-131].

The role of a nanorod is a perfect light absorber which can be used to indicate the orientation of a nanorod. Figure 6.7 shows the experiment results of polarization

dependence luminance intensity. The gold nanorods were synthesized by the seeded method having the aspect ratio ~ 4 which have a maximum extinction at the wavelength of 780 nm. By focusing linearly polarized light onto the nanorod with a 1.4 NA objective, the nanorod is able to generate a two-photon luminance (TPL). The strength of its luminance depends on relationship between the orientation of nanorod and the polarization distribution at the focus. The maximum luminance would be generated when the polarization axis of illumination beam is parallel to the longitudinal axis of nanorod. In contrast, there is no luminance as the polarization is perpendicular to the longitudinal axis of nanorod, as shown in Fig. 6.7(a). By controlling the polarization angle of linear polarized light through a half-wave plate, one can plot its intensity variation versus the rotation of incident polarization, as shown in Fig. 6.7(b). The strength of TPL is polarization angle dependence and exhibits a relation which is directly proportional to the four square of cosine theta multiplied by electric field $\mathrm{I}(\theta) \propto (\mathrm{E}\cos\theta)^4$. The orientation angle of an in-plane nanorod could be determine by this dipolar cosine fits.

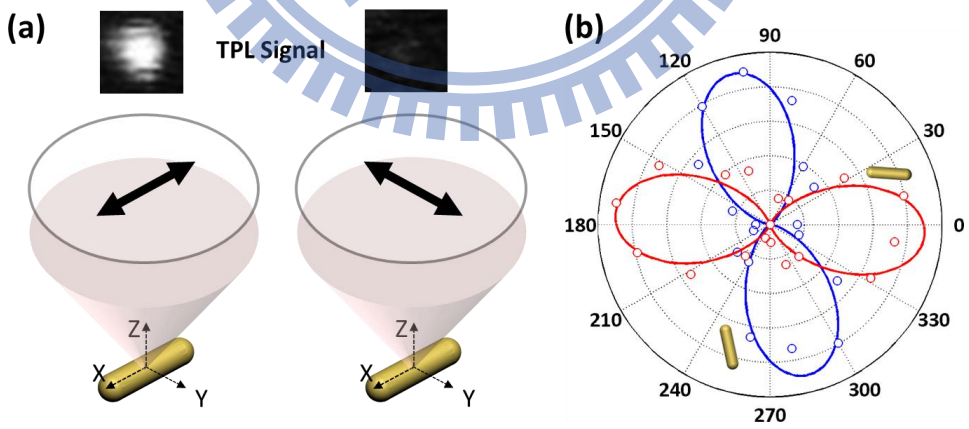

Fig. 6. 7 Imaging gold nanorods. (a) Schematic diagram of the link between polarization and the intensity of TPL. (b) Polarized TPL versus angle, with dipolar cosine fits.

However, this method is only suitable for detecting in-plane nanorods and some of out-of-plane nanorods with small title angle. Most of standing nanorods cannot be detected due to the weak projection from out-of-plane to in-plane. In this case, an axial polarization at the focus is needed for handling standing nanorods. By means of pupil polarization engineering, one can create an axial polarization at the focus. Figure 6.8 shows the field distribution of TPL excited by different state of polarized illumination under the strong focusing condition (NA = 1.4, λ = 780 nm). By using linear polarized light to determine the orientation of nanorods, one should take at least three images by rotating the polarization cover 0, 45 and 90 degrees. In contrast, azimuthal polarization provides a better route providing fast detection based on a single shot. This is because the field distribution of its focus is spatially varied in polarization and rotational symmetry in amplitude. As a result, one can observe a pair of lobes rather than a perfect donut shape on its TPL. This pair of lobes is central symmetry along the axis of zero intensity which is the degeneration of original donut shape. This null axis is parallel to the longitudinal axis of nanorods. Based on this link we can easily determine the orientation of nanorods without the need of rotating polarization angle.

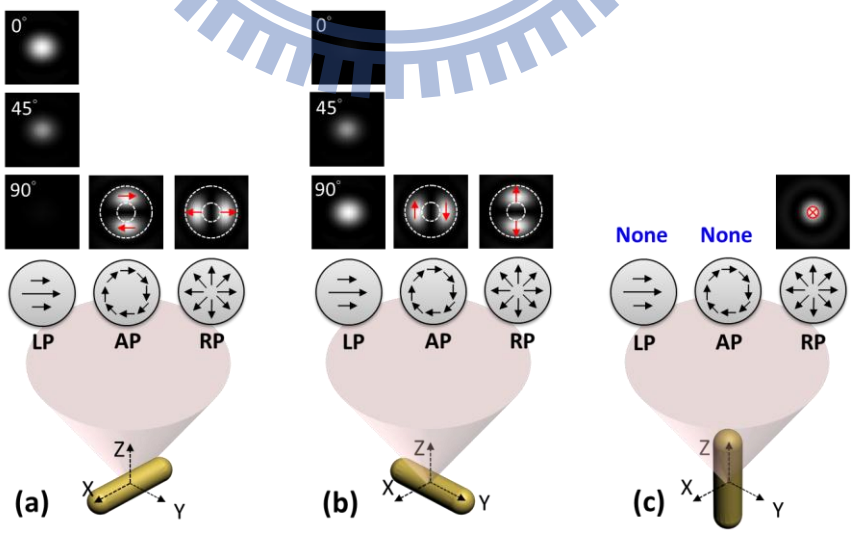

Fig. 6. 8 Field distribution of TPL excited by different state of polarized illumination under the strong focusing condition (NA = 1.4, λ = 780 nm). The

orientation of nanorod is in-plane and parallel to (a) x-axis and (b) y-axis, and (c) out-of-plane which is parallel to z-axis, the image width of TPL is 3 μm.

In addition, radially polarized illumination provides not only fast examination for in-plane nanorods but also additional link for standing nanorods due to its unique longitudinal component along axial direction based on the strong focusing. Generally speaking, radial polarization is a perfect illumination source for orientation detection which provides an entire response cover every orthogonal axis.

The size of a gold nanorod is significantly smaller compared to the size of focused spot. Therefore its luminance scanning image pattern resembles the point spread function of a focused beam. In experimental, we fix the position of objective lens and move the scanning stage of the nanorods sample. All of the excited TPL were collected by a high sensitivity PMT. In addition, a notch filter placed in front of PMT for blocking the strong reflectance of excitation light source. Figure 6.9 shows experimental results of TPL of godnanorods which is

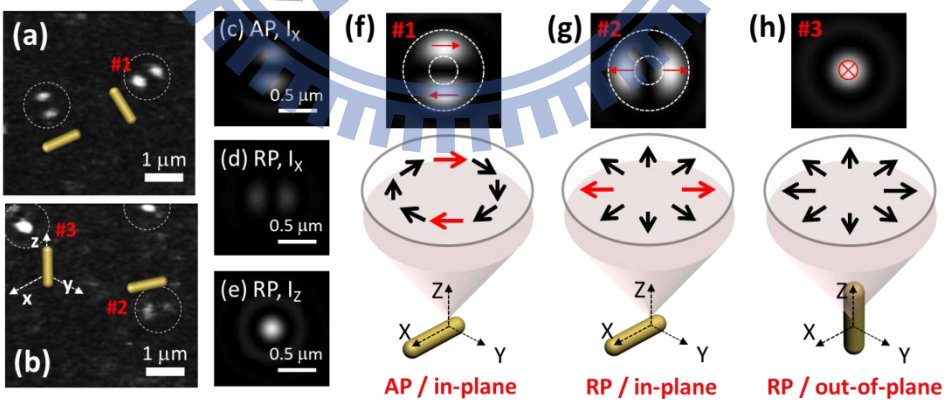

Fig. 6. 9 Experimental results of TPL of godnanorods. The raster scanning image of TPL of nanorods which is generated by (a) azimuthal polarization and (b) radial polarization. Dashed line encircle of mark #1 to #3 highlight the field distribution of TPL of nanorods and their individual schematic diagrams are shown in (f) to (h), respectively. The field distribution of focus is calculated under the condition of NA

=1.4, annular illumination of ε = 0.4, and λ = 780 nm for (c) azimuthal polarization and (d)-(e) radial polarization.

generated by (a) azimuthally and (b) radially polarized illumination. The same as our prediction, the field distribution of TPL image only exhibits a pair of lobes with different orientated angle which is depending on the orientation of nanorods. In the case of radially polarized illumination, a bright circle spot is also revealed which implies the existence of standing nanorods. Also, we can observed that the brightness of TPL of #2 is dimmer than that of #3. This is because the annular illumination purified the strength of longitudinal of a radially polarized focus. In the case of ε = 0.4, the ratio of peak intensity for them are $I_{X,AP}$: $I_{X,RP}$: $I_{Z,RP}$ = 0.6 : 0.25 : 1. This means the focus of radial polarization is not a pure longitudinal component; we still can observe the existence of transverse component which is not negligible. Figure 6.10 give us a strong evidence to support our theoretical prediction that we mentioned above. Before that, we have to dress a brief introduction on the excitation dynamics of small metal particles, in which the photon energy of a short laser pulse is converted to thermal energy and acoustic vibrations.

6.2.2 Photothermal Reshaping and Selective Melting

The excitation dynamics of metals on picosecond timescales has been widely studied using ultrafast spectroscopic techniques. Since the 1980s, a wide range of pump-probe studies on metal films [132, 133] and ensembles of metal nanoparticles [134-138] of various shapes and compositions have revealed a complex interaction between the excitation light source (most often a femtosecond laser pulse) and the conduction electrons and lattice of the particle. A generic series of events has been found in these studies, which largely applies to both metal films and nanoparticles. Firstly the excitation pulse sets the free electron cloud

into oscillation, and increases the electron temperature. The kinetic energy of the electrons is then conveyed to the lattice through electron-phonon coupling. When the excitation light pulse has sufficient energy, the lattice temperature increases to above the threshold melting temperature and the particle melts. The rapid rise in electron and lattice temperature is also responsible for the launching of a lattice oscillation in nanoparticles, most commonly referred to as acoustic vibrations. As a last step in the process the nanoparticle reaches thermal equilibrium with its environment through heat dissipation.

When the initial particle shape is non-spherical, the particles will reshape to the energetically more favored spherical geometry when the particle temperature exceeds the melting temperature. Consequently, gold nanorods can be efficiently reshaped due to their large absorption cross sections and high energy geometry. Link et al. [136] and Chang et al. [115] have studied laser induced reshaping of gold nanorods using UV-VIS spectroscopy. They found that laser irradiation depletes the population of nanorods which exhibit a non-zero absorption cross section at the laser illumination wavelength. This causes a bleach in the extinction profile around the laser wavelength and a pronounced color change can be observed. Because the longitudinal SPR of gold nanorods is very sensitive to the particle geometry, reshaping of gold nanorods results in large spectral changes which can be detected with straightforward spectroscopic techniques.

Therefore, by increasing the power of laser pulse, the lattice temperature would be increased and resulted in the photothermal reshaping. The process of nanorods reshape will lead to a blue shift of surface plasmon resonance. As a result, the TPL of nanorods will drop when the wavelength of excitation laser is fixed. Figure 6.10(a) shows the experimental results of contrast difference on the TPL of in-plane (blue curve) and out-of-plane (red curve) nanorods. The contrast of brightness is adopted by the definition of $\mathrm{C} = \frac{I_{max} - I_{min}}{I_{max} + I_{min}}$, where $0 < \mathrm{C} < 1$. Also, the I_{max} and I_{min} was calculated by the Gaussian fitting. The error bars

presented in Fig. 6.10 is the averaged value of around 10 nanorods on each point. Through the fitting line of averaged points, one can notice that the photothermal reshaping is a single photon absorbed process which demonstrates a linear dependence on the contrast difference versus the power of laser pulse. In this experiment, we only perform focusing radial polarization to melt the standing nanorods by increasing the power of laser pulse. But based on our results, we can found that we do melt not only out-of-plane nanorods but also in-plane nanorods which means the field distribution of the focused spot contained transverse component also. This is why the blue curve has a similar slop as red curve. When the power increased to 400 μW, the contrast difference observed at in-plane nanorods is the same as that of out-of-plane nanorods in the case of 180 μW. Fig. 6.10(b) and Fig. 6.10(c) respectively demonstrates the transition of photothermal reshaping of nanorods by observing the brightness change on TPL.

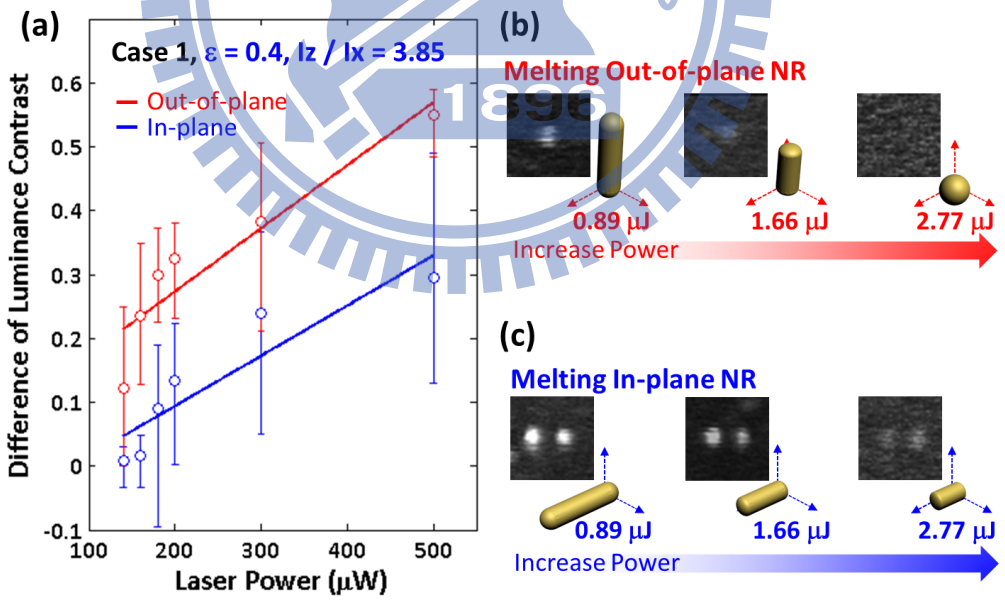

Fig. 6. 10 Experimental results of selective melting for standing nanorods by femtosecond pulsed laser with annular illumination of ε = 0.4 (Spectra-Physics Tsunami, 100 fs pulse width, 82 MHz repetition rate). (a) The contrast difference on TPL of godnanorods when the melting powering of focused radial polarization is

increased. (b) and (c) The transition of photothermal reshaping of nanorods by observing the brightness change on TPL.

The longitudinal component of a focused radial polarization can be further enhanced by increasing the ε value of the annular aperture. Figure 6.11 shows the calculated ratio of longitudinal to transverse component by increasing the ε value of the annular aperture. The ε of the annular pupil is defined by the ratio of outer radius to inner radius, as shown in Fig. 6.11(a). When the ε is increased to 0.7, the longitudinal to transverse ratio at the focus is 6.15. In this condition, the peak intensity of transverse component of the focused radial polarization is around 15% of that of longitudinal component, as shown in Fig. 6.11(c). In practically, the focus of radial polarization can be treated as a pure longitudinal component

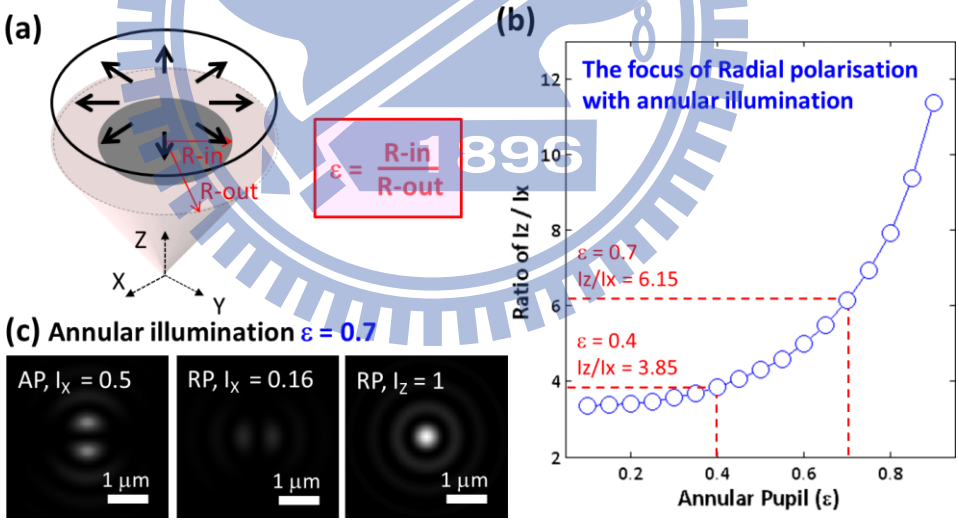

Fig. 6. 11 The effect of annular illumination. (a) The definition of annular aperture. (b) The chart of the ratio of longitudinal to transverse component versus the size of annular aperture. (c) The field distribution of focused spot for different component of different polarized illumination.

due to the traverse component is negligible. Again, we perform radial polarization to achieve

selective melting with the annular aperture of $\varepsilon = 0.7$. By determining the contrast difference of TPL before and after melting, one can evaluate the performance of selective melting, as shown in Fig. 6.12. It is notice that the slope of blue and red fitting curves is quite different comparing to each other. In the case 2 of $\varepsilon = 0.7$, only the out-of-plane nanorods were melted but in-plane nanorods still keep the contrast of TPL in a similar level. This provides a strong evidence that our theoretical assumption is correct to neglect the contribution of transverses component with comparable small amount electric field.

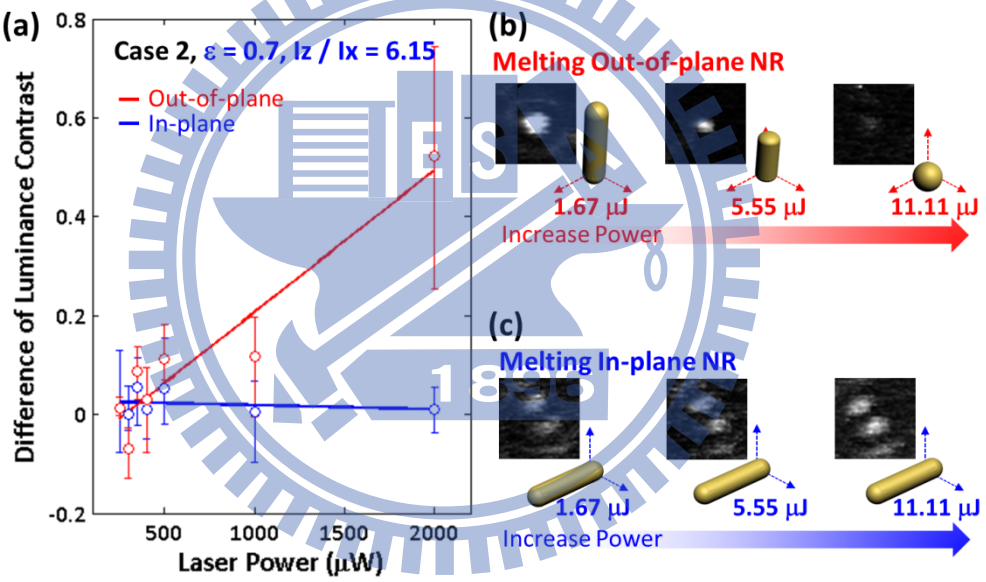

Fig. 6. 12 Experimental results of selective melting for standing nanorods by femtosecond pulsed laser with annular illumination of ε = 0.7. (a) The contrast difference on TPL of godnanorods when the melting powering of focused radial polarization is increased. (b) and (c) The transition of photothermal reshaping of nanorods by observing the brightness change on TPL.

6.2.4 Polarization Multiplexing Recording

Multiplexed optical recording provides an unparalleled approach to increase the information density beyond 1 Tbits/cm^3 by storing multiple, individually addressable patterns within the same recording volume. Although wavelength [139, 140], polarization [107, 141-144], and spatial imensions [145-149] have all been exploited for multiplexing, these approaches have never been integrated into a single technique which could ultimately increase the information capacity by orders of magnitude. The major hurdle is the lack of a suitable recording medium which is extremely selective in the wavelength, polarization and the 3 spatial domains in order to provide orthogonality in all 5 dimensions. Until a Nature article came out in 2010, Zijlstra et al. shown a true five-dimensional optical recording by exploiting the unique properties of the longitudinal surface plasmon resonance (SPR) of gold nanorods [108]. The longitudinal SPR exhibits an excellent wavelength and polarization sensitivity, whereas the distinct energy threshold required for the photothermal recording mechanism provides the axial selectivity. The recordings were detected using longitudinal SPR mediated two-photon luminescence provided an enhanced wavelength and angular selectivity compared to conventional linear detection mechanisms.

Here, we further increase the number of polarization recording state by introducing a longitudional component of focused radial polarization which can be treated as a pure axial polarization. The present of axial polarization would complete the polarization multiplexing recording. In order to demonstrate this concept, a bulk sample was prepared for polarization multiplexing recording. Gold nanorods with average aspect ratios of 4.1 were prepared using wet chemical synthesis. The nanorods was mixed with a 15 wt% polyvinyl alcohol solution, and dropped on a coverslip. Then, the sample was heated at 50 degree for 1 hours. The thickness of this layer was 5 um. The approximate nanorod concentration in this bulk media was 300 ± 35nM (~145 nanorods in the focal volume of the 1.4 NA objective lens). In the

setup of optical instrument, both recording and readout were conducted in the same homebuilt microscope. For recording, an electro-optic modulator control the repetition rate from the pulse train of a femtosecond pulse laser (SpectraPhysics Tsunami, 100 fs pulse duration, 82MHz repetition rate, tunable between 690 and 1,010 nm). The laser pulses were focused onto the sample through a high NA objective lens (Olympus 1.4 NA). For readout, the TPL of the nanorods was excited using the 82 MHz output from the femtosecond laser. The TPL signal was directed to a photomultiplier tube (Hamamatsu H7422P40) and was detected in the 400 – 600 nm wavelength range. To prevent erasure of the patterns, the pulse energy of the readout laser was two orders of magnitude lower than the patterning pulse energy.

Figure 6.13 shows the experiment result of polarization multiplexing patterning and readout. The pulse laser was performed with 1MHz repetition rate for the purpose of minimizing the effect of heat accumulation. Two state of linear polarization and radial polarization with annular aperture of $\varepsilon = 0.7$ were applied to record different patterns at the same position. Then, those patterns were readout through different state of polarization, as shown in Fig. 6.13.

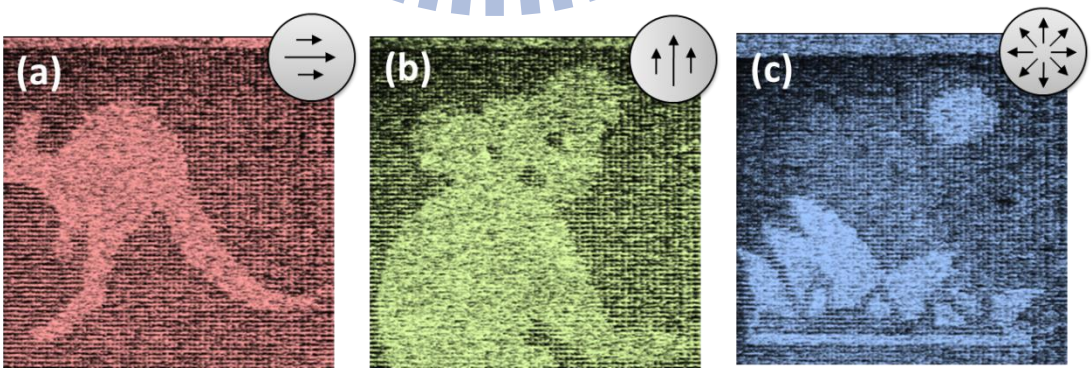

Fig. 6. 13 Polarization multiplexing patterning and readout. Normalized TPL raster scans of eighteen patterns encoded in the same area using three laser light polarizations and one laser wavelengths. Patterns were written in a single layers.

The recording laser pulse properties are indicated. The recordings were retrieved by detecting the TPL excited with the same wavelength and polarization as employed for the recording. The size of all images is 100x100 μm, and the patterns are 75x75 pixels.

6.2.5 Conclusion

In summary, we have successfully perform axial polarization at focus to demonstrate the possibility to detect, melting, and readout its TFL by means of radially polarized illumination in conjunction with annular aperture of $\varepsilon = 0.7$. Through these study, we found azimuthal and radial polarization provide a fast scheme for determine the orientation of nanorods not only for in-plane nanorods but also for out-of-plane nanorods. By changing the apodized ratio of annular aperture, the ratio of longitudinal to transverse electric field can be used for selective melting. In practically, the polarization distribution at focus can be treated as pure axial polarization when the annular pupil of $\varepsilon > 0.7$. Finally, we demonstrated that the possibility of polarization multiplexing patterning and readout through two state of liner polarization and radial polarization with radial polarization with annular aperture of $\varepsilon = 0.7$. Proposed concept is able to significantly increase the recording density of ODS system. Also, the manipulation of the polarization distribution at focal plane by means of annular pupil technique provides a powerful method to target arbitral oriented nanorods which is able to apply to bio image and local heating treatmen

Chapter VII

Conclusion and Outlook

7.1 Thesis Conclusion

In this thesis, we began with the basic theory of a diffraction system toward vectorial diffraction theory which can apply to describe the depolarization effect of a strong focusing condition. From the theory, we do know the beam structure at pupil plane strongly affects the field distribution in the vicinity of the focal point, which reveals 2D to 3D transformation from the 2D pupil plane to the 3D focus volume. The beam structure at the entrance contains the information of amplitude, phase, and polarization. Among those parameters, polarization engineer is the most important and useful but hard to implement in practical. In Chapter 2, we proposed a universal method to synthesis arbitrary polarization structure so-called SIP beam. In addition to superposition method for coherent light source, we also introduce a simple and costless method for the generation of incoherent SIP beam based on segmental method in Chapter 5. Following, the focusing mechanism of radially polarized beam was study in Chapter 3. Based on the fully understand on the optical property of SIP beams, we utilized their unique polarization property to interact with metal material including flat gold thin film as well as gold nano particle. Based on the phase matching condition, the interaction of TM-polarized light and gold nano structure can excite surface plasmon resonance which is useful for the applications on plasmonic device, sensing, imaging, melting, and optical data storage. Individual paper review has been given in Chapter 5 to Chapter 7. Moreover, we proposed several novel ideas for these applications to push technology moving forward by means of pupil engineering. As a summary, a far-field scheme on generation of long-range propagating surface plasmon was proposed in Chapter 5 for

simplified the excitation scheme. For the sensing application, two kinds of SPR sensors were proposed in Chapter 6 based on coherent and incoherent light sources which can be applied for nanoscopy sensing radar and SPR-based spectral microscopy, respectively. Finally, by means of focus polarization vector synthesis, we implement the possibility of imaging, sensing, melting, and cording information on gold nanorods which opens a new era for scientist has the chance to fully utilize polarization in 3D. The concept of 3D polarization manipulation can apply to current bio-image, optical therapy, and advanced optical data storage.

7.2 Outlook

The research in this thesis can be further extended towards a more comprehensive understanding on each proposed optical system, such as far-field SPPs excitation scheme, nanoscopy sensing radar, SPR-based spectral microscopy, and 3D polarization manipulation scheme.

Far-Field SPPs Excitation Scheme

Based on the proposed excitation scheme, we are able to generate a wide range of SPPs patterns, not only steering and manipulating single SPP wave, but also launching multipole SPP waves at the same time. This unique feature could provide a customized SPPs lighting source for advanced plasmonic devices, which can be used for ultrahigh bandwidth devices for optical systems.

Nanoscopy Sensing Radar

Based on proposed interfering SPR sensor, one can utilize radial polarization generated omnidirectional propagating SPP wave to sense the tiny change among the metallic plane

surface. However, this system is a concept which still remains a lot of room for researcher to study its sensing ability, such as accuracy, and applicable targeting area.

3D SPR-based spectral microscopy

Based on incoherent white light radial polarization, we demonstrate the possibility to excite entire wavelength of SPR at the same time for full color sensing application. Current optical configuration can be further integrated with two dimensional scanning stages. In that case, one can generate a three dimentional refractive index map which contains two dimensions in spatial and one dimension in wavelength. This wavelength dependent information could assist researcher to decompose a conventional optical image into a series of refractive index map on individual wavelength which are able to highlight the wavelength dependent structure inside a cell. Moreover, the sensitivity of this white light SPR based sensor could be further improved by doping gold nanorods on the metallic surface.

3D Polarization Manipulation Scheme

We demonstrated the interaction of 3D polarization focus and arbitrary orientated gold nanorods through imaging, sensing, melting, and coding. Also, we utilized this entire process to further increase the recording capacity of bit-by-bit optical data storage by means of melting out-of-plane gold nanorods. As we know that gold nanorods are great polarization absorber which can generate two-photo luminance without the bleaching effect. In addition to increase recording capacity via adding more polarization vector, this technique can also be used for the application on biomedical imaging, diagnostics, and therapy.

References

1. W. T. Welford, "Use of annular aperture to increase focal depth," Journal of the Optical Society of America **50**, 749-753 (1960).
2. R. L. H. Steven T. Yang, Y.-H. Lee, Roger Fabian W. Pease and Gerry Owen, "Effect of central obscuration on image formation in projection lithography," Proc. SPIE **1264**, 477 (1990).
3. S. W. Hell, and J. Wichmann, "Breaking the diffraction resoultion limit by stimulated-emission-stimulated-emission-depletion fluorescence microscopy," Opt. Lett. **19**, 780-782 (1994).
4. S. W. Hell, "Far-field optical nanoscopy," Science **316**, 1153-1158 (2007).
5. D. P. Biss, and T. G. Brown, "Cylindrical vector beam focusing through a dielectric interface: reply to comment," Opt. Express **12**, 970-971 (2004).
6. S. Quabis, R. Dorn, M. Eberler, O. Glockl, and G. Leuchs, "Focusing light to a tighter spot," Opt. Commun. **179**, 1-7 (2000).
7. Y. Mushiake, N. Nakajima, and Matsumur.K, "Generation of radially polarized optical beam mode by lase oscillation," Proceedings of the Institute of Electrical and Electronics Engineers **60**, 1107-& (1972).
8. A. A. Tovar, "Production and propagation of cylindrically polarized Laguerre-Gaussian laser beams," Journal of the Optical Society of America a-Optics Image Science and Vision **15**, 2705-2711 (1998).
9. A. V. Nesterov, V. G. Nizlev, and V. P. Yakunin, "Generation of high-power radially polarized beam," J. Phys. D-Appl. Phys. **32**, 2871-2875 (1999).
10. D. Pohl, "Operation of a ruby-laser in purely transverse electric mode TE01," Appl. Phys. Lett. **20**, 266-& (1972).
11. R. Oron, S. Blit, N. Davidson, A. A. Friesem, Z. Bomzon, and E. Hasman, "The formation of laser beams with pure azimuthal or radial polarization," Appl. Phys. Lett. **77**, 3322-3324 (2000).
12. I. Moshe, S. Jackel, and A. Meir, "Production of radially or azimuthally polarized beams in solid-state lasers and the elimination of thermally induced birefringence effects," Opt. Lett. **28**, 807-809 (2003).
13. S. Quabis, R. Dorn, and G. Leuchs, "Generation of a radially polarized doughnut mode of high quality," Appl. Phys. B-Lasers Opt. **81**, 597-600 (2005).

14. G. Machavariani, N. Davidson, E. Hasman, S. Blit, A. A. Ishaaya, and A. A. Friesem, "Efficient conversion of a Gaussian beam to a high purity helical beam," Opt. Commun. **209**, 265-271 (2002).
15. R. Dorn, S. Quabis, and G. Leuchs, "Sharper focus for a radially polarized light beam," Phys. Rev. Lett. **91** (2003).
16. G. Machavariani, Y. Lumer, I. Moshe, A. Meir, and S. Jacket, "Efficient extracavity generation of radially and azimuthally polarized beams," Opt. Lett. **32**, 1468-1470 (2007).
17. A. K. Spilman, and T. G. Brown, "Stress birefringent, space-variant wave plates for vortex illumination," Applied Optics **46**, 61-66 (2007).
18. W. J. Lai, B. C. Lim, P. B. Phua, K. S. Tiaw, H. H. Teo, M. H. Hong, and Ieee, *Radially polarized light generation using segmented spirally varying retarder* (Ieee, New York, 2008).
19. X. M. Gao, J. S. Li, Y. Fang, Q. F. Zhan, H. M. Guo, and S. L. Zhuang, "A simple method for generating inhomogeneously polarized vector beam," Opt. Lasers Eng. **49**, 899-902 (2011).
20. H. W. Ren, Y. H. Lin, and S. T. Wu, "Linear to axial or radial polarization conversion using a liquid crystal gel," Appl. Phys. Lett. **89**, 3 (2006).
21. N. Passilly, R. de Saint Denis, K. Ait-Ameur, F. Treussart, R. Hierle, and J. F. O. Roch, "Simple interferometric technique for generation of a radially polarized light beam," Journal of the Optical Society of America a-Optics Image Science and Vision **22**, 984-991 (2005).
22. V. G. Niziev, R. S. Chang, and A. V. Nesterov, "Generation of inhomogeneously polarized laser beams by use of a Sagnac interferometer," Applied Optics **45**, 8393-8399 (2006).
23. B. H. Jia, X. S. Gan, and M. Gu, "Direct measurement of a radially polarized focused evanescent field facilitated by a single LCD," Opt. Express **13**, 6821-6827 (2005).
24. Q. W. Zhan, and J. R. Leger, "Focus shaping using cylindrical vector beams," Opt. Express **10**, 324-331 (2002).
25. P. Brijesh, T. J. Kessler, J. D. Zuegel, and D. D. Meyerhofer, "Demonstration of a horseshoe-shaped longitudinal focal profile," J. Opt. Soc. Am. B-Opt. Phys. **24**, 1030-1036 (2007).
26. I. Iglesias, and B. Vohnsen, "Polarization structuring for focal volume shaping in high-resolution microscopy," Opt. Commun. **271**, 40-47 (2007).
27. I. J. Cooper, M. Roy, and C. J. R. Sheppard, "Focusing of pseudoradial polarized beams," Opt. Express **13**, 1066-1071 (2005).
28. P. L. Greene, and D. G. Hall, "Focal shift in vector beams," Opt. Express **4**, 411-419 (1999).
29. K. S. Youngworth, and T. G. Brown, "Focusing of high numerical aperture

cylindrical-vector beams," Opt. Express **7**, 77-87 (2000).
30. L. E. Helseth, "Roles of polarization, phase and amplitude in solid immersion lens systems," Opt. Commun. **191**, 161-172 (2001).
31. S. Quabis, R. Dorn, M. Eberler, O. Glockl, and G. Leuchs, "The focus of light - theoretical calculation and experimental tomographic reconstruction," in *Spring Meeting of the Quantum-Optics-Section of the German-Physical-Society*(Springer-Verlag, Bonn, Germany, 2001), pp. 109-113.
32. D. Ganic, X. S. Gan, and M. Gu, "Focusing of doughnut laser beams by a high numerical-aperture objective in free space," Opt. Express **11**, 2747-2752 (2003).
33. T. Wilson, F. Massournian, and R. Juskaitis, "Generation and focusing of radially polarized electric fields," Opt. Eng. **42**, 3088-3089 (2003).
34. D. P. Biss, and T. G. Brown, "Primary aberrations in focused radially polarized vortex beams," Opt. Express **12**, 384-393 (2004).
35. C. J. R. Sheppard, and A. Choudhury, "Annular pupils, radial polarization, and superresolution," Applied Optics **43**, 4322-4327 (2004).
36. A. S. van de Nes, P. R. T. Munro, S. F. Pereira, J. J. M. Braat, and P. Torok, "Cylindrical vector beam focusing through a dielectric interface: comment," Opt. Express **12**, 967-969 (2004).
37. R. de Saint Denis, N. Passilly, M. Laroche, T. Mohammed-Brahim, and K. Ait-Ameur, "Beam-shaping longitudinal range of a binary diffractive optical element," Applied Optics **45**, 8136-8141 (2006).
38. Y. Kozawa, and S. Sato, "Focusing property of a double-ring-shaped radially polarized beam," Opt. Lett. **31**, 820-822 (2006).
39. M. Leutenegger, R. Rao, R. A. Leitgeb, and T. Lasser, "Fast focus field calculations," Opt. Express **14**, 11277-11291 (2006).
40. Y. Kozawa, and S. Sato, "Sharper focal spot formed by higher-order radially polarized laser beams," Journal of the Optical Society of America a-Optics Image Science and Vision **24**, 1793-1798 (2007).
41. T. H. Lan, and C. H. Tien, "Study on focusing mechanism of radial polarization with immersion objective," in *17th International Symposium on Optical Memory*(Inst Pure Applied Physics, Singapore, SINGAPORE, 2007), pp. 5806-5808.
42. T. H. Lan, and C. H. Tien, "Study on focusing mechanism of radial polarization with immersion objective," Jpn. J. Appl. Phys. **47**, 5806-5808 (2008).
43. L. Z. Rao, J. X. Pu, Z. Y. Chen, and P. Yei, "Focus shaping of cylindrically polarized vortex beams by a high numerical-aperture lens," Opt. Laser Technol. **41**, 241-246 (2009).
44. Q. W. Zhan, "Trapping metallic Rayleigh particles with radial polarization," Opt. Express **12**, 3377-3382 (2004).
45. P. L. Greene, and D. G. Hall, "Properties and diffraction of vector Bessel-Gauss beams,"

Journal of the Optical Society of America a-Optics Image Science and Vision **15**, 3020-3027 (1998).

46. C. C. Sun, and C. K. Liu, "Ultrasmall focusing spot with a long depth of focus based on polarization and phase modulation," Opt. Lett. **28**, 99-101 (2003).
47. R. Borghi, M. Santarsiero, and M. A. Alonso, "Highly focused spirally polarized beams," Journal of the Optical Society of America a-Optics Image Science and Vision **22**, 1420-1431 (2005).
48. B. H. Jia, X. S. Gan, and M. Gu, "Direct observation of a pure focused evanescent field of a high numerical aperture objective lens by scanning near-field optical microscopy," Appl. Phys. Lett. **86**, 3 (2005).
49. L. Novotny, M. R. Beversluis, K. S. Youngworth, and T. G. Brown, "Longitudinal field modes probed by single molecules," Phys. Rev. Lett. **86**, 5251-5254 (2001).
50. K. J. Moh, X. C. Yuan, J. Bu, S. W. Zhu, and B. Z. Gao, "Surface plasmon resonance imaging of cell-substrate contacts with radially polarized beams," Opt. Express **16**, 20734-20741 (2008).
51. R. Vander, and S. G. Lipson, "High-resolution surface-plasmon resonance real-time imaging," Opt. Lett. **34**, 37-39 (2009).
52. M. Mansuripur, "Certain compitational aspecs of vector diffraction problems," Journal of the Optical Society of America a-Optics Image Science and Vision **6**, 786-805 (1989).
53. W. C. Kim, N. C. Park, Y. J. Yoon, H. Choi, and Y. P. Park, "Investigation of near-field imaging characteristics of radial polarization for application to optical data storage," Opt. Rev. **14**, 236-242 (2007).
54. T. H. Lan, and C. H. Tien, "Servo study of radially polarized beam in high numerical aperture optical data storage system," Jpn. J. Appl. Phys. Part 1 - Regul. Pap. Brief Commun. Rev. Pap. **46**, 3758-3760 (2007).
55. Y. Kozawa, and S. Sato, "Generation of a radially polarized laser beam by use of a conical Brewster prism," Opt. Lett. **30**, 3063-3065 (2005).
56. S. C. Tidwell, D. H. Ford, and W. D. Kimura, "Generating radially polarized beams interfertrically," Applied Optics **29**, 2234-2239 (1990).
57. P. Torok, P. Varga, and G. R. Booker, "Electromagnetic diffraction of light focused through a planar interface between materials of mismatched refractive-indexs-structure of the clcctromagnetic-field," Journal of the Optical Society of America a-Optics Image Science and Vision **12**, 2136-2144 (1995).
58. D. P. Biss, and T. G. Brown, "Cylindrical vector beam focusing through a dielectric interface," Opt. Express **9**, 490-497 (2001).
59. R. W. Wood, "On a remarkable case of uneven distribution of light in a diffraction grating spectrum," Philos. Mag. **4**, 396-402 (1902).
60. U. Fano, "The theory of anomalous diffraction gratings and of quasi-stationary waves on

metallic surfaces (Sommerfeld's waves)," Journal of the Optical Society of America **31**, 213-222 (1941).

61. R. H. Ritchie, "Plasma losses by fast electrons in thin films," Phys. Rev. **106**, 874-881 (1957).
62. E. A. Stern, and R. A. Ferrell, "Surface plasma oscillations of a fegenerate electron gas," Phys. Rev. **120**, 130-136 (1960).
63. H. Raether, "Surface-plasmons on smooth ad rough surfaces and on greatings," Springer Tracts Mod. Phys. **111**, 1-133 (1988).
64. S. A. Maier, "Plasmonics: Fundamentals and Applications," (Springer, 2007).
65. S. I. Bozhevolnyi, and F. A. Pudonin, "Two-dimensional micro-optics of surface plasmons," Phys. Rev. Lett. **78**, 2823-2826 (1997).
66. F. I. Baida, D. Van Labeke, A. Bouhelier, T. Huser, and D. W. Pohl, "Propagation and diffraction of locally excited surface plasmons," Journal of the Optical Society of America a-Optics Image Science and Vision **18**, 1552-1561 (2001).
67. W. L. Barnes, A. Dereux, and T. W. Ebbesen, "Surface plasmon subwavelength optics," Nature **424**, 824-830 (2003).
68. M. I. Stockman, "Nanofocusing of optical energy in tapered plasmonic waveguides," Phys. Rev. Lett. **93** (2004).
69. H. Ditlbacher, J. R. Krenn, G. Schider, A. Leitner, and F. R. Aussenegg, "Two-dimensional optics with surface plasmon polaritons," Appl. Phys. Lett. **81**, 1762-1764 (2002).
70. L. L. Yin, V. K. Vlasko-Vlasov, J. Pearson, J. M. Hiller, J. Hua, U. Welp, D. E. Brown, and C. W. Kimball, "Subwavelength focusing and guiding of surface plasmons," Nano Lett. **5**, 1399-1402 (2005).
71. A. G. Curto, and F. J. G. de Abajo, "Near-field optical phase antennas for long-range plasmon coupling," Nano Lett. **8**, 2479-2484 (2008).
72. B. Hecht, H. Bielefeldt, L. Novotny, Y. Inouye, and D. W. Pohl, "Local excitation, scattering, and interference of surface plasmons," Phys. Rev. Lett. **77**, 1889-1892 (1996).
73. Q. W. Zhan, "Evanescent Bessel beam generation via surface plasmon resonance excitation by a radially polarized beam," Opt. Lett. **31**, 1726-1728 (2006).
74. W. B. Chen, and Q. W. Zhan, "Realization of an evanescent Bessel beam via surface plasmon interference excited by a radially polarized beam," Opt. Lett. **34**, 722-724 (2009).
75. Z. J. Hu, P. S. Tan, S. W. Zhu, and X. C. Yuan, "Structured light for focusing surface plasmon polaritons," Opt. Express **18**, 10864-10870 (2010).
76. M. G. Somekh, G. Stabler, S. G. Liu, J. Zhang, and C. W. See, "Wide-field high-resolution surface-plasmon interference microscopy," Opt. Lett. **34**, 3110-3112 (2009).
77. T. Wilson, R. Juskaitis, and P. Higdon, "The imaging of dielectric point scatterers in conventional and confocal polarisation microscopes," Opt. Commun. **141**, 298-313

(1997).
78. L. Novotny, and B. Hecht, "Principles of Nano-optics," (Cambridge U. Press, 2006).
79. E. Wolf, "Electromagnetic Diffraction in Optical Systems. I. An Integral Representation of the Image Field," Proceedings of the Royal Society of London. Series A, Mathematical and Physical Sciences **253**, 349-357 (1959).
80. B. Richards, and E. Wolf, "Electromagnetic Diffraction in Optical Systems. II. Structure of the Image Field in an Aplanatic System," Proceedings of the Royal Society of London. Series A, Mathematical and Physical Sciences **253**, 358-379 (1959).
81. A. Bouhelier, F. Ignatovich, A. Bruyant, C. Huang, G. C. D. Francs, J. C. Weeber, A. Dereux, G. P. Wiederrecht, and L. Novotny, "Surface plasmon interference excited by tightly focused laser beams," Opt. Lett. **32**, 2535-2537 (2007).
82. H. Kano, S. Mizuguchi, and S. Kawata, "Excitation of surface-plasmon polaritons by a focused laser beam," J. Opt. Soc. Am. B-Opt. Phys. **15**, 1381-1386 (1998).
83. P. S. Tan, X. C. Yuan, J. Lin, Q. Wang, and R. E. Burge, "Analysis of surface plasmon interference pattern formed by optical vortex beams," Opt. Express **16**, 18451-18456 (2008).
84. P. S. Tan, X. C. Yuan, J. Lin, Q. Wang, T. Mei, R. E. Burge, and G. G. Mu, "Surface plasmon polaritons generated by optical vortex beams," Appl. Phys. Lett. **92**, 3 (2008).
85. A. Bouhelier, and G. P. Wiederrecht, "Surface plasmon rainbow jets," Opt. Lett. **30**, 884-886 (2005).
86. M. F. Xiao, R. Machorro, and J. Siqueiros, "Interference in far-field radiation of two contra-propagating surface plasmon polaritons in the Kretchmann configuration," J. Vac. Sci. Technol. A-Vac. Surf. Films **16**, 1420-1424 (1998).
87. Y. Garini, B. J. Vermolen, and I. T. Young, "From micro to nano: recent advances in high-resolution microscopy," Curr. Opin. Biotechnol. **16**, 3-12 (2005).
88. K. A. Willets, and R. P. Van Duyne, "Localized surface plasmon resonance spectroscopy and sensing," Annu. Rev. Phys. Chem. **58**, 267-297 (2007).
89. Kretschm.E, and H. Raether, "Radiative decay of non radiative surface plasmons excited by light," Zeitschrift Fur Naturforschung Part a-Astrophysik Physik Und Physikalische Chemie **A 23**, 2135-& (1968).
90. A. Otto, "Excitation of nonradiative surface plasma waves in silver by method of frustrated total reflection," Zeitschrift Fur Physik **216**, 398-& (1968).
91. H. Kano, and W. Knoll, "Locally excited surface-plasmon-polaritons for thickness measurement of LBK films," Opt. Commun. **153**, 235-239 (1998).
92. A. Duval, A. Laisne, D. Pompon, S. Held, A. Bellemain, J. Moreau, and M. Canva, "Polarimetric surface plasmon resonance imaging biosensor," Opt. Lett. **34**, 3634-3636 (2009).
93. K. J. Moh, X. C. Yuan, J. Bu, S. W. Zhu, and B. Z. Gao, "Radial polarization induced surface

plasmon virtual probe for two-photon fluorescence microscopy," Opt. Lett. **34**, 971-973 (2009).

94. E. M. Yeatman, "Resolution and sensitivity in surface plasmon microscopy and sensing," in *Artifical Biosensing Interfaces (ABI) Workshop No 2 - Surface Characterization and Optical Sensing Methods in Biosensors*(Elsevier Advanced Technology, Tampere, Finland, 1995), pp. 635-649.
95. B. Rothenhausler, and W. Knoll, "Interferometric determination of the complex wave of plasmon surface-polaritons," J. Opt. Soc. Am. B-Opt. Phys. **5**, 1401-1405 (1988).
96. C. E. H. Berger, R. P. H. Kooyman, and J. Greve, "Resoultion in surface-plasmon microscopy," Rev. Sci. Instrum. **65**, 2829-2836 (1994).
97. C. E. H. Berger, R. P. H. Kooyman, and J. Greve, "Surface plasmon propagation near an index step," Opt. Commun. **167**, 183-189 (1999).
98. T. A. Leskova, A. A. Maradudin, and W. Zierau, "Surface plasmon polariton propagation near an index step," Opt. Commun. **249**, 23-35 (2005).
99. A. V. Zayats, Smolyaninov, Ii, and A. A. Maradudin, "Nano-optics of surface plasmon polaritons," Phys. Rep.-Rev. Sec. Phys. Lett. **408**, 131-314 (2005).
100. J. Homola, "Surface plasmon resonance sensors for detection of chemical and biological species," Chem. Rev. **108**, 462-493 (2008).
101. R. Zhao, T. Zhai, Z. Wang, Y. Wang, and D. Liu, "Simultaneous excitation of cavity resonance and surface plasmon resonance in Ag/Al2O3/Ag layer structure," Appl. Phys. B-Lasers Opt. **92**, 585-588 (2008).
102. A. Shoham, R. Vander, and S. G. Lipson, "Production of radially and azimuthally polarized polychromatic beams," Opt. Lett. **31**, 3405-3407 (2006).
103. T. Grosjean, M. Suarez, and A. Sabac, "Generation of polychromatic radially and azimuthally polarized beams," Appl. Phys. Lett. **93** (2008).
104. D. A. Parthenopoulos, and P. M. Rentzepis, "3-dimendsional optical storage memory.," Science **245**, 843-845 (1989).
105. E. Walker, A. Dvornikov, K. Coblentz, S. Esener, and P. Rentzepis, "Toward terabyte two-photon 3D disk," Opt. Express **15**, 12264-12275 (2007).
106. E. Walker, A. Dvornikov, K. Coblentz, and P. Rentzepis, "Terabyte recorded in two-photon 3D disk," Applied Optics **47**, 4133-4139 (2008).
107. X. P. Li, J. W. M. Chon, S. H. Wu, R. A. Evans, and M. Gu, "Rewritable polarization-encoded multilayer data storage in 2,5-dimethyl-4-(p-nitrophenylazo) anisole doped polymer," Opt. Lett. **32**, 277-279 (2007).
108. P. Zijlstra, J. W. M. Chon, and M. Gu, "Five-dimensional optical recording mediated by surface plasmons in gold nanorods," Nature **459**, 410-413 (2009).
109. J. Perez-Juste, I. Pastoriza-Santos, L. M. Liz-Marzan, and P. Mulvaney, "Gold nanorods: Synthesis, characterization and applications," Coord. Chem. Rev. **249**, 1870-1901 (2005).

110. C. R. Martin, "nanomaterials - a membrane based synthetic approach," Science **266**, 1961-1966 (1994).
111. C. R. Martin, "Membrane-based synthesis of nanomaterials," Chem. Mat. **8**, 1739-1746 (1996).
112. B. M. I. vanderZande, M. R. Bohmer, L. G. J. Fokkink, and C. Schonenberger, "Aqueous gold sols of rod-shaped particles," J. Phys. Chem. B **101**, 852-854 (1997).
113. B. M. I. van der Zande, M. R. Bohmer, L. G. J. Fokkink, and C. Schonenberger, "Colloidal dispersions of gold rods: Synthesis and optical properties," Langmuir **16**, 451-458 (2000).
114. Y. Y. Yu, S. S. Chang, C. L. Lee, and C. R. C. Wang, "Gold nanorods: Electrochemical synthesis and optical properties," J. Phys. Chem. B **101**, 6661-6664 (1997).
115. S. S. Chang, C. W. Shih, C. D. Chen, W. C. Lai, and C. R. C. Wang, "The shape transition of gold nanorods," Langmuir **15**, 701-709 (1999).
116. N. R. Jana, L. Gearheart, and C. J. Murphy, "Wet chemical synthesis of high aspect ratio cylindrical gold nanorods," J. Phys. Chem. B **105**, 4065-4067 (2001).
117. B. Nikoobakht, and M. A. El-Sayed, "Preparation and growth mechanism of gold nanorods (NRs) using seed-mediated growth method," Chem. Mat. **15**, 1957-1962 (2003).
118. N. R. Jana, "Gram-scale synthesis of soluble, near-monodisperse gold nanorods and other anisotropic nanoparticles," Small **1**, 875-882 (2005).
119. M. P. Pileni, "The role of soft colloidal templates in controlling the size and shape of inorganic nanocrystals," Nat. Mater. **2**, 145-150 (2003).
120. N. R. Jana, L. Gearheart, and C. J. Murphy, "Evidence for seed-mediated nucleation in the chemical reduction of gold salts to gold nanoparticles," Chem. Mat. **13**, 2313-2322 (2001).
121. M. B. Mohamed, Z. L. Wang, and M. A. El-Sayed, "Temperature-dependent size-controlled nucleation and growth of gold nanoclusters," J. Phys. Chem. A **103**, 10255-10259 (1999).
122. B. Nikoobakht, and M. A. El-Sayed, "Evidence for bilayer assembly of cationic surfactants on the surface of gold nanorods," Langmuir **17**, 6368-6374 (2001).
123. K. R. Brown, and M. J. Natan, "Hydroxylamine seeding of colloidal Au nanoparticles in solution and on surfaces," Langmuir **14**, 726-728 (1998).
124. J. X. Gao, C. M. Bender, and C. J. Murphy, "Dependence of the gold nanorod aspect ratio on the nature of the directing surfactant in aqueous solution," Langmuir **19**, 9065-9070 (2003).
125. Z. L. Wang, M. B. Mohamed, S. Link, and M. A. El-Sayed, "Crystallographic facets and shapes of gold nanorods of different aspect ratios," Surf. Sci. **440**, L809-L814 (1999).
126. M. Z. Liu, and P. Guyot-Sionnest, "Mechanism of silver(I)-assisted growth of gold

nanorods and bipyramids," J. Phys. Chem. B **109**, 22192-22200 (2005).

127. H. Petrova, J. Perez-Juste, Z. Y. Zhang, J. Zhang, T. Kosel, and G. V. Hartland, "Crystal structure dependence of the elastic constants of gold nanorods," J. Mater. Chem. **16**, 3957-3963 (2006).
128. C. J. Johnson, E. Dujardin, S. A. Davis, C. J. Murphy, and S. Mann, "Growth and form of gold nanorods prepared by seed-mediated, surfactant-directed synthesis," J. Mater. Chem. **12**, 1765-1770 (2002).
129. P. Mulvaney, "Surface plasmon spectroscopy of nanosized metal particles," Langmuir **12**, 788-800 (1996).
130. K. L. Kelly, E. Coronado, L. L. Zhao, and G. C. Schatz, "The optical properties of metal nanoparticles: The influence of size, shape, and dielectric environment," J. Phys. Chem. B **107**, 668-677 (2003).
131. P. K. Jain, K. S. Lee, I. H. El-Sayed, and M. A. El-Sayed, "Calculated absorption and scattering properties of gold nanoparticles of different size, shape, and composition: Applications in biological imaging and biomedicine," J. Phys. Chem. B **110**, 7238-7248 (2006).
132. R. W. Schoenlein, W. Z. Lin, J. G. Fujimoto, and G. L. Eesley, "Femtoseconf studes pf mpmeqio;obrium e;ectronic process in Metals," Phys. Rev. Lett. **58**, 1680-1683 (1987).
133. N. Del Fatti, R. Bouffanais, F. Vallee, and C. Flytzanis, "Nonequilibrium electron interactions in metal films," Phys. Rev. Lett. **81**, 922-925 (1998).
134. J. Y. Bigot, J. C. Merle, O. Cregut, and A. Daunois, "Electron dynamics dyma,ics in dynamics in copper metallic nanoparticels probed with femtosecond optical pulses," Phys. Rev. Lett. **75**, 4702-4705 (1995).
135. H. Inouye, K. Tanaka, I. Tanahashi, and K. Hirao, "Ultrafast dynamics of nonequilibrium electrons in a gold nanoparticle system," Phys. Rev. B **57**, 11334-11340 (1998).
136. S. Link, and M. A. El-Sayed, "Spectral properties and relaxation dynamics of surface plasmon electronic oscillations in gold and silver nanodots and nanorods," J. Phys. Chem. B **103**, 8410-8426 (1999).
137. C. Voisin, N. Del Fatti, D. Christofilos, and F. Vallee, "Ultrafast electron dynamics and optical nonlinearities in metal nanoparticles," J. Phys. Chem. B **105**, 2264-2280 (2001).
138. G. V. Hartland, "Measurements of the material properties of metal nanoparticles by time-resolved spectroscopy," Phys. Chem. Chem. Phys. **6**, 5263-5274 (2004).
139. H. Ditlbacher, J. R. Krenn, B. Lamprecht, A. Leitner, and F. R. Aussenegg, "Spectrally coded optical data storage by metal nanoparticles," Opt. Lett. **25**, 563-565 (2000).
140. H. H. Pham, I. Gourevich, J. K. Oh, J. E. N. Jonkman, and E. Kumacheva, "A multidye nanostructured material for optical data storage and security data encryption," Adv. Mater. **16**, 516-+ (2004).
141. Y. Niidome, S. Urakawa, M. Kawahara, and S. Yamada, "Dichroism of poly(vinylalcohol)

films containing gold nanorods induced by polarized pulsed-laser irradiation," Jpn. J. Appl. Phys. Part 1 - Regul. Pap. Short Notes Rev. Pap. **42**, 1749-1750 (2003).

142. O. Wilson, G. J. Wilson, and P. Mulvaney, "Laser writing in polarized silver nanorod films," Adv. Mater. **14**, 1000 (2002).
143. S. Alasfar, M. Ishikawa, Y. Kawata, C. Egami, O. Sugihara, N. Okamoto, M. Tsuchimori, and O. Watanabe, "Polarization-multiplexed optical memory with urethane-urea copolymers," Applied Optics **38**, 6201-6204 (1999).
144. J. Perez-Juste, B. Rodriguez-Gonzalez, P. Mulvaney, and L. M. Liz-Marzan, "Optical control and patterning of gold-nanorod-poly(vinyl alcohol) nanocomposite films," Adv. Funct. Mater. **15**, 1065-1071 (2005).
145. S. Kawata, and Y. Kawata, "Three-dimensional optical data storage using photochromic materials," Chem. Rev. **100**, 1777-1788 (2000).
146. J. H. Strickler, and W. W. Webb, "3-dimensional optical-data storage in refractive media by 2-photon point excitation," Opt. Lett. **16**, 1780-1782 (1991).
147. B. H. Cumpston, S. P. Ananthavel, S. Barlow, D. L. Dyer, J. E. Ehrlich, L. L. Erskine, A. A. Heikal, S. M. Kuebler, I. Y. S. Lee, D. McCord-Maughon, J. Q. Qin, H. Rockel, M. Rumi, X. L. Wu, S. R. Marder, and J. W. Perry, "Two-photon polymerization initiators for three-dimensional optical data storage and microfabrication," Nature **398**, 51-54 (1999).
148. J. F. Heanue, M. C. Bashaw, and L. Hesselink, "Volume holographic storage and retrieval of digital data," Science **265**, 749-752 (1994).
149. D. Day, M. Gu, and A. Smallridge, "Rewritable 3D bit optical data storage in a PMMA-based photorefractive polymer," Adv. Mater. **13**, 1005 (2001).